Metabolic Imaging and

Applications in Protein and Lipid Homeostasis

Yihui Shen

Submitted in partial fulfillment of the requirements for the degree of

Doctor of Philosophy

in the Graduate School of Arts and Sciences

COLUMBIA UNIVERSITY

2017

ABSTRACT

Metabolic Imaging and Applications in Protein and Lipid Homeostasis

Yihui Shen

Metabolic activity is an important functional parameter of a living cell. Microscopic techniques are demanded to resolve the heterogeneity of metabolic activity from cell to cell and among subcellular compartments. Towards this, work in the Min lab has been dedicated to developing a prevailing metabolic imaging platform that couples chemical imaging by stimulated Raman scattering (SRS) microscopy with small vibrational tags on precursor molecules. This thesis describes efforts along metabolic imaging by SRS microscopy, with focus on visualizing protein and lipid homeostasis. Chapter 1 describes the design principle of metabolic imaging, including selection of vibrational tags and setup of SRS microscopy, and an overview of successful demonstrations of metabolic imaging in protein and lipid metabolism. Chapter 2 describes adoption of such principle to visualize protein turnover with ^{13}C-phenylalanine metabolic labeling under steady-state condition and various perturbations. The rest of this thesis (Chapters 3-6) switches focus to fatty acid metabolism and cellular lipid homeostasis. As the minimal tagging in vibrational imaging preserves the physicochemical property of lipid molecules to the largest extent, it motivated me to revisit fatty acid metabolism from a biophysical perspective. Bearing the question in mind whether the non-equilibrium metabolic activity could drive phase

separation in biological membranes, I thus look into the principle of membrane organization and its implication in biological membranes in Chapter 3. Then in Chapter 4, I describe the discovery and characterization of previously unknown phase separation in endoplasmic reticulum (ER) membrane caused by lipid synthesis. In this case, metabolic imaging by SRS enables identification of solid-like domains formed by saturated fatty acid (SFA) metabolites. This observation further raises the question whether phase separation bears any functional roles in the adverse effects of SFAs (or lipotoxicity). Towards this, Chapter 5 introduces the background of lipotoxicity including its definition and models. Then I review proposed mechanisms for lipotoxicity, which point to the central role of ER in mediating the stress transduction. In Chapter 6, I present our findings that suggest the association of the observed solid-like domains with ER structural remodeling and local autophagic arrest. Together, these efforts demonstrate the valuable capability of SRS imaging to reveal metabolic heterogeneity and how this aids in the investigation of metabolic stress.

TABLE OF CONTENTS

LIST OF FIGURES

LIST OF TABLES

ACKNOWLEDGEMENT

Chapter 1

Metabolic Imaging by stimulated Raman scattering microscopy

1.1 Vibrational tags for small molecules

Contrast mechanisms for imaging biomacromolecules are well established. For example, proteins can be visualized by staining with dye-labeled antibody or genetically encoded green fluorescent protein (GFP) tag. Nucleic acids can be visualized by hybridization or tagging with recognizable sequence. The limit in live cell has been pushed to imaging translation event at single molecule resolution, by tagging proteins with multimerized epitopes and mRNAs with repeating sequence that recruits dozens of fluorescent labels (*1–4*). Yet small molecules do not have comparable tolerance for giant tags. Hence the development of contrast mechanisms for small molecules focuses on minimizing the size of the tag. Towards this, the limit goes to a single atom, such as in techniques such as positron emission tomography (PET) (*5*), multi-isotope imaging mass spectroscopy (MIMS) (*6*), or a chemical bond in optical-based vibrational imaging (*7*). Among these, the optical-based vibrational imaging has become increasingly popular owing to its fine subcellular resolution and live-cell compatibility. The tailored development of vibrational tags not only enables subcellular tracking of small molecule, but also provides contrast for activity-based metabolic imaging.

Currently most of the vibrational tags fall into two major categories: alkyne-based (or the like) and stable-isotope-based (*7, 8*). Development of bioorthogonal chemistry introduced alkyne as a chemical handle onto analogs of nucleosides, amino acids, fatty acids, glycans, and drugs (*9*). These analogs mimic their natural counterparts and can be incorporated into their metabolites

though at lower rates (e.g. ~1/1000 for methionine analog (*10*)). Alkyne turns out to be a good

orthogonal tag for vibrational imaging too. Triple bond is rare in biological systems, and its

vibration occurs in a cell-silent region (1800~2600 cm^{-1}) free of cellular background. In addition,

the stretching of C≡C bond is a strong vibrational mode (*11*), which makes it a sensitive reporter.

Lastly, the narrow linewidth of triple bond stretching (FWHM ~ 14 cm^{-1}) promises

straightforward multiplexing imaging (*12*). On the other hand, stable isotopes offer minimal

labeling for vibrational imaging. The heavier weight of an isotope (e.g. deuterium) slows down

the vibration of the associated chemical bond (e.g. carbon-deuterium, C-D), thus creating

red-shifted frequency (e.g. 2100cm^{-1} for C-D compared to 2900 cm^{-1} for C-H) **(Figure 1.1)**.

Isotope labeling to the largest extent preserves the biochemical identity of the small molecule,

hence it bears essentially no toxicity and usually does not require functional characterization.

Though Raman cross section of a single C-D bond is 1-2 orders of magnitude smaller than

alkyne, more than one substitution can be introduced into one molecule. Stable isotopes have

also found broad application elsewhere in spectroscopic techniques such as nuclear magnetic

resonance (NMR), quantitative mass spectroscopy (*13*), and Raman spectroscopy(*14*). Thus the

great availability of commercial source for isotope-labeled molecules could save the effort to

synthesize new probes.
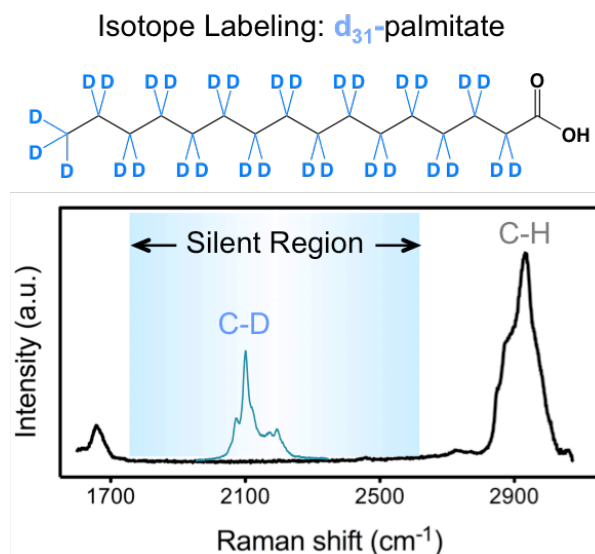
Figure 1.1 Isotope labeling for vibrational imaging. Isotope labeling of a fatty acid molecule produces carbon-deuterium (C-D) vibration in the cell silent region of Raman spectroscopy. Black curve shows Raman spectrum obtained from non-labeled HeLa cell. Blue curve shows Raman spectrum obtained from the labeled molecule.

1.2 Quantitative metabolic imaging by stimulated Raman scattering microscopy

Bond-selective stimulated Raman scattering (SRS) microscopy has proven to be the most suited technique for optical imaging of the incorporated vibrational tags. In SRS microscopy, one pump laser and one Stokes laser are used. 'Bond-selective' refers to the fine spectral resolution ($\sim$6cm^{-1}) produced by narrow-band lasers (6ps). Bond-selective detection is achieved by tuning the pump laser wavelength so that the energy difference between the two lasers matches with the vibrational energy of the targeted chemical bond. In this case, SRS signal (S) can be produced in proportion to the chemical concentration ([c]), the Raman cross section of the chemical bond in the molecule ($\sigma_{molecule}$), and laser powers (I_{pump} and I_{Stokes}), i.e. $S \propto [c] \cdot \sigma_{molecule} \cdot I_{pump} \cdot I_{Stokes}$ (15).

The nonlinear laser power dependence is analogous to other types of multi-photon microscopy, which usually adopt tight focus and point scanning and are intrinsically capable of optical sectioning. The instrumental setup is shown below **(Figure 1.2)**. Apart from the narrow band lasers and the laser-scanning module, this setup also integrates a forward detection module (condenser/filter/photodiode) and a high-frequency modulation transfer scheme (modulator/lock-in amplifier), which are commonly adopted in pump-probe microscopy and will be explained below.

The signal generation in SRS microscopy can be readily understood with the description of light-molecule interaction **(Figure 1.2)**. In the focal volume where the light is intense enough for nonlinear interaction, energy exchange occurs between the molecule's vibration and pump/Stokes photons. During each interaction, one molecule is promoted from ground state to vibrational state, while one photon is lost in the pump field and one photon is gained in the Stokes field (result of energy conservation). The loss of pump photon numbers and the gain in Stokes photon numbers (also light intensities) are referred to as stimulated Raman loss (SRL) and stimulated Raman gain (SRG). The frequency of such event depends on how many molecules are present in the focal volume ($[c]$), how likely each molecule is going to interact with photons ($\sigma_{molecule}$), and how many photons are there in each beam (I_{pump} and I_{Stokes}), which can be summarized as $S \propto [c] \cdot \sigma_{molecule} \cdot I_{pump} \cdot I_{Stokes}$. However, direct detection of SRL or SRG

(i.e. changes in intensity) over large laser intensity is not achievable (usually $\Delta I/I < 10^{-3}$), due to intensity fluctuation caused by laser, scanning, and sample heating. Thus SRS usually adopts high-frequency modulation transfer scheme. Basically, Stokes beam is on-off modulated, so that this modulation can be transferred to the pump beam with amplitude S, as a result of light-molecule interaction. Only the transmitted pump beam is then detected and its intensity modulation (amplitude S) is extracted by a lock-in amplifier, with final noise approaching the inherent photon noise of pump laser.
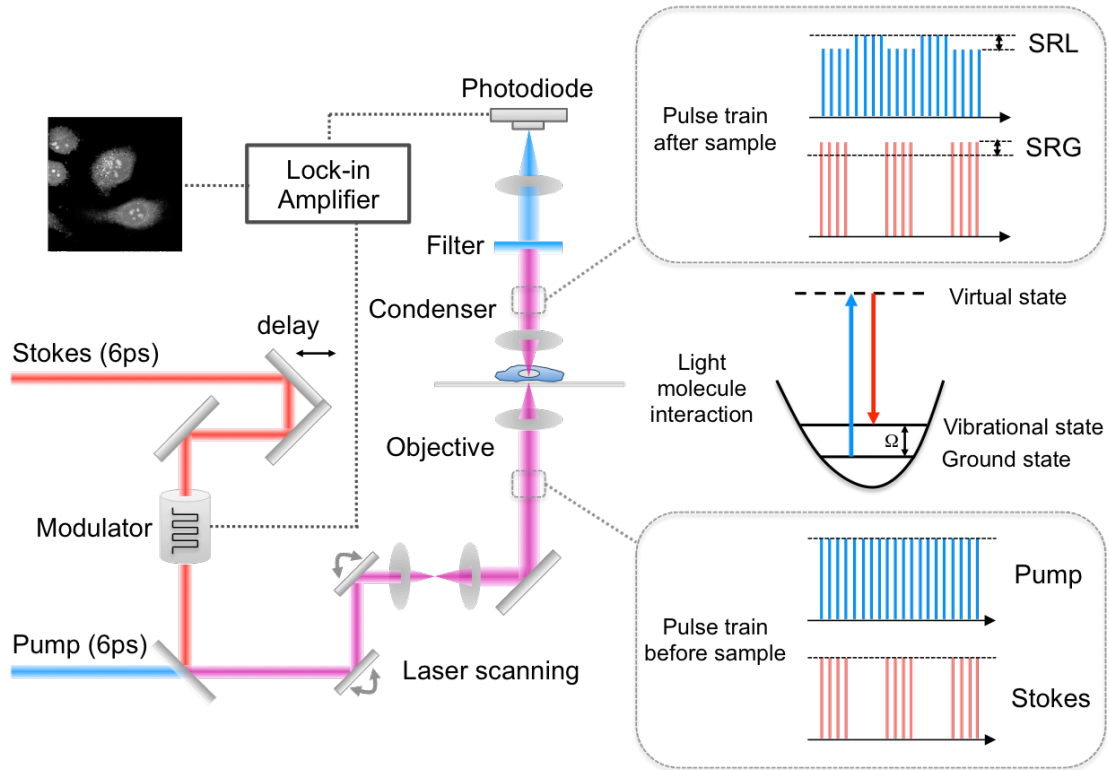
Figure 1.2 Instrumental setup and signal generation for stimulated Raman scattering microscopy. Stokes beam with optimized delay and modulation is combined with pump beam. They are then sent into a laser scanning microscope and focused onto sample by an objective, and then collected by a collimating condenser. A filter blocks Stokes beam to allow detection of pump beam by a photodiode and demodulation by lock-in amplifier. The output

signal is then registered in the image pixel by pixel. The light-molecule interaction is shown on the right together with light intensity change before and after interaction (viewed from bottom to top).

1.3 Applications in protein metabolism and lipid metabolism

With the incorporation of vibrational tags through metabolic activity, and the quantitative chemical mapping of these tags by SRS microscopy, this imaging modality has found broad developments and applications in visualizing protein and lipid metabolism. As the last piece in central dogma, protein metabolism is tightly controlled. The turnover dynamics of proteins, both synthesis and degradation, can be imaged from the metabolic incorporation of labeled amino acids after pulse and/or chase. Such information would be valuable under scenarios such as local protein synthesis (*16*) and failure of protein quality control system (*17*). Lipids comprise another kind of indispensable biomolecules that function in energy storage, membrane architecture and signaling. They consist of a variety of molecules. For example, cholesterol is a major component in plasma membrane; triacylglycerides and cholesterol esters are the major lipids stored in lipid droplets; and the amphipathic phospholipids make up most of the cell membrane. To study lipid metabolism, namely lipid biosynthesis, Raman labels could be introduced into the precursors or building blocks. Enrichment of labels into the newly synthesized lipids could offer contrast for imaging. Here I have summarized applications of vibrational tags for imaging protein metabolism and lipid metabolism **(Table 1)**, which will also be major focus of this thesis.

Table 1. Summary of recent applications of metabolic imaging

Protein metabolism			
Vibrational tag	**Reported activity**	**Detection**	**Ref**
Hpg (alkyne bearing methionine analog)	protein synthesis	SRS microscopy	(*18, 19*)
d_5-phenylalanine	protein synthesis	Raman microspectroscopy	(*20*)
deuterated amino acids	protein synthesis in delicate neuronal systems and animal, two-color pulse chase labeling	SRS microscopy	(*21, 22*)
^{13}C-phenylalanine	protein turnover under steady state and in neuro-degenerative model	SRS microscopy	(*23*) **Chapter 2**
deuterated amino acids	protein degradation measured by decay of C-H signal	SRS microscopy	(*22*)

Lipid metabolism (readers can also refer to more specialized reviews (*24, 25*))			
Vibrational tag	**Reported activity**	**Detection**	**Ref**
d_6-cholesterol	cholesterol scavenged by macrophage accumulates in LDs	Raman microspectroscopy	(*26*)
d_{38}-cholesterol	heterogeneous partitioning of free cholesterol, cholesterol ester and triglyceride into LDs	SRS	(*27*)
phenyldiyne cholesterol	esterified cholesterol in LDs, free cholesterol in lysosome of disease model, uptake in C elegans	SRS	(*28*)
d_9-choline	phospholipid synthesis, elevated in cancer cells, important in embryogenesis	SRS	(*29*)
propargyl-choline	phospholipid synthesis	SRS	(*18*)
d_8-arachidonic acid	LD phagosome interaction in neutrophils	Raman microspectroscopy	(*30*)
d_{31}-palmitic acid d_{33}-oleic acid	fatty acid scavenging kinetics in macrophages	Raman microspectroscopy	(*26, 31*)
d_{33}-/d_2- oleic acid	LD synthesis	CARS	(*32, 33*)
d_{31}-palmtic acid	LD and membrane synthesis	SRS	(*34*)
multiple deuterated fatty acids	neutral lipid profiling	hyperspectral SRS	(*35*)
17-octadecynoic acid (alkyne-palmitic acid)	LD accumulation in cells and C. elegans	SRS	(*18, 19*)

LD: lipid droplet

1.4 References

1. C. Wang, B. Han, R. Zhou, X. Zhuang, Real-Time Imaging of Translation on Single mRNA Transcripts in Live Cells. *Cell*. **165**, 990–1001 (2016).

2. X. Yan, T. A. Hoek, R. D. Vale, M. E. Tanenbaum, Dynamics of Translation of Single mRNA Molecules in Vivo. *Cell*. **165**, 976–989 (2016).

3. B. Wu, C. Eliscovich, Y. J. Yoon, R. H. Singer, *Science*, **352**, 1430-1435 (2016).

4. T. Morisaki *et al.*, Real-time quantification of single RNA translation dynamics in living cells. *Science*. **352**, 1425–1429 (2016).

5. S. S. Gambhir, Molecular imaging of cancer with positron emission tomography. *Nat Rev Cancer*. **2**, 683–693 (2002).

6. M. L. Steinhauser *et al.*, Multi-isotope imaging mass spectrometry quantifies stem cell division and metabolism. *Nature*. **481**, 516–9 (2012).

7. L. Wei *et al.*, Live-cell bioorthogonal chemical imaging: stimulated Raman scattering microscopy of vibrational probes. *Acc. Chem. Res.* **49**, 1494–1502 (2016).

8. B. Błasiak, C. H. Londergan, L. J. Webb, M. Cho, Vibrational Probes: From Small Molecule Solvatochromism Theory and Experiments to Applications in Complex Systems. *Acc. Chem. Res.* **50**, 968–976 (2017).

9. M. Grammel, H. C. Hang, Chemical reporters for biological discovery. *Nat Chem Biol*. **9**, 475–484 (2013).

10. K. L. Kiick, D. A. Tirrell, Protein Engineering by In Vivo Incorporation of Non-Natural Amino Acids: Control of Incorporation of Methionine Analogues by Methionyl-tRNA Synthetase. *Tetrahedron*. **56**, 9487 (2000).

11. H. Yamakoshi *et al.*, Alkyne-tag Raman imaging for visualization of mobile small molecules in live cells. *J. Am. Chem. Soc.* **134**, 20681–20689 (2012).

12. L. Wei *et al.*, Super-multiplex vibrational imaging. *Nature*. **544**, 465–470 (2017).

13. S.-E. Ong *et al.*, Stable Isotope Labeling by Amino Acids in Cell Culture, SILAC, as a

Simple and Accurate Approach to Expression Proteomics. *Mol. Cell. Proteomics*. **1**, 376–386 (2002).

14. M. Li, W. E. Huang, C. M. Gibson, P. W. Fowler, A. Jousset, Stable isotope probing and Raman spectroscopy for monitoring carbon flow in a food chain and revealing metabolic pathway. *Anal. Chem.* **85**, 1642–9 (2013).

15. W. Min, C. W. Freudiger, S. Lu, X. S. Xie, Coherent nonlinear optical imaging: beyond fluorescence microscopy. *Annu. Rev. Phys. Chem.* **62**, 507–530 (2011).

16. H. Kang, E. M. Schuman, A requirement for local protein synthesis in neurotrophin-induced hippocampal synaptic plasticity. *Science*. **273**, 1402–6 (1996).

17. A. Tsvetkov, M. Arrasate, S. Barmada, Proteostasis of polyglutamine varies among neurons and predicts neurodegeneration. *Nat. Chem. Biol.* **9**, 586–592 (2013).

18. L. Wei *et al.*, Live-cell imaging of alkyne-tagged small biomolecules by stimulated Raman scattering. *Nat. Methods*. **11**, 410–2 (2014).

19. S. Hong *et al.*, Live-cell stimulated Raman scattering imaging of alkyne-tagged biomolecules. *Angew. Chemie Int. Ed.* **53**, 5827–5831 (2014).

20. H.-J. van Manen, A. Lenferink, C. Otto, Noninvasive imaging of protein metabolic labeling in single human cells using stable isotopes and Raman microscopy. *Anal. Chem.* **80**, 9576–9582 (2008).

21. L. Wei, Y. Yu, Y. Shen, M. C. Wang, W. Min, Vibrational imaging of newly synthesized proteins in live cells by stimulated Raman scattering microscopy. *Proc. Natl. Acad. Sci.* **110**, 11226–11231 (2013).

22. L. Wei *et al.*, Imaging Complex Protein Metabolism in Live Organisms by Stimulated Raman Scattering Microscopy with Isotope Labeling. *ACS Chem. Biol.* **10**, 901–908 (2015).

23. Y. Shen, F. Xu, L. Wei, F. Hu, W. Min, Live-cell quantitative imaging of proteome degradation by stimulated Raman scattering. *Angew. Chem. Int. Ed. Engl.* **53**, 5596–9 (2014).

24. Y. Yu, P. V Ramachandran, M. C. Wang, Shedding new light on lipid functions with CARS and SRS microscopy. *Biochim. Biophys. Acta*. **1841**, 1120–1129 (2014).

25. A. Syed, E. A. Smith, Raman Imaging in Cell Membranes, Lipid-Rich Organelles , and Lipid Bilayers, 1–21 (2017).

26. C. Matthäus *et al.*, Noninvasive imaging of intracellular lipid metabolism in macrophages by Raman microscopy in combination with stable isotopic labeling. *Anal. Chem.* **84**, 8549–8556 (2012).

27. A. Alfonso-García, S. G. Pfisterer, H. Riezman, E. Ikonen, E. O. Potma, D38-cholesterol as a Raman active probe for imaging intracellular cholesterol storage. *J. Biomed. Opt.* **21**, 61003 (2016).

28. H. J. Lee *et al.*, Assessing Cholesterol Storage in Live Cells and C. elegans by Stimulated Raman Scattering Imaging of Phenyl-Diyne Cholesterol. *Sci. Rep.* **5**, 7930 (2015).

29. F. Hu, L. Wei, C. Zheng, Y. Shen, W. Min, Live-cell vibrational imaging of choline metabolites by stimulated Raman scattering coupled with isotope-based metabolic labeling. *Analyst*. **139**, 2312-2317 (2014).

30. H.-J. van Manen, Y. M. Kraan, D. Roos, C. Otto, Single-cell Raman and fluorescence microscopy reveal the association of lipid bodies with phagosomes in leukocytes. *Proc. Natl. Acad. Sci. U. S. A.* **102**, 10159–64 (2005).

31. C. Stiebing *et al.*, Real-time Raman and SRS imaging of living human macrophages reveals cell-to-cell heterogeneity and dynamics of lipid uptake. *J. Biophotonics* (2017), doi:10.1002/jbio.201600279.

32. X. S. Xie, Living Cells as Test Tubes. *Science*. **312**, 228–230 (2006).

33. T. Weeks, I. Schie, L. J. den Hartigh, J. C. Rutledge, T. Huser, Lipid-cell interactions in human monocytes investigated by doubly-resonant coherent anti-Stokes Raman scattering microscopy. *J Biomed Opt*. **16**, 21117 (2011).

34. D. Zhang, M. N. Slipchenko, J.-X. Cheng, Highly Sensitive Vibrational Imaging by

Femtosecond Pulse Stimulated Raman Loss. *J. Phys. Chem. Lett.* **2**, 1248–1253 (2011).

35. D. Fu *et al.*, Quantitative chemical imaging with multiplex stimulated Raman scattering microscopy. *J. Am. Chem. Soc.* **134**, 3623–26 (2012).

Chapter 2

Live-cell quantitative imaging of proteome degradation by stimulated Raman scattering

The content of this chapter has been published in

Y. Shen, F. Xu, L. Wei, F. Hu, W. Min, Live-cell quantitative imaging of proteome degradation by stimulated Raman scattering. Angew. Chem. Int. Ed. Engl. **53**, 5596–9 (2014).

2.1 Abstract

Protein degradation is a regulatory process essential to cell viability, and its dysfunction is implicated in many diseases such as aging and neurodegeneration. Here we report stimulated Raman scattering microscopy coupled with metabolic labeling of ^{13}C-phenylalanine to visualize protein degradation in living cells with subcellular resolution. We choose the ring breathing modes of endogenous ^{12}C-phenylalanine and incorporated ^{13}C-phenylalanine as protein markers for the original and nascent proteome, respectively, and quantified the decay of the former through ratio maps. We demonstrated time dependent imaging of proteomic degradation in mammalian cells under steady-state condition and various perturbations including oxidative stress, cell differentiation, and huntingtin protein aggregation.

2.2 Introduction

Proteins that are abnormal or no longer in function are actively removed by protein degradation. It is essential to cell viability as a regulatory control in response to physiological and pathological cues (*1*). Indeed, disruption of proteolysis machinery has been implicated in aging and neurodegenerative disorders, where cells are exposed to the danger of oxidatively damaged proteins or aggregation-prone proteins (*2*, *3*). Extensive efforts have been made to quantify cellular protein degradation. Traditional autoradiography uses pulse-chase labeling of radioactive amino acids (e.g., ^{35}S-methionine) with the treatment of protein synthesis inhibitor (*4*). Later, Stable Isotope Labeling by Amino Acids in Cell Culture (SILAC) was developed in tandem with

mass spectrometry, through quantifying the relative amount of 'heavy' and 'light' peptides (*5–7*).

However, both of them measure proteome from a collective lysed cell culture and are unable to

reveal cell-cell or subcellular variation. Even when coupled to secondary ion microscopy in

multi-isotope imaging mass spectrometry (MIMS), its invasive detection does not allow live cell

measurement (*8, 9*). Besides autoradiography and mass spectrometry, fluorescence reporter

library has enabled proteome half life determination after a photo-bleach chase (*10*). But it

requires creation of genomic fusion library, thus is not generally applicable to all cell types.

Here we report a general strategy that visualizes the degradation of the overall proteome in living

cells with subcellular resolution by coupling metabolic labeling of ^{13}C-phenylalanine (^{13}C-Phe)

with stimulated Raman scattering (SRS) microscopy. Specifically, we choose the characteristic

ring-breathing modes of endogenous ^{12}C-Phe and metabolically incorporated ^{13}C-Phe as the

Raman spectroscopic markers for the old and new proteome, respectively. Proteomic degradation

can then be imaged by SRS in living cells by ratio maps of ^{12}C/(^{12}C+^{13}C), where total proteome

is represented by the sum of ^{12}C-Phe and ^{13}C-Phe. We show the utility of our technique by

measuring quasi steady-state proteome degradation in mammalian cell lines and mouse

hippocampal neurons, as well as studying perturbation caused by oxidative stress, cell

differentiation and protein aggregation process. Technically, this is the first time that ^{13}C-labeled

amino acid is used together with nonlinear vibrational microscopy. Our proteome imaging

method is capable of revealing cell's global metabolic activity with exquisite spatial resolution.

2.3 Results

2.3.1 Choice of phenylalanine as marker for ratiometric protein turnover imaging

The choice of phenylalanine as proteome marker is critical for labeling. First, since it is an essential amino acid that has to be supplied in culture medium, the metabolic incorporation of its ^{13}C isotopologue could distinguish the nascent proteome from the original. Second, its ring-breathing mode exhibits a strong, isolated sharp peak (FWHM~10 cm^{-1}) at 1004 cm^{-1} **(Figure 2.1)**, enabling a resolvable shift upon ^{13}C substitution. In contrast, Amide I band (around 1655 cm^{-1}) and CH$_3$ stretching (around 2940cm^{-1}) **(Figure 2.1 B)** as protein markers (*11–14*) are not only broadband but also suffer from severe interference from lipids (around 1650 cm^{-1} and 2850 cm^{-1}), nucleic acids (around 2950 cm^{-1}), and water (around 3100 cm^{-1}). Third, compared to the protein-bound phenylalanine concentration of 90 mM (*15*), the intracellular free phenylalanine pool (0.5 mM) (*16*) is essentially negligible. Moreover, since ^{13}C-Phe is supplied in large excess, ^{12}C-Phe from degraded proteins is seldom recycled. Microscopy wise, the advantage of SRS microscopy lies in its superb sensitivity, well-preserved spectra, and linear concentration dependence, thus is well suited for quantitative live imaging (*13, 17–19*). On contrary, another nonlinear microscopy, coherent anti-Stokes Raman scattering, has drawbacks such as non-resonant background, spectral distortion, complex concentration dependence, and coherent image artifact (*20*).
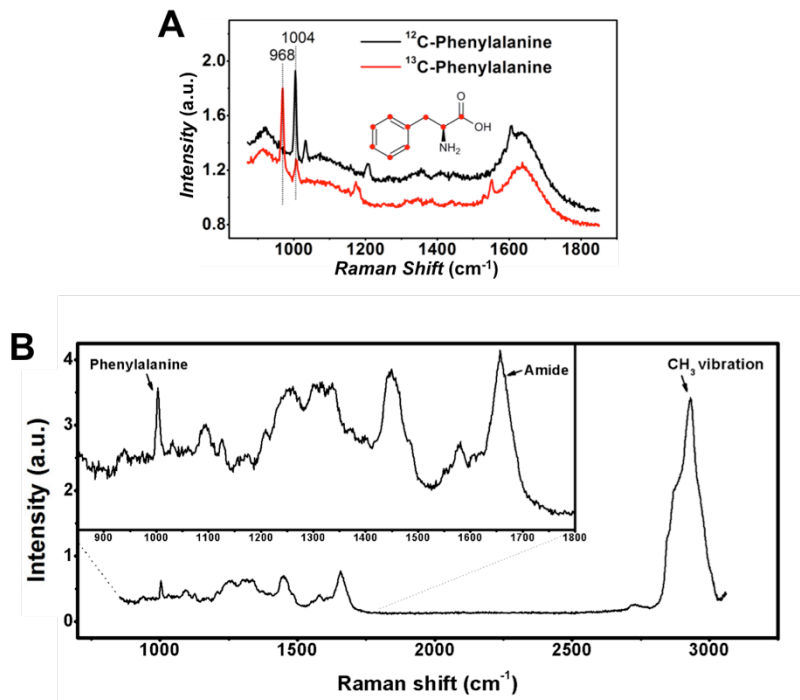
Figure 2.1 ¹³C-Phe labeling provides a resolvable peak beyond cellular background. (A) Spontaneous Raman spectra of ¹²C-Phe (black) and ¹³C-Phe (red) with vibrational frequency shift from 1004 cm⁻¹ to 968 cm⁻¹. Inset shows the structure of phenylalanine with ¹³C sites denoted by red dots. **(B)** A spontaneous Raman spectrum of a non-labeled fixed HeLa cell. Background from water and glass has been subtracted. The broad band from 2800 cm⁻¹ to 3050 cm⁻¹, which is often assigned to protein CH_3, contains overlapping signals from lipid, protein, nucleic acids, and water. Inset shows part of the fingerprint region from 850 cm⁻¹ to 1800 cm⁻¹. Amide I band, centered at 1655 cm⁻¹, is also a broad band with interference from unsaturated lipid and water. In contrast, phenylalanine is an isolated sharp peak at 1004 cm⁻¹, sitting on a flat baseline from 950 cm⁻¹ to 1050 cm⁻¹.

2.3.2 Metabolic labeling by ¹³C-phenylalanine

We first tested the vibrational frequency shift of phenylalanine by ¹³C labeling. As vibration frequency is inversely proportional to the square root of reduced mass, and also taking H atoms into account, the Raman peak of uniformly-¹³C-labeled phenylalanine (i.e., ¹³C-Phe) should red

shift to $1004 \times \sqrt{13/14} = 967.5$ cm^{-1}, which is close to the measured 968 cm^{-1} in buffer solution **(Figure 2.1 A,** red**)**. This peak shift has also been observed in microbes fed with ^{13}C-glucose (*21*). Some attention needs to be paid to the signal extraction as both ^{12}C- and ^{13}C- Phe Raman peaks sit on a flat baseline (950~1050 cm^{-1}) **(Figure 2.1 B)**. Since SRS preserves spontaneous Raman spectrum, we adopt a simple and robust subtraction strategy to determine the net phenylalanine signal: using the central valley at 986 cm^{-1} to represent the baseline background and then subtracting it from images at the two peaks (968 cm^{-1} and 1004 cm^{-1}). Besides, we notice that there is a smaller peak from ^{13}C-Phe overlapping with the 1004 cm^{-1} peak of ^{12}C-Phe. After treating this as a linear contribution from ^{13}C channel to ^{12}C channel with a coefficient of 0.14, we can obtain pure ^{13}C and ^{12}C signals as $I(^{13}C) = I_{968} - I_{986}$ and $I(^{12}C) = I_{1004} - I_{986} - 0.14 \cdot I(^{13}C)$, I represents the intensity from spectrum or image.

We then demonstrated our method in cultured HeLa cells. After cells were incubated with 0.8 mM ^{13}C-Phe substituted medium, time dependent spontaneous Raman spectra were measured **(Figure 2.2)** from fixed cells. The endogenous ^{12}C peak shows an apparent decay while the ^{13}C peak increases concurrently over time, proving the success of metabolic incorporation. The normalized ratios (^{12}C/(^{12}C+^{13}C)) verses time were fitted with an exponential decay ($\tau = 43 \pm 4$ hrs) **(Figure 2.2,** inset**)**.
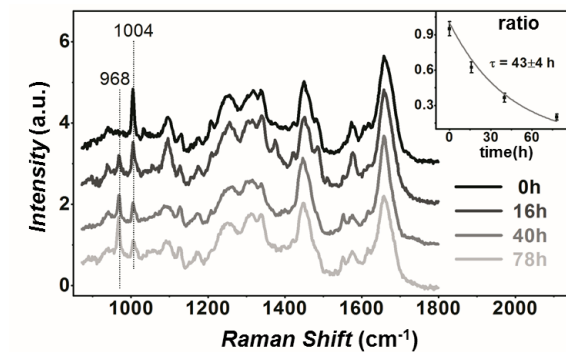
Figure 2.2 Time dependent spontaneous Raman spectra of HeLa cells. The spectra clearly show decline of 1004 cm^{-1} peak and rise of 968 cm^{-1} peak. The center at 986 cm^{-1} is used in background subtraction for SRS images. Inset: single exponential fitting of $^{12}C/(^{12}C+^{13}C)$ ratio obtained from spectra.

2.3.3 Ratiometric imaging of protein turnover by SRS imaging

To obtain ratiometric maps, we set up SRS microscope similarly as previously described (*11*). Live cell SRS images were acquired at three Raman shifts (968 cm^{-1}, 986 cm^{-1}, 1004 cm^{-1}). After background subtraction, gradual weakening of the resulting ^{12}C channels clearly indicates the degradation of old proteome **(Figure 2.3 A)**. As expected, the amount of total proteome almost remains unchanged in quasi steady state, as confirmed by the sum images of ^{12}C and ^{13}C channels. Ratio maps were calculated as normalized $^{12}C/(^{12}C+^{13}C)$ to account for cell-cell variation and laser power fluctuation. One can readily infer how fast the degradation is from these ratio maps. To compare our results with those collective cell culture results, we fitted averaged ratios with single exponential decay ($\tau = 40\pm1$ hrs) **(Figure 2.3 B)**. This is close to what was determined earlier from the spectra and also matches the 35 hrs reported using mass spectrometry (*22*). We also examined the effect of oxidative stress on protein turnover. Reactive

oxygen species (ROS) production and cellular anti-oxidant defense are normally balanced as part of homeostasis. However, under severe oxidative stress, accumulation of ROS will harm the proteolysis machinery thus retarding protein degradation (*2, 23*). We determined the proteomic degradation of HeLa cells treated with 200 μM H_2O_2 by 24 hr ^{13}C-Phe labeling. Cells treated with H_2O_2 exhibit a ~25% higher ^{12}C ratio than control, indicating a slower protein degradation under oxidative stress **(Figure 2.3 C)**.
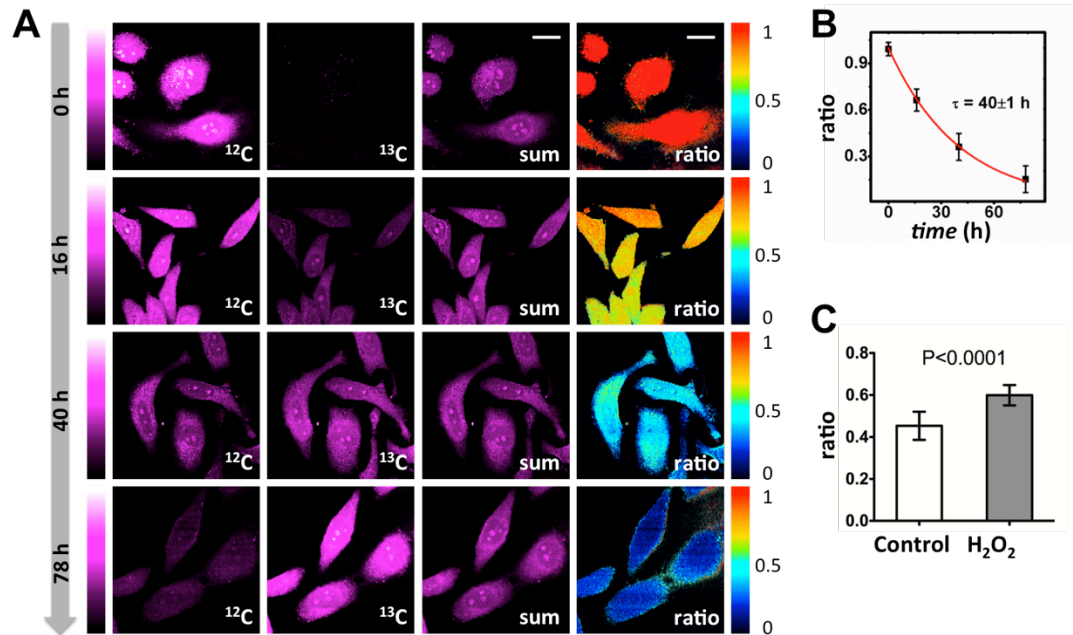
Figure 2.3 SRS imaging reveals protein degradation kinetics in HeLa cells. (A) Background subtracted ^{12}C- and ^{13}C-Phe SRS images and their sum and ratio maps of HeLa cells show obvious decay in ^{12}C channel and increase in ^{13}C channel over time. Ratio images decay from ~1.0 to ~0.2. Scale bar, 20μm. **(B)** Single exponential fitting of ^{12}C ratio obtained from SRS images. Error bar, standard deviation of ratio. **(C)** Treatment of H_2O_2 results in a slower degradation in HeLa cells incubated with ^{13}C-Phe for 24 hrs. Control: 0.45±0.07, n=12; H_2O_2 treated: 0.60±0.05, n=14. n is number of cells analyzed.
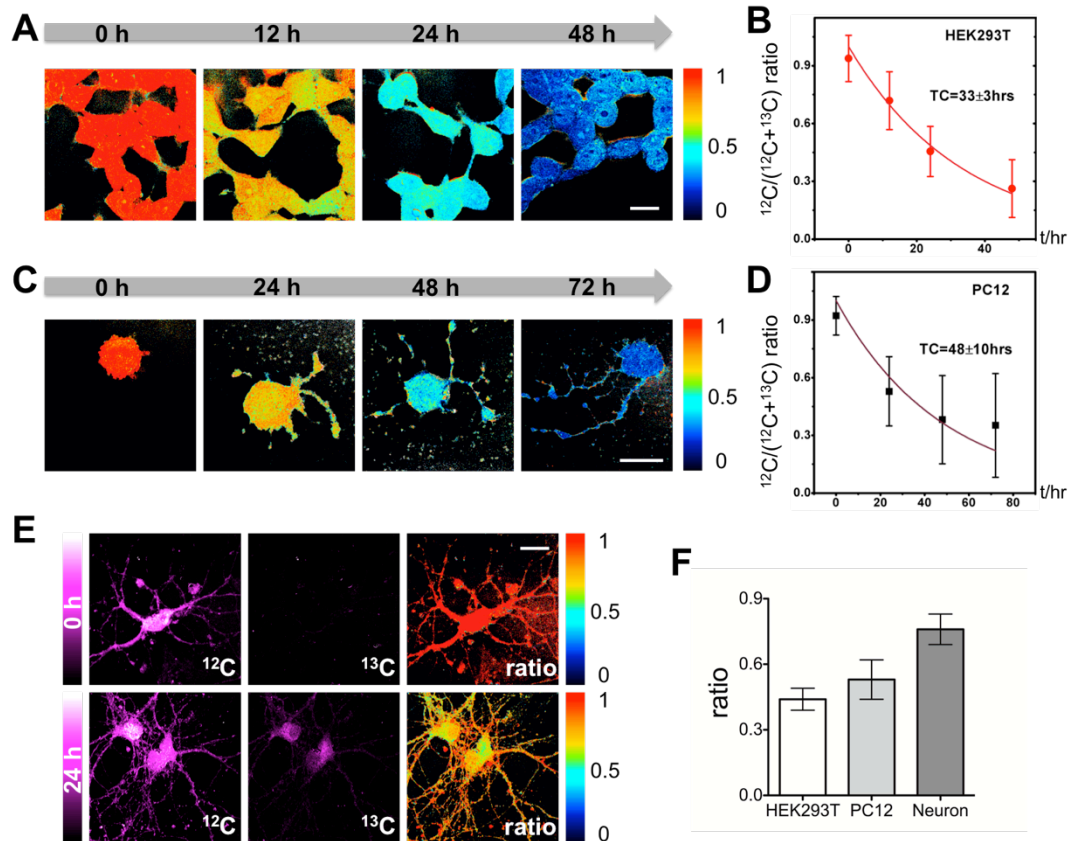
Figure 2.4 SRS imaging reveals protein degradation kinetics in HEK293T, PC12 and primary neurons. (A and B) Time dependent $^{12}C/(^{12}C+^{13}C)$ SRS ratio maps (A) and single-exponential fitting of the averaged ratio (B) for HEK293T cells. **(C and D)** Time dependent $^{12}C/(^{12}C+^{13}C)$ SRS ratio maps (C) and single-exponential fitting of the averaged ratio (D) for PC12 cells during differentiation induced by NGF-β. Error bars in (B) and (D), standard deviation. **(E)** SRS images of ^{12}C and ^{13}C channels and calculated $^{12}C/(^{12}C+^{13}C)$ ratio images for mouse hippocampal neurons incubated with ^{13}C-Phe for 0 hr and 24 hrs. **(F)** Comparison of $^{12}C/(^{12}C+^{13}C)$ ratios at 24 hr incubation among HEK293T, PC12, and neurons, indicating that neurons have a slower protein degradation. Scale bars, 20 μm.

Our technique could readily be applied to study protein degradation of other cell lines or primary cells under either steady state or differentiation conditions. For example, in live HEK293T cells **(Figure 2.4 A)**, they were found to follow similar decay patterns but exhibited a faster kinetics

with $\tau = 33\pm3$ hrs **(Figure 2.4 B)**. This is reasonable due to their faster growth than HeLa cells. We went on to obtain SRS images during PC12 cell differentiation induced by NGF-β in the presence of ^{13}C-Phe **(Figure 2.4 C)**, which reveals protein degradation kinetics with $\tau = 48\pm10$ hrs **(Figure 2.4 D)**. We further demonstrates in primary mouse hippocampal neuron culture **(Figure 2.4 E)** using same concentration of ^{13}C-Phe. Protein degradation clearly takes place after 24 hrs, but much more slowly **(Figure 2.4 F)**, in consistence with the profound metabolic difference between neurons (post-mitotic) and HeLa or HEK293T cells (immortal).

2.3.4 Heterogeneity of protein turnover in polyQ protein aggregation model

Finally we studied the impact of protein aggregation on proteomic degradation with subcellular resolution. It is generally believed that polyQ expansion is one of the genetic reasons for neuron degenerative disorders such as Huntington's disease (*24*). Overexpression of mutant huntingtin (Htt) could overwhelm the capacity of cellular proteolysis and form aggregates as inclusion bodies (IBs). However, the precise role of aggregate formation is still under debate. We expressed a fluorescent protein (mEos2) tagged N-terminal fragment of the mutant Htt protein, mEos2-Htt-Q94, in HEK293T cells as a protein aggregation model. 24 hrs after plasmid transfection, cells were switched to ^{13}C-Phe medium and imaged 24 hrs and 48 hrs later **(Figure 2.5 A)**. mEos2 fluorescence readily revealed bright cluster regions as IBs. The corresponding regions in the ratio maps **(Figure 2.5 B,** arrow**)** show severely retarded degradation, confirming proteolysis inability inside IBs. Thus, the subcellular mapping capability of our technique is

indispensable to resolve this compartmentalized impairment of metabolic activity. We notice that SRS signal could be interfered by the two-photon absorption of mEos2. To exclude this possibility, we photo-bleached the mEos2 and restored SRS images (data not shown).
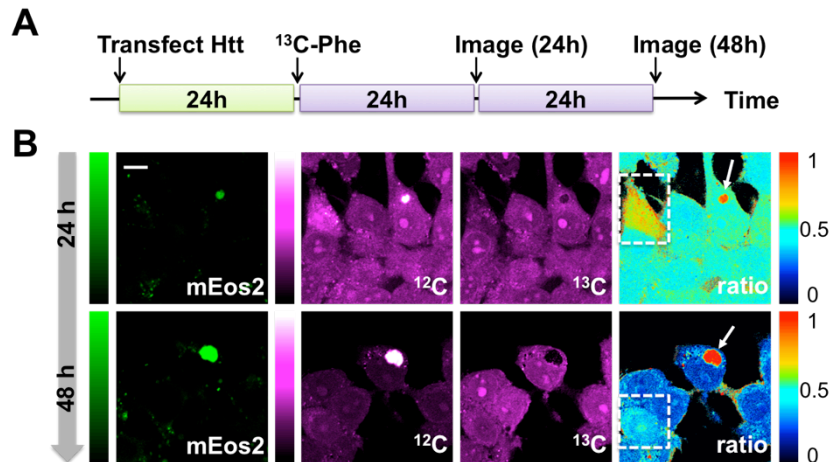
Figure 2.5 Proteomic degradation of HEK293T cells during Htt-Q94 aggregation. (A) Experimental timeline. **(B)** HEK293T cells were imaged after 24-hr or 48-hr expression of Htt-Q94-mEos2. First column: mEos2 fluorescence images indicate the formation of inclusion body. Second and third columns: SRS images at ^{12}C and ^{13}C channels. Last column: SRS ratio maps with subcellular resolution reveal retarded degradation inside inclusion bodies (arrow) as well as pronounced slowdown of cytoplasmic protein degradation within a few cells (boxed). Scale bar, 10 μm.

Remarkable cell-to-cell variations were observed, shedding light on the functional role of IB formation. While the degradation rates for cytoplasmic proteins in most tested cells were very similar to those non-transfected cells **(Figure 2.4 A)**, a few ones with hotter colors **(Figure 2.5 B, boxed)** exhibited pronouncedly slower degradation. Interestingly, there exist only diffusive Htt-Q94 (or small IBs) in their fluorescence images. In contrast, cells containing large IBs

display normal degradation rate for the cytoplasmic proteins. Hence, our observation lends support to the emerging hypothesis that the diffusive oligomers of aggregation-prone proteins might become toxic to cells by gradually interfering with proteasome machinery, while the formation of inclusion bodies may actually play a neuroprotective role by sequestering the diffusive toxic species (*25*, *26*).

2.4 Conclusion

In summary, we have demonstrated the coupling of SRS microscopy with ^{13}C-Phe labeling in quantitative imaging of protein degradation. Compared to existing approaches, our method is unique in several aspects. First, ^{13}C stable isotope introduces minimal perturbation; meanwhile SRS offers non-invasive detection with subcellular resolution. On the contrary, neither autoradiography nor mass spectrometry can probe living cells. Second, the intrinsic contrast from ^{12}C-Phe offers an endogenous marker for the preexisting proteome. This is hardly achievable for bioorthogonal alkyne tagging (*27–29*), which can only visualize the newly incorporated tags. Likewise, the recently reported deuterium labeling approach only allows imaging of proteome synthesis but not degradation (*11*) (note that monitoring the decay of C-D signal after pulse-chase of deuterated amino acid would not work, since the C-D signal would gradually transfer from protein to other metabolites such as lipids (*30*)). Last, unlike analysis on individual proteins, our proteomic approach reveals the global proteolysis activity, a phenotype in many

diseases, thus our technique can be applied to drug screening where cell's proteolysis status is a key functional observable.

2.5 Methods

Stimulated Raman Scattering Microscopy

We use picoEmerald laser system (Applied Physics and Electronics) as light source for SRS microscopy. It produces Pump (tunable from 720 nm – 990 nm) and Stokes (1064 nm) beams simultaneously with 80 MHz repetition. For 968, 986 and 1004 cm^{-1}, the wavelengths of pump laser are 964.5, 962.8 and 961.1 nm, respectively. Pulse durations for two beams are 6 ps and 5-6 ps, respectively, (measured bandwidth for OPO laser is 0.2 nm), corresponding to 5 cm^{-1} in excitation spectral resolution. Stokes beam is modulated at 8 MHz by an internal electro-optic modulator. The spatially and temporally overlapped Pump and Stokes beams are introduced into an inverted multiphoton laser scanning microscopy (FV1200MPE, Olympus), and then focused onto the sample by a 60X water objective (UPlanAPO/IR, 1.2 N.A., Olympus). Transmitted Pump and Stokes beams are collected by a high N.A. condenser lens (oil immersion, 1.4 N.A., Olympus) and pass through a bandpass filter (890/220 CARS, Chroma Technology) to filter out Stokes beam. A large area (10×10 mm) Si photodiode (FDS1010, Thorlabs) is used to measure the remaining Pump beam intensity. We apply 64 V DC voltage on the photodiode to increase saturation threshold and reduce response time. The output current is terminated by a 50Ω terminator and pre-filtered by an 8-MHz band-pass filter (KR 2724, KR electronics) to reduce

laser and scanning noise. The signal is then demodulated by a lock-in amplifier (SR844, Stanford Research Systems) at the modulation frequency. The in-phase X output is fed back to the analog channel (FV10-ANALOG) of the microscope. Image acquisition speed is limited by 20 μs time constant set for the lock-in amplifier. Correspondingly, we use 100 μs pixel dwell time, which gives a speed of 25 s/frame for a 512-by-512-pixel field of view. Laser powers on sample are measured to be 130 mW for modulated Stokes beam and 120 mW for Pump beam. Laser powers are monitored through image acquisition by an internal power meter and power fluctuation are controlled within 2% by the laser system. 16-bit grey scale images are acquired by Fluoview software.

Spontaneous Raman Spectroscopy

Spontaneous Raman spectra were acquired using an upright confocal Raman spectrometer (InVia Raman microscope; Renishaw). A 532 nm YAG laser is used to illuminate the sample with a power of 27 mW on sample through a 50×, N.A. 0.75 objective (NPLAN EPI; Leica). Data acquisition was performed after 80-second integration by the WiRE software. Fixed HeLa cells are used and glass background from the coverslip is subtracted by measuring signal from non-cell region near the target cell. The spectra are normalizd according to Amide I band.

Cell Culture and ^{13}C-Phe Labeling

^{13}C-Phe labeling in mammalian cell lines and mouse hippocampal neuron cells ^{13}C-Phe supplemented DMEM for HeLa (ATCC), HEK293T (ATCC) cells were made using ^{13}C$_9$,^{15}N-L-phenylalanine (Sigma) (final concentration: 0.8 mM) and other regular amino acids, salts and vitamins, with 10% FBS and penicillin-streptomycin (Invitrogen). ^{13}C-Phe supplemented DMEM for PC12 (ATCC) differentiation is similar except for low serum concentration (1% FBS) and a supplement of 50 ng/mL NGF-β (murine recombinant, Sigma). HeLa or HEK293T or PC12 cells were seeded onto a coverslip in regular medium and then subjected to medium change or induction to differentiation. For incubation time longer than 48 hrs, the medium is refreshed once to prevent exhaustion of nutrition. For experiments with mouse hippocampal neuron culture, ^{13}C-Phe supplemented Neurobasal Medium was used for labeling ~8 day old neurons. After an intended incubation period, the coverslips were taken out and used to make a chamber filled with PBS for SRS imaging. Cells for spontaneous Raman spectra measurement were fixed using cold 4% paraformaldehyde in PBS for 15 min, then washed twice with PBS.

For studying huntingtin aggregation, HEK293T cells were transfected with 3μg Htt-Q94 (Addgene, tagged with mEos2 or SNAP) plasmid using Transfection Reagent (FuGene, Promega) in regular DMEM. After 24 hr incubation, the medium is switched to ^{13}C-Phe supplemented DMEM. The formation of inclusion body was confirmed by mEos2 fluorescence, which is taken with the same laser scan confocal microscope upon illumination by 488 nm laser (400μW).

Image processing and data analysis Images are assigned color by ImageJ. Ratio maps are calculated by Matlab2012. Single exponential fitting is performed in Origin8.0. Student t test and P value calculation is performed in Prism5.0.

2.6 References

1. A. L. Goldberg, Protein degradation and protection against misfolded or damaged proteins. *Nature*. **426**, 895–899 (2003).

2. R. Shringarpure, K. Davis, Protein turnover by the proteasome in aging and disease. *Free Radic. Biol. Med.* **32**, 1084–1089 (2002).

3. A. Tsvetkov, M. Arrasate, S. Barmada, Proteostasis of polyglutamine varies among neurons and predicts neurodegeneration. *Nat. Chem. Biol.* **9**, 586–592 (2013).

4. A. Bachmair, D. Finley, A. Varshavsky, In vivo half-life of a protein is a function of its amino-terminal residue. *Science.* **234**, 179–186 (1986).

5. M. Mann, Functional and quantitative proteomics using SILAC. *Nat. Rev. Mol. Cell Biol.* **7**, 952–8 (2006).

6. M. Larance, Y. Ahmad, K. J. Kirkwood, T. Ly, A. I. Lamond, Global subcellular characterization of protein degradation using quantitative proteomics. *Mol. Cell. Proteomics.* **12**, 638–650 (2013).

7. M. K. Doherty, D. E. Hammond, M. J. Clague, S. J. Gaskell, R. J. Beynon, Turnover of the Human Proteome : Determination of Protein Intracellular Stability by Dynamic SILAC research articles. *J. Proteome Res.* **8**, 104–112 (2009).

8. D.-S. Zhang *et al.*, Multi-isotope imaging mass spectrometry reveals slow protein turnover in hair-cell stereocilia. *Nature.* **481**, 520–524 (2012).

9. M. L. Steinhauser *et al.*, Multi-isotope imaging mass spectrometry quantifies stem cell division and metabolism. *Nature.* **481**, 516–9 (2012).

10. E. Eden *et al.*, Proteome half-life dynamics in living human cells. *Science.* **331**, 764–768 (2011).

11. L. Wei, Y. Yu, Y. Shen, M. C. Wang, W. Min, Vibrational imaging of newly synthesized proteins in live cells by stimulated Raman scattering microscopy. *Proc. Natl. Acad. Sci.* **110**, 11226–11231 (2013).

12. D. Zhang *et al.*, Quantitative vibrational imaging by hyperspectral stimulated Raman scattering microscopy and multivariate curve resolution analysis. *Anal. Chem.* **85**, 98–106 (2013).

13. Y. Ozeki *et al.*, High-speed molecular spectral imaging of tissue with stimulated Raman scattering. *Nat. Photonics*. **6**, 845–851 (2012).

14. X. Zhang *et al.*, Label-free live-cell imaging of nucleic acids using stimulated Raman scattering microscopy. *Chemphyschem*. **13**, 1054–9 (2012).

15. H.-J. van Manen, A. Lenferink, C. Otto, Noninvasive imaging of protein metabolic labeling in single human cells using stable isotopes and Raman microscopy. *Anal. Chem.* **80**, 9576–9582 (2008).

16. K. Piez, H. Eagle, The free amino acid pool of cultured human cells. *J. Biol. Chem.* **231**, 533–545 (1958).

17. C. W. Freudiger *et al.*, Label-free biomedical imaging with high sensitivity by stimulated Raman scattering microscopy. *Science*. **322**, 1857–61 (2008).

18. B. G. Saar *et al.*, Video-rate molecular imaging in vivo with stimulated Raman scattering. *Science.* **330**, 1368–1370 (2010).

19. P. Wang *et al.*, Label-free quantitative imaging of cholesterol in intact tissues by hyperspectral stimulated Raman scattering microscopy. *Angew. Chem. Int. Ed. Engl.* **52**, 13042–6 (2013).

20. W. Min, C. W. Freudiger, S. Lu, X. S. Xie, Coherent nonlinear optical imaging: beyond fluorescence microscopy. *Annu. Rev. Phys. Chem.* **62**, 507–530 (2011).

21. H. N. Noothalapati Venkata, S. Shigeto, Stable isotope-labeled Raman imaging reveals dynamic proteome localization to lipid droplets in single fission yeast cells. *Chem. Biol.* **19**, 1373–80 (2012).

22. S. B. Cambridge *et al.*, Systems-wide proteomic analysis in mammalian cells reveals conserved, functional protein turnover. *J. Proteome Res.* **10**, 5275–5284 (2011).

23. N. Breusing, T. Grune, Regulation of proteasome-mediated protein degradation during oxidative stress and aging. *Biol. Chem.* **389**, 203–209 (2008).

24. H. Y. Zoghbi, H. T. Orr, Glutamine repeats and neurodegeneration. *Annu. Rev. Neurosci.* **23**, 217–247 (2000).

25. M. Arrasate, S. Mitra, E. S. Schweitzer, M. R. Segal, S. Finkbeiner, Inclusion body formation reduces levels of mutant huntingtin and the risk of neuronal death. *Nature.* **431**, 805–810 (2004).

26. J. Tyedmers, A. Mogk, B. Bukau, Cellular strategies for controlling protein aggregation. *Nat. Rev. Mol. Cell Biol.* **11**, 777–88 (2010).

27. D. C. Dieterich *et al.*, In situ visualization and dynamics of newly synthesized proteins in rat hippocampal neurons. *Nat. Neurosci.* **13**, 897–905 (2010).

28. L. Wei *et al.*, Live-cell imaging of alkyne-tagged small biomolecules by stimulated Raman scattering. *Nat. Methods.* **11**, 410–2 (2014).

29. L. Lin *et al.*, A bioorthogonal Raman reporter strategy for SERS detection of glycans on live cells. *Angew. Chem. Int. Ed. Engl.* **52**, 7266–71 (2013).

30. F. Hu, L. Wei, C. Zheng, Y. Shen, W. Min, Live-cell vibrational imaging of choline metabolites by stimulated Raman scattering coupled with isotope-based metabolic labeling. *Analyst* (2014), doi:10.1039/c3an02281a.

Chapter 3

Membrane phase behavior and implication in biological membrane

3.1 Chapter overview: membrane lipid bilayer and phases

Membrane encloses the boundary of life. They are composed of amphiphilic lipid molecules containing a hydrophilic head and a long hydrocarbon tail. These molecules self-assemble as a bilayer in aqueous environment, with the hydrophilic head facing outward, in order to avoid hydrophobic interaction between the hydrocarbons and water. Thus the biological membrane has long been perceived as a fluidic barrier and neutral two-dimensional solvent for membrane proteins, as in the textbook 'fluid mosaic' model (lipid bilayer inserted by membrane proteins) (*1*). Yet this perception is over-simplified from the current point of view, given the enormous diversity of lipids and their intricate influence on bilayer property. For example, the random mixing of lipids and proteins in the 'fluid mosaic' model cannot explain how proteins are selectively sorted to the plasma membrane after they are made, or why certain lipids and proteins cluster in the plasma membrane of eukaryotic cell (*2*).

The above functions point to the capability of biological membrane (complex of protein and lipids) to segregate laterally. It was in fact found earlier that lateral segregation is an inherent property of lipids, and is dictated by the phase behavior of the bilayer. Since then, the study of membrane phase behavior has attracted scientists' interest for decades, not only for its implication in the organization principle of biological membrane, but also as an intriguing physicochemical problem by its own. Studies of *in vitro* model membrane have revealed three major phases existing in lipid bilayer: solid ordered phase (S_o, also known as gel phase), liquid

disordered phase (L_d, also known as liquid crystalline phase), and liquid ordered phase (L_o) (*3*).

They are defined by the spatial arrangement and motional freedom of the lipid molecules

(Figure 3.1). The S_o phase is characterized by highly ordered intermolecular packing, and

essentially frozen in-bilayer movement (diffusion coefficient $D = 10^{-3}$ μm^2/s). In comparison, the

L_d phase assumes random conformation in the acyl chains, and molecules can freely diffuse

inside ($D = 1$ μm^2/s). The third phase, L_o phase, is a cholesterol-enriched phase. It possesses high

order as in S_o phase, but retains fast diffusion like in L_d phase.

unsaturated lipids (low-T_m)

saturated lipids (high-T_m)

cholesterol

Liquid disordered (L_d)
low conformational order, fast lateral diffusion

Liquid ordered (L_o)
high conformational order, fast lateral diffusion

Solid ordered (S_o)
high conformational order, slow lateral diffusion
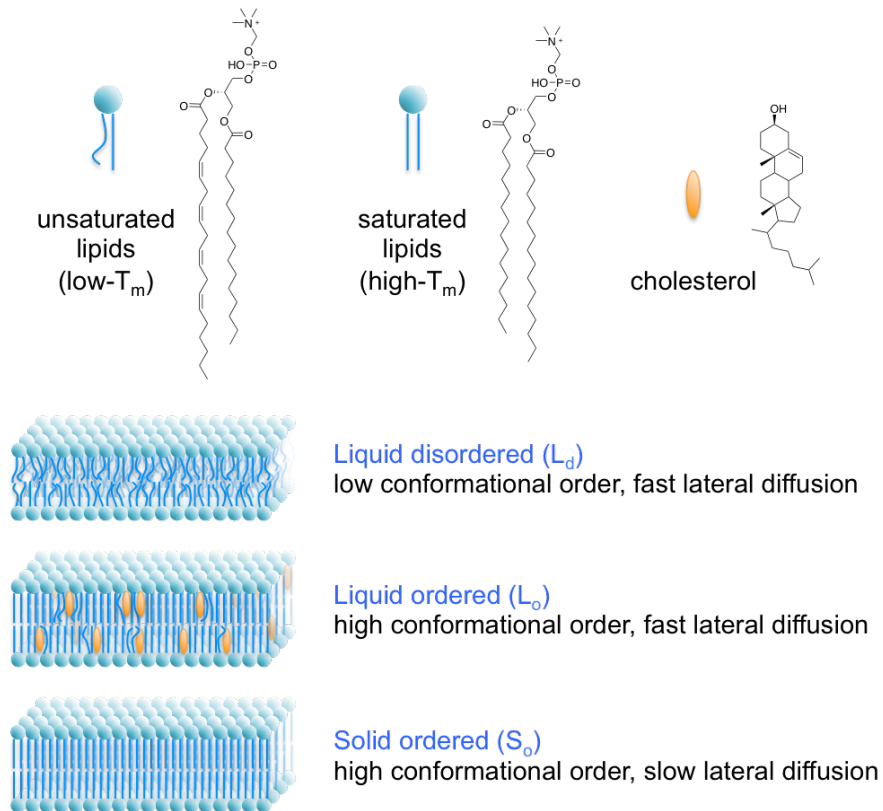
Figure 3.1 Molecular structures of common lipid molecules in biological membrane and three major phases observed in model membranes. Structures are shown for an unsaturated phosphotidylcholine (PC), a saturated PC, and cholesterol. Cartoons are shown for L_d, L_o and S_o phases, together with description of their distinct properties.

Depending on the temperature as well as the chemical composition, a bilayer could assume uniform phase or co-existence of multiple phases. In the latter case, immiscible domains will form, which accounts for spontaneous lateral segregation in membrane. Below I will briefly introduce the concept of main phase transition and lateral phase separation in model membranes, as well as how this translates into understanding of biological membranes. For more elaborative description and discussion, the reader can refer to earlier instructive and inspiring reviews (*3–10*).

3.2 Main phase transition of lipid bilayer

The main phase transition (*11*) describes the temperature-dependent S_o-to-L_d phase transition of lipid bilayer formed by single component, e.g. **di**palmitoyl**p**hosphatidyl**c**holine (DPPC). At low temperature, the DPPC bilayer adopts S_o phase, with all the acyl chains aligned and minimal lateral movement. The CH_2 moieties are in the trans conformation as a low-energy state. Upon increasing the temperature, the acyl chains undergo trans-gauche isomerization and the bilayer becomes less ordered and more fluidic towards the L_d phase. Conformational change in one molecule causes it bumping into its adjacent molecules, and therefore triggers a cooperative molecular motion in a long distance. Such cooperativity is then reflected in the 'melting curve', where physical properties of the bilayer changes abruptly at a temperature called 'main phase transition temperature' (T_m). T_m is an intrinsic physicochemical property of the lipid molecule, and reflects the propensity of the molecule to assume ordered structure in a mixture. Therefore it

is one of the most important parameters to describe the compositional features of a lipid mixture.

Some general trend could be inferred from the T_m's of various bilayer-forming lipids **(Table 2)**.

Increasing the aliphatic chain length would elevate the T_m, while higher degree of unsaturation

results in a lower T_m. The hydrophilic head group can also change T_m by as much as 20K (e.g.

comparing DPPE and DPPC).

Table 2 Names and transition temperatures of related lipid species

Lipid species	Name	Acyl chain	Transition temperature (T_m/°C) *
PC	POPC	C16:0/C18:1	-2
	DLPC	C12:0/C12:0	-1
	DMPC	C14:0/C14:0	24
	DPPC	C16:0/C16:0	41
	DSPC	C18:0/C18:0	55
	d_{62}-DPPC	C16:0/C16:0	37
PA	DMPA	C14:0/C14:0	50
	DPPA	C16:0/C16:0	67
PI	DPPI	C16:0/C16:0	41
PS	DPPS	C16:0/C16:0	54
PE	DPPE	C16:0/C16:0	62
DG	DPG	C16:0/C16:0	66

* Transition temperature data is adapted from references (*12*, *13*). Melting point is used instead of transition temperature for DG. PC: phosphatidylcholine; PA: phosphatidic acid; PI: phosphatidylinositol; PS: phosphatidylserine; PE: phosphatidylethanolamine; DG: diacylglycerol.

3.3 Cholesterol promotes L_o phase formation

As one major component of biological membrane, cholesterol is the most important regulator of

membrane phase behavior. Thermodynamic studies reveal that cholesterol eliminates the main

phase transition, making a smooth transition through T_m (*12*). This can be explained by the rigidity of cholesterol's ring structure that limits the motion of the acyl chains and thus breaks up the long-range cooperativity in between them. Consequently, cholesterol exerts different effects when it is mixed with saturated lipids or unsaturated lipids. For saturated lipids that normally form S_o, cholesterol frees up individual molecule from interaction with its neighbors, and increases lateral movement approaching that in L_d phase. For unsaturated lipids that normally form L_d, cholesterol restricts the conformational flexibility in the acyl chains, and confines the volume taken up by each lipid. Hence cholesterol increases the packing order in unsaturated lipid bilayer like in the S_o phase. The overall effect of cholesterol is to eliminate the difference between L_d and S_o phase, and gives rise to a third phase, the L_o phase.

3.4 Lateral phase separation in lipid bilayer

Nano-scale lateral heterogeneity in bilayer was recognized when the 'fluid mosaic' model was presented (*1*). In the same year, lateral phase separation in phospholipid membrane was observed and proposed to facilitate membrane trafficking (*14*). The term 'lateral' refers to two-dimensional behavior, since in most processes concerning lipid phase behavior, the hydrophobic hydrocarbon-water interaction dominates over all the other interaction energies.

Lateral phase separation can occur when different lipids are mixed. Micro- or nano- domains will form, driven by immiscibility between different phases. Phase separation of lipid mixtures can be

quantitatively described in terms of temperature or chemical composition. Analogous to the main

phase transition of a single species, lipid mixture also transits from one-phase regime to phase

coexistence when it is cooled through its miscibility transition temperature (T_c) (*15*). At T_c, the

energy cost to exchange matter between different components is essentially zero. The system

then displays critical behavior, where fluctuations in domain size and composition occur. This is

believed to have important implication in the behavior of cell plasma membrane. More

commonly, phase behavior of a mixture is described with respect to varying chemical

composition. This is more relevant to biological membranes that are usually kept under

physiological temperature. Observations in ternary mixtures composed by a low-T_m lipid, a high-

T_m lipid, and cholesterol can be summarized into phase diagram (*6, 9, 15*). A simplified diagram

is shown below **(Figure 3.2)**. Any point in the triangle diagram represents a specific composition

and it falls into a certain phase regime that is delineated by a line defining the phase boundary.

The location of these lines is determined by the combination of lipid molecules in the mixture.
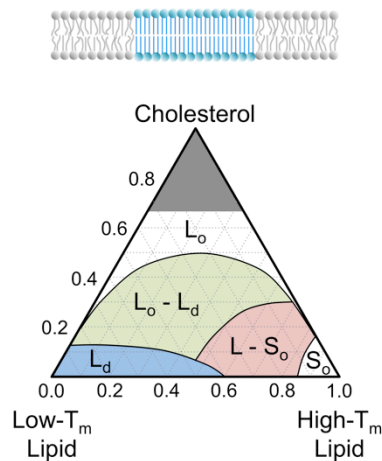
Figure 3.2 Lateral phase separation and sketch of phase diagram. Lipids with distinct property will segregate into domains. A simplified phase diagram is shown for a bio-mimicking ternary-component model membrane, based on experimental measurement from reference (*16*). Solid lines indicate phase boundaries. Area above 66% cholesterol exceeds its solubility in lipid bilayer thus not considered here.

3.5 Biological membranes

Knowledge gained from model membrane study provides valuable insight into the organization principle of biological membrane. Chemical compositions obtained from 'lipidomics' of sub-cellular compartments can be readily fitted into the phase diagram so that equilibrium property of the membrane can be inferred. For example, the endoplasmic reticulum (ER) has low cholesterol concentration and low lipid saturation, which predicts L_d-like properties (*3, 17, 18*). In comparison, the plasma membrane is enriched with cholesterol and saturated lipids, which predicts L_d-L_o phase coexistence. Experimentally the liquid phase separation is readily observed in giant vesicles budded from plasma membrane (GPMV) (*5*).

However, biological membranes are fundamentally different from *in vitro* model systems. This has been realized after decades of efforts searching for 'lipid raft' in live cell. The lipid raft hypothesis was raised to account for lateral heterogeneity and assembly of a 'signaling platform' in plasma membrane (*2, 19*). Though lipid raft has found its physical ground as L_o phase, its existence in cell membrane remains a debate. Unlike GPMV (model for plasma membrane) where micro-scale phase separation can be readily observed by optical microscopy, the raft domain is believed to be much smaller (nanoscale size) and much more dynamic (*5*). The

puzzling behavior in live cell invokes researches into the unique properties of biological membrane (*7*, *8*).

Many factors have been proposed that distinguish biological membranes from *in vitro* model membranes (*5*, *7*). One important factor is attributed to the crowding membrane proteins, whose transmembrane domain perturbs putative lipid domain boundary, while interaction with the cytoskeleton adds diffusion barriers to the membrane lipids. The other important factor relates to the non-equilibrium nature of biological membrane. The living cell is an intrinsically non-equilibrium system that constantly undergoes lipid turnover and membrane trafficking. This is especially relevant and important for endoplasmic reticulum (ER), the largest membrane system as well as the lipid metabolic center in cell. Thus in the next chapter, I will show new evidence obtained by metabolic imaging that proves the susceptibility of ER membrane phase to the modulation of lipid metabolic activity.

3.6 References

1. S. Singer, G. L. G. L. Nicolson, The fluid mosaic model of the structure of cell membranes. *Science*. **175**, 720–731 (1972).

2. K. Simons, G. Van Meer, Lipid sorting in epithelial cells. *Biochemistry*. **27**, 6197–6202 (1988).

3. G. van Meer, D. R. Voelker, G. W. Feigenson, Membrane lipids: where they are and how they behave. *Nat. Rev. Mol. Cell Biol.* **9**, 112–24 (2008).

4. D. Lingwood, K. Simons, Lipid rafts as a membrane-organizing principle. *Science*. **327**, 46–50 (2010).

5. K. Simons, J. L. Sampaio, Membrane organization and lipid rafts. *Cold Spring Harb Perspect Biol*. **3**, a004697 (2011).

6. F. A. Heberle, G. W. Feigenson, Phase Separation in Lipid Membranes. *Cold Spring Harb Perspect Biol*, 1–13 (2011).

7. K. Jacobson, O. G. Mouritsen, R. G. W. Anderson, Lipid rafts: at a crossroad between cell biology and physics. *Nat. Cell Biol.* **9**, 7–14 (2007).

8. E. L. Elson, E. Fried, J. E. Dolbow, G. M. Genin, Phase separation in biological membranes: integration of theory and experiment. *Annu. Rev. Biophys.* **39**, 207–226 (2010).

9. D. Marsh, Cholesterol-induced fluid membrane domains: A compendium of lipid-raft ternary phase diagrams. *Biochim. Biophys. Acta - Biomembr.* **1788**, 2114–2123 (2009).

10. R. Phillips, T. Ursell, P. Wiggins, P. Sens, Emerging roles for lipids in shaping membrane-protein function. *Nature*. **459**, 379–85 (2009).

11. J. F. Nagle, Theory of the Main Lipid Bilayer Phase Transition. *Annu. Rev. Phys. Chem.* **31**, 157–196 (1980).

12. P. R. Cullis, D. B. Fenske, M. J. Hope, in *Biochemistry of Lipids, Lipoproteins and Membranes* (ELSEVIER, ed. 5, 2008), pp. 1–37.

13. N. Kučerka, M.-P. Nieh, J. Katsaras, Fluid phase lipid areas and bilayer thicknesses of commonly used phosphatidylcholines as a function of temperature. *Biochim. Biophys. Acta - Biomembr.* **1808**, 2761–2771 (2011).

14. E. J. Shimshick, H. M. McConnell, Lateral phase separation in phospholipid membranes. *Biochemistry*. **12**, 2351–2360 (1973).

15. S. L. Veatch, S. L. Keller, Separation of liquid phases in giant vesicles of ternary mixtures of phospholipids and cholesterol. *Biophys. J.* **85**, 3074–3083 (2003).

16. R. F. M. de Almeida, A. Fedorov, M. Prieto, Sphingomyelin/ phosphatidylcholine/

cholesterol phase diagram: boundaries and composition of lipid rafts. *Biophys. J.* **85**, 2406–16 (2003).

17. F. R. Maxfield, I. Tabas, Role of cholesterol and lipid organization in disease. *Nature.* **438**, 612–621 (2005).

18. R. Volmer, D. Ron, Lipid-dependent regulation of the unfolded protein response. *Curr. Opin. Cell Biol.* **33**, 67–73 (2015).

19. K. Simons, E. Ikonen, Functional rafts in cell membranes. *Nature.* **387**, 569–572 (1997).

Chapter 4

Metabolic activity induces membrane phase separation in endoplasmic reticulum

4.1 Abstract

Membrane phase behavior has been well characterized in model membranes in vitro under thermodynamic equilibrium state. However, the widely observed differences between biological membranes and their in vitro counterparts are placing more emphasis on non-equilibrium factors, including influx and efflux of lipid molecules. The endoplasmic reticulum (ER) is the largest cellular membrane system and also the most metabolically active organelle responsible for lipid synthesis. Yet how the non-equilibrium metabolic activity modulates ER membrane phase has not been investigated. Here, we studied the phase behavior of functional ER in the context of lipid metabolism. Utilizing advanced vibrational imaging technique, i.e. stimulated Raman scattering microscopy, we discovered that metabolism of palmitate, a prevalent saturated fatty acid (SFA), could drive solid-like domain separation from the presumably uniformly fluidic ER membrane, a previously unknown phenomenon. The potential of various fatty acids to induce solid phase can be predicted by the transition temperatures of their major metabolites. Interplay between saturated and unsaturated fatty acids is also observed. Hence, our study sheds light on cellular membrane biophysics by underscoring the non-equilibrium metabolic status of living cell.

4.2 Introduction

Lipid bilayers enclose the boundary of life, and their diverse chemical compositions together with physical phases underlie membrane organizations and biological functions (*1*). Studies of *in*

vitro model membranes have shown that depending on chemical composition, mixture of lipids in a bilayer could either blend into a uniform phase, or phase-separate into co-existing domains due to immiscibility. Three major phases have been observed in these studies: liquid disordered (L_d), liquid ordered (L_o), and solid ordered (S_o), each representing a distinct type of bilayer organization (*1*, *2*).

However, biological membranes are fundamentally different from *in vitro* model systems. As a manifestation, liquid phase separation gives rise to static microdomains that can be readily observed in model membrane, yet the existence of raft domains (L_o - like) in live cell has been a debate for decades due to much smaller domain size and faster dynamics (*3*). Many factors have been proposed to account for the unique aspects of biological membranes. One important factor is attributed to lipid-protein interaction, including the crowding effect of membrane protein as well as the intimate regulation by cytoskeleton (*3*, *4*). Another less-considered but more fundamental factor concerns the thermodynamic state of the membrane. The living cell is an intrinsically non-equilibrium system that constantly undergoes lipid turnover and membrane trafficking. This is especially relevant and important for endoplasmic reticulum (ER), the largest membrane system as well as the lipid metabolic center in cell. Indeed, ER is subject to the influx of lipid molecules synthesized from fatty acids, the efflux due to vesicle budding and secretion, and the exchange of lipids with other organelles via extensive and dynamic physical contacts (*1*). All the above contribute to fast turnover of ER lipids (half life ~ 100h or one cell division) (*5*, *6*).

With rich metabolic activity, ER membrane is easily perturbed from equilibrium by dynamic influx of nutrients. We hence hypothesize that the non-equilibrium factor, such as lipid synthesis in ER, is capable of driving ER membrane from its poised L_d phase to phase separation. Our hypothesis is motivated by recent studies and findings. Experimentally, fatty acids such as palmitate have been reported to promote saturated lipid synthesis and accumulation in ER, which subsequently impair ER structural integrity (*7–9*). But the ER phase behavior was not examined there. Theoretical study has also alluded to local phase separation when patches of membrane with different composition are delivered to a bilayer (*10*). This could be relevant to the condition of active lipid synthesis occurring in ER.

Towards testing this hypothesis, our study creates a non-equilibrium condition with the presence of lipid synthesis in ER membrane of living cells. To examine the spatial heterogeneity of membrane and interrogate its biophysical status, we employed the emerging vibrational imaging technique, i.e. stimulated Raman scattering microscopy, and correlated it with lipidomics and fluorescence imaging. We found that ER membrane phase is susceptible to the modulation by metabolic activity. Remarkably, lipid synthesis derived from palmitate, a prevalent saturated fatty acid (SFA), even drives formation of solid-like domains, which are rarely reported in live cells that presumably require fluidic membrane (*4, 11–14*). Interestingly, the propensity of phase separation can be tuned by the molecular identity of the metabolic flux: the ability of various fatty acids to induce solid-like domains is correlated with the transition temperatures of their

major metabolites, and might be related with their cytotoxicity. Our study surveys the ER phase behavior in the thermodynamic space of external perturbation, and provides new insight into membrane phase behavior of living cells far away from equilibrium.

4.3 Results

4.3.1   Palmitate promotes membrane lipid synthesis

ER hosts the majority of de novo lipid synthesis in the cell (*1*). In this way, ER is able to build new membrane components from external nutrients such as fatty acids, and supply the renewal of other membrane-bound organelles. In fact, it has been reported that palmitate, the most abundant fatty acid in circulation (*15*), promotes phospholipid synthesis and accumulation in ER (*7–9*). To understand how palmitate metabolism reshapes the cellular lipidome and what types of lipid metabolites are accumulating, we analyzed changes in cellular lipid composition over time by HPLC-MS **(Figure 4.1)**.

The time-dependent lipid heatmap **(Figure 4.1 A)** reveals significant fold increase in glycerolipids (DG, TG, and phospholipids) and ceramide (Cer) ($p < 0.05$). This confirms that exogenous fatty acid promotes *de novo* lipid synthesis. Interestingly, when quantified by the change in absolute amount, several particular lipids show up in the highest rank of increase or decrease **(Figure 4.1 B)**. Besides TG, a common storage lipid, the major lipid accumulation is attributed to DG, PA, PI, and PC with two saturated fatty acyl chains (most likely 16:0 or 18:0).

Meanwhile, there is a slight decrease in CE and PC lipids with unsaturated acyl chains. In summary, palmitate caused time-dependent accumulation of fully saturated glycerolipids that elevated the overall lipid saturation in the cells.
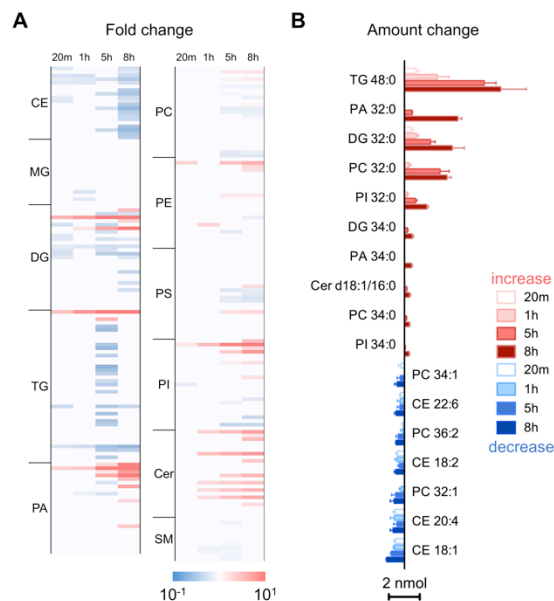
Figure 4.1 Palmitate promotes synthesis and accumulation of saturated lipids. (A) Alteration in major lipids after treatment by palmitate for 20min, 1h, 5h, and 8h. Fold change (p<0.05, student's t-test) was calculated and shown in the heatmap. CE: cholesterol ester; MG: monoacylglyceride; DG: diacylglyceride; TG: triacylglyceride; PA: phosphatidic acid; PC: phosphatidylcholine; PE: phosphatidylethanolamine; PS: phosphatidylserine; PI: phosphatidylinositol; Cer: ceramide; SM: sphingomyeline. **(B)** Alteration in amount was calculated as the amount difference between palmitate treated and control. Diagram shows top ranks in increase or decrease. Data are presented as mean ± SEM.

4.3.2   Vibrational imaging reveals dynamic structures derived from lipid synthesis

To examine the spatial heterogeneity of these newly synthesized lipids, we then sought to visualize their distribution and organization as well as relation to ER in cells. Towards this, we

employed the emerging vibrational imaging technique for stable-isotope-labeled small molecules (*16*). Specifically, deuterium labeling of small molecules creates carbon-deuterium bond (C-D) whose vibration provides distinct chemical contrast for stimulated Raman scattering (SRS) microscopy **(Figure 4.2 A)**. This platform is well-suited for studying lipid metabolism as well as membrane biophysics (*16–19*), since tagging small lipid molecules with relatively bulky fluorophores often significantly perturbs lipid metabolism (*20*) (will also be shown later in our study). Indeed, most common fluorescent tags such as NBD and BODIPY were termed 'ill-suited' when used to study lipid biophysics (*20, 21*).

We treated cells with deuterium-labeled palmitate (d-palmitate) for several hours before acquiring C-D SRS images. We found that palmitate-derived lipids possessing the C-D label formed isolated micron-sized patches **(Figure 4.2 B)**. We then correlated the C-D SRS image with confocal fluorescence from a luminal ER marker transiently expressed in the same cell (ER-GFP). In this way, we confirmed that these new structures colocalized with ER **(Figure 4.2 B)**, consistent with ER accumulation of palmitate-derived lipids mentioned earlier (*7*). Similar distribution pattern was reproduced in many other cell types, including HepG2 liver cell and mouse fibroblast **(Figure 4.2 C and D)**, suggesting a common underlying mechanism.
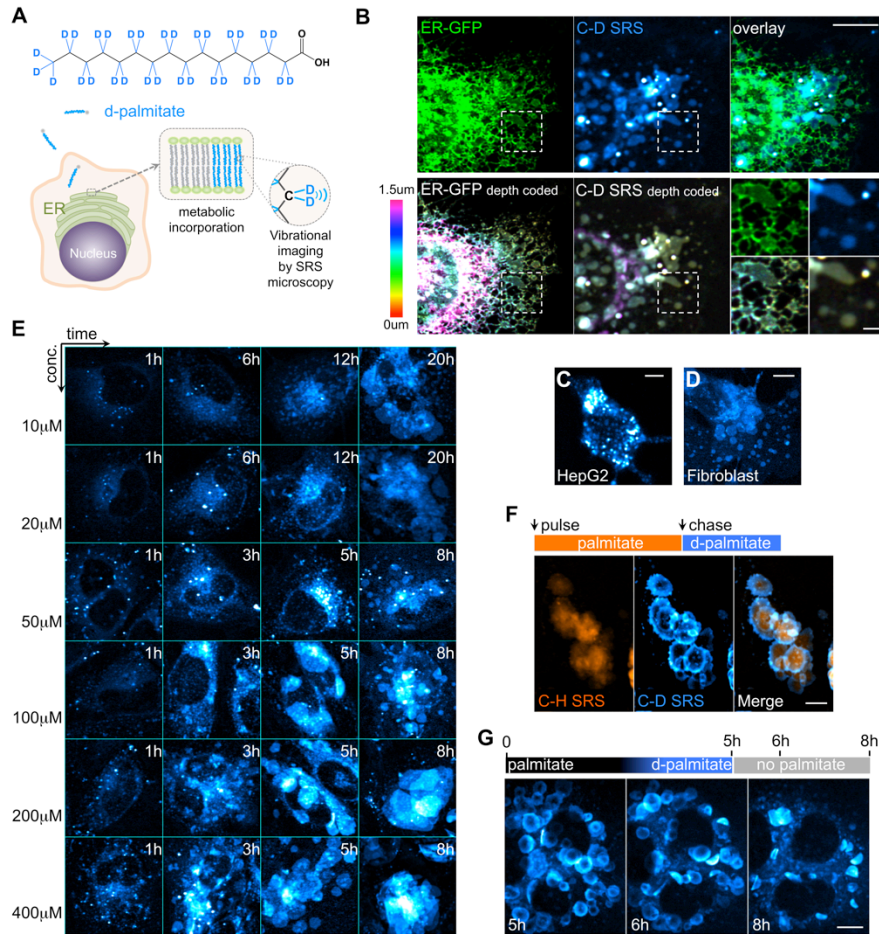
Figure 4.2 Vibrational imaging reveals new dynamic structures formed by palmitate metabolites. (A) Illustration of isotope-SRS imaging: Deuterium-labeled palmitate (d-palmitate) is metabolically incorporated into cellular lipids. The C-D bond vibration of the resulting metabolites is specifically detected by SRS microscopy. 400μM fatty acid was used in this study if not specified. **(B)** ER-GFP expressing HeLa cell was treated by 400μM d-palmtiate for 4 hrs. Upper row shows 2-D projection of ER-GFP fluorescence, C-D SRS, and their overlay. Bottom row shows depth-color-coded image of ER-GFP and C-D SRS, and the magnified view of boxed regions. **(C and D)** C-D SRS images of HepG2 liver cell (C) and mouse fibroblast (D) treated with palmitate for 5 hrs. **(E)** C-D SRS images of HeLa cells treated with palmitate at varying dose (10 ~ 400μM) and time (1 ~20h). **(F)** HeLa cells were pulse-chase treated with 4hr palmitate and 2hr d-palmitate, fixed and washed by 0.5% Triton X-100. Two color images are shown for C-H and C-D channels. **(G)** The clearance of palmitate-derived compartments after removal of palmitate. HeLa cells were pulse-chase treated by 4hr palmitate and 1hr d-palmtiate to better delineate the compartments. Then palmitate was removed and C-D SRS image were taken at indicated time. Scale bars: 10μm.

Next we studied the dynamics including both the growth and turnover of these structures. We supplemented HeLa cells with palmitate concentration varying from 10μM to 400μM for duration from 1hr to 20hrs **(Figure 4.2 E)**. This is in reference to the free fatty acid concentration in circulation (fluctuating in a wide range from sub- to several milli molar) (*22*) and that commonly applied in other studies (e.g. 400μM (*8*, *23–25*)). We found that the new structures grew over time, faster at higher concentration **(Figure 4.2 E)**. It appeared as isolated puncta in early stages and gradually developed into large lamellar structure. The development over time well correlates with the accumulation of palmitate metabolites revealed by lipidomics. Notably, these structures exist in a wide range of time and dose conditions we have used: at concentration down to 10μM, or after as short as 1h treatment **(Figure 4.3 A)**. To resolve the growth dynamics in single cells, we performed a sequential treatment first by palmitate followed by d-palmitate. The later-applied label appeared on the rim, which suggests that the development of the structure is driven by accumulation of new palmitate metabolites at the periphery **(Figure 4.2 F)**. These compartments disappeared gradually following removal of palmitate from the media, indicating that their development relies on the sustained influx of fatty acid **(Figure 4.2 G)**. All the above dynamic features suggest that these palmitate-derived structures were driven by cellular metabolic activity.

We furthur verified the above conclusion based on the following additional lines of evidence. Firstly, although palmitate is reported to be toxic at high dose (*26*), no observable cell death

occurred under the time and dose condition we used for imaging **(Figure 4.3 B)**, which indicates

that the cells are metabolically active. Secondly, quantification of intracellular free fatty acid

(FFA) reveals a transient rise and then recovery to baseline level within 3hrs **(Figure 4.3 C)**.

Thus FFA alone is not sufficient to form such stable structures over a long time. Lastly, these

structures were abolished by small-molecule inhibitor of acyl-CoA synthetase that catalyzes the

first step in lipid synthesis (*27*) **(Figure 4.3 D and E)**, and were also suppressed by siRNA of

GPAT4, an enzyme involved in phospholipid synthesis (*28*) **(Figure 4.3 F and G)**.
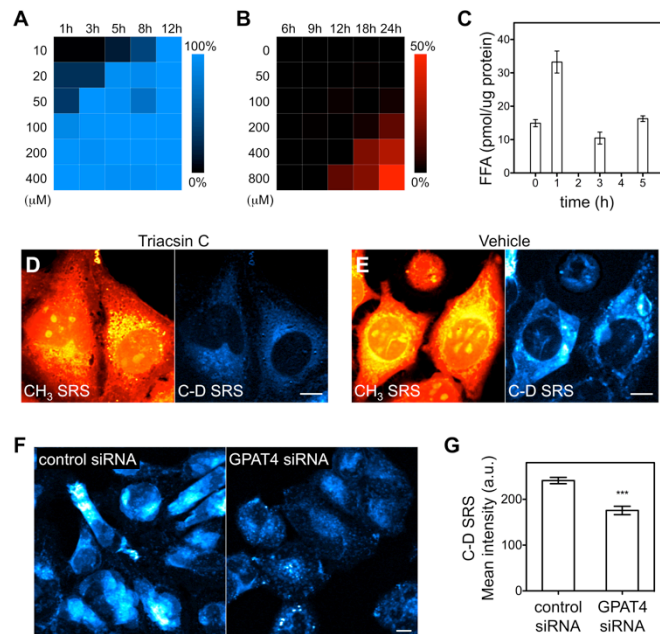
Figure 4.3 Palmitate-derived structure is a result of lipid synthesis. (A) Percentage of cells with observable

palmitate-derived non-LD structure. **(B)** Time- and dose- dependent decrease in cell number. **(C)** FFA concentration

measured in HeLa cells after treatment by palmitate for 0, 1, 3, and 5 hrs. Data are presented as mean ± SEM. n=4.

(D and **E)** HeLa cells were treated with d-palmitate for 5 hrs in the presence of 5μM Triacsin C (D) or vehicle

(DMSO) (E). CH₃ SRS shows total protein distribution as morphology of the cell. **(F)** HeLa cells transfected with

control siRNA or GPAT4 siRNA for 48hrs, and treated with d-palmitate for 6 hrs. Representative C-D SRS images are shown. **(G)** Mean C-D SRS intensity is quantified for each condition. $p < 0.001$, $n = 4$, total cell number >100. Scale bars: $10\mu m$.

4.3.3   Newly synthesized lipids form phase-separated membrane domains in ER

Given the observed dynamic accumulation of palmitate metabolites in ER, we asked if ER membrane phase had been affected. To test this, we first examined if the new structures are organized as membrane, and then evaluated if they are phase-separated domains from the fluidic ER.

We confirmed that they were not lipid droplets (LDs) where neutral lipid metabolites (TAG and CE) are stored. At early stage (1h incubation) when the structures are small, they can be readily distinguished from LDs via neutral lipid staining by Nile Red **(Figure 4.4 A)**. Quantitative image analysis of the Nile-Red-positive and -negative structures reveals significant difference between LDs and the non-LD signal. LDs can be easily distinguished in the image as small intense puncta. Yet the non-LD structures exhibit wider distribution in size but weaker and more uniform intensity than LDs **(Figure 4.4 B and C)**, suggesting a lamellar organization. Indeed, morphologically, reconstructed z-stack images revealed planar structures spanning several microns in x-y but with diffraction-limited z-profiles **(Figure 4.4 D)**. This fits into the model where planar membrane bilayer lies parallel to the illumination plane **(Figure 4.4 E)**. In cells

where individual compartments are no longer resolvable from each other, we could always find

step-like features in the line profile of C-D SRS intensity **(Figure 4.4F)**. We could then identify

an equal spacing after calculating pairwise intensity difference **(Figure 4.4 G)** (14±5 uV in HeLa

and 19±6 uV in COS-7). As an orders-of-magnitude estimation, this intensity spacing translates

into 3.1×10^6 palmitoyl groups in focus, which approximates to the SRS signal size calculated

from one deuterated lipid bilayer, suggesting the compositional unit to be lipid bilayer **(see 4.5**

Supplementary Information). Thus in parallel with lipidomic analysis that the accumulating

lipids (DG, PA, PI, and PC) are all membrane constituents **(Figure 4.1)**, these pieces of evidence

from imaging strongly support that palmitate-derived lipids are forming membrane.
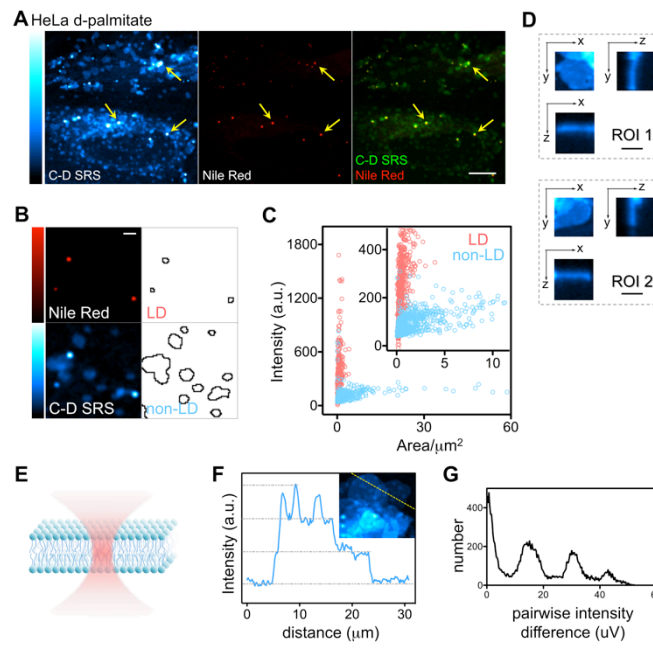
Figure 4.4 Image quantification and analysis reveals membrane features of palmitate-derived structure. (A)
C-D SRS, Nile Red fluorescence and overlay images of HeLa cell treated with d-palmitate for 1 hr and stained by
Nile Red. Arrows indicate LDs stained by Nile Red. **(B)** Representative images showing image segmentation based

on Nile Red positive (LD) or Nile Red negative (non-LD). **(C)** C-D SRS intensity quantification and area measurement from LD and non-LD signal based on segmentation in (B). **(D)** HeLa cell was treated with d-palmitate for 5hrs. Orthogonal views of two regions of interest (ROI) from depth-resolved reconstructed image are shown for individual structures. **(E)** Cartoon showing the focused light illumination on the single bilayer. **(F)** Line profiles of C-D SRS image with overlapping layers of palmitate metabolites. **(G)** Pairwise distribution function was calculated for these line profiles, which show oscillating patterns that indicate constant intensity spacing. Scale bars: 10μm in (A); 2μm in (B) and (D).

In fact, forming domains instead of blending into existing ER membrane already implies different organization in palmitate-derived lipids from the native ER membrane. We then further examined the spatial relation of these membrane domains to ER membrane using two types of membrane markers, one lipid (BODIPY-C_{12}) and one membrane protein (mCherry-sec61β). BODIPY-C_{12} is a common fluorescent analog of palmitate **(Figure 4.5 A)**, and also serves as a general membrane marker. Thus we add trace BODIPY-C_{12} along with d-palmitate. Remarkably, different patterns were observed in the correlative SRS and fluorescence images **(Figure 4.5 B)**. While C-D SRS exhibited many isolated domains, BODIPY-C_{12} highlighted reticular structure resembling the ER. Even negative correlation can be observed between BODIPY fluorescence and C-D SRS channel in flat regions of ER membrane such as large sheet and nuclear envelope **(Figure 4.5 C, Figure 4.6 A-C)**. This observation, on one hand, could be reconciled by strong perturbation from the BODIPY tag. On the other hand, it supported the hypothesized lateral phase separation in ER membrane, since bulky fluorescent probes usually favor partitioning into disordered over ordered phase *in vitro* (*20*).
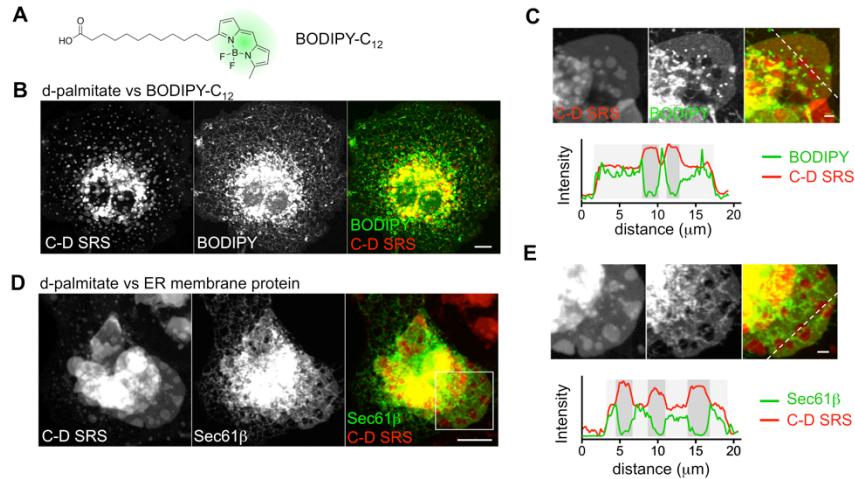
Figure 4.5 Fluorescent membrane markers reveal lateral separation of palmitate-derived membrane domains in ER. (A) Chemical structure of fluorescent analog, BODIPY-C$_{12}$. **(B)** COS-7 cell was treated with d-palmitate and 2μM BODIPY-C$_{12}$ for 5 hrs. C-D SRS, BODIPY fluorescence, and their overlay are shown. **(C)** Magnified view is shown for a large sheet. Intensity profiles of the dashed line are shown for both SRS (red) and fluorescence (green) channels. **(D)** mCherry-Sec61β-expressing COS-7 cell was treated with d-palmitate for 4 hrs. C-D SRS, Sec61β fluorescence, and their overlay are shown. **(E)** Magnified view is shown for the boxed area in (D). Intensity profiles of both SRS (red) and fluorescence (green) channels are shown for the dashed line in (D). In (C) and (E), dark grey stripes indicate two layers of palmitate-derived membrane. Scale bars: 10μm in (B) and (D); 2μm in (C) and (E).

This result of lateral phase separation can be further verified with an ER membrane protein marker, mCherry-Sec61β **(Figure 4.5 D)**. Specifically, on large sheets, negative correlation can be clearly identified between C-D SRS and mCherry fluorescence channels **(Figure 4.6 E)**. Special considerations must be taken when examining the lateral heterogeneity in ER membrane. Different from plasma membrane or vesicle, ER has unique architecture composed by tubular and lamellar cisternae. We noted that the planar structure of C-D SRS domains fits into the model of so-called 'ER sheet' (lamellar cisternae), where a lamellar space is enclosed by two

opposing membrane bilayers. Palmitate metabolites may constitute either or both of the bilayers **(Figure 4.6 D)**. This is manifested in the line profiles of C-D SRS that negatively correlates with fluorescence channel **(Figure 4.5 C and E, Figure 4.6 C)**. With one layer of palmitate-derived membrane, fluorescent markers still reside in the opposite bilayer of the cisternae; yet when both layers are occupied by palmitate metabolites, fluorescence is almost non-detectable.
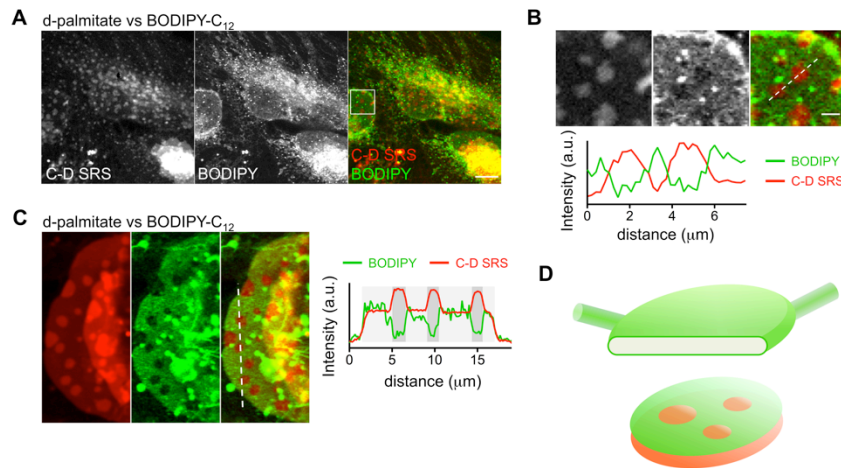
Figure 4.6 Fluorescent membrane markers reveal lateral separation of palmitate-derived membrane domains in ER (supplementary). (A) HeLa cell was treated with d-palmitate and 1μM BODIPY-C$_{12}$ for 1 hrs. C-D SRS, BODIPY fluorescence, and their overlay are shown. **(B)** Magnified view is shown for the boxed area in (A). Intensity profiles of the dashed line are shown below for both SRS (red) and fluorescence (green) channels. **(C)** Similar to **Figure 4.5 E**. **(D)** Tubular and lamellar structures of ER cisternae (upper) and the proposed model for lateral phase separation in ER (bottom). Palmitate-derived membrane is shown in red while the rest of ER membrane is shown in green. Scale bars: 10μm in (A); 2μm in (B) and (C).

4.3.4   Emergence of solid-like domain in ER membrane

Unlike plasma membrane (~ 50% cholesterol), ER membrane is characterized by low cholesterol

level (3-6% of lipids (*29*)). This predicts unique phase behavior in ER membrane, because

cholesterol is known to eliminate solid-liquid transition and promote L_o phase formation in *in*

vitro model membrane (*30*). Accordingly, ER membrane in its normal state is believed to adopt

uniform L_d phase due to low lipid saturation (*1*, *14*, *31*), but meanwhile is potentiated for L-S_o

phase separation if saturation level elevates sufficiently **(Figure 4.7)**. Since lipid synthesis

following palmitate supplementation introduces into ER new membrane components that are

overall more saturated, we hypothesized that such influx was able to drive solid-like domain

separation from the otherwise L_d-like ER. Solid phase is characterized by highly ordered acyl

chain packing, as well as ultraslow lateral motion **(Figure 4.7)**. Thus to test our hypothesis, we

first evaluated the conformational order and then estimated the translational mobility of lipids

within these domains.
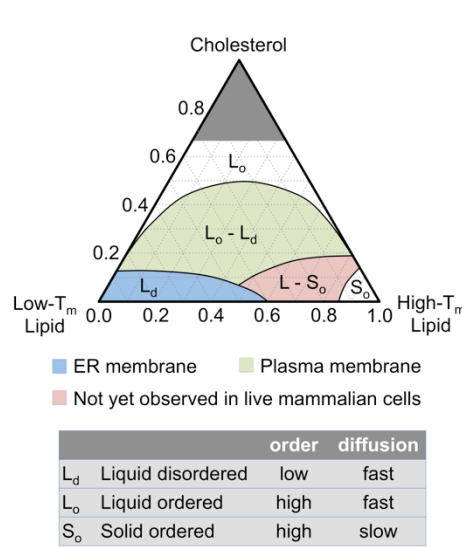
Figure 4.7 Sketch of phase diagram of bio-mimicking ternary-component model membrane. Solid lines

indicate phase boundaries defined by composition of each component in the mixture at a given temperature such as

37°C. Phase regions are colored to show the current understanding of biological membrane phase and do not

necessarily represent the exact composition. Area above 66% cholesterol exceeds its solubility in lipid bilayer thus not considered here. Based on experimental results from reference (*2*).

In Raman spectroscopy, the acyl chain conformational order could be inferred from the Raman peak width of CD_2 symmetric stretch vibration at 2101 cm^{-1}: the more ordered, the narrower the peak (*32*). The Raman spectra measured from d-palmitate-treated cells **(Figure 4.8 A,** cell**)** resembled that from d_{62}-DPPC in the ordered (presumably S_o) phase **(Figure 4.8 A,** d_{62}-DPPC 25°C**)**, but displayed pronouncedly narrower peaks than d_{62}-DPPC or d_{31}-POPC in L_d phase **(Figure 4.8 A,** d_{62}-DPPC 42°C and d_{31}-POPC 25°C**)**. To offer more spatial information, we performed ratiometric SRS imaging between 2101 and 2168 cm^{-1} to map the conformational order of intracellular palmitate metabolites. Consistently, with reasonable heterogeneity, the membrane domains display high 2101/2168 cm^{-1} ratio close to the ordered phase **(Figure 4.8 B)**. Hence, *in situ* Raman microspectroscopy and SRS spectral imaging unraveled a marked increase in acyl chain conformational order on the palmitate derived membrane domains.
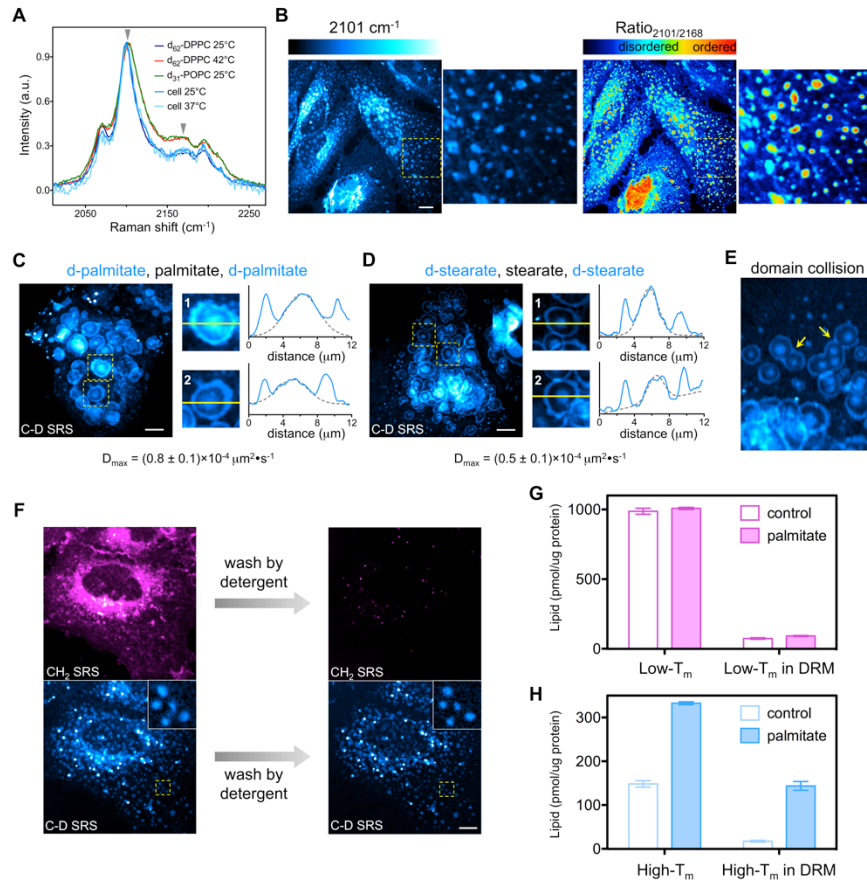
Figure 4.8 Palmitate-derived membrane domains exhibit solid-like properties as high conformational order and low translational mobility. (A) Normalized Raman spectra of d_{62}-DPPC dispersion (at 25°C and 42°C) and d_{31}-POPC dispersion (at 25°C) overlaid with Raman spectra of HeLa cells treated with d-palmitate for 5 hrs (acquired at 25°C and 37°C). Arrowheads mark peak ($2101cm^{-1}$) and shoulder ($2168cm^{-1}$) frequencies used for spectral imaging in (B). **(B)** C-D SRS images acquired at $2101cm^{-1}$ and $2168cm^{-1}$ and the calculated ratiometric images for HeLa cells treated with d-palmitate for 3hrs. Magnified images are shown on the right. **(C)** C-D SRS images of HeLa cell sequentially treated with d-palmitate (3 hrs), palmitate (1.5 hrs) and d-palmitate (0.5 hrs). Intensity profiles (blue) were measured across the yellow lines in ROIs and fitted with Gaussian function (gray dashed). The estimated maximum diffusion coefficient (D_{max}) is shown below (mean ± SEM, n = 13). **(D)** Similar to the sequential treatment in (C), d-stearate (1 hr), stearate (1.5 hrs) and d-stearate (0.5 hr) was used instead on palmitate. The estimated maximum diffusion coefficient (D_{max}) is shown below (mean ± SEM, n = 21). **(E)** Domain collision (arrows) captured in cells treated as in (C). **(F)** HeLa cell was treated with d-palmitate for 1 hr. CH_2 and

C-D SRS images were taken before (left column) and after (right column) being washed by 0.5% Triton X-100 for 10 min at 4°C. **(G and H)** Changes in low-T_m (G) and high-T_m (H) lipid concentration in total lipid extract or detergent-resistant lipid fraction (DRM) after palmitate treatment for 5 hrs. Major species DG, PA, PI, PC, PE, PS are included in quantification. Data are presented as mean ± SD. Scale bars: 10μm.

We then sought to evaluate the translational mobility within the phase-separated domains. Since fluorescent probes failed to incorporate into these domains **(Figure 4.5)**, we relied on pulse-chase SRS imaging to estimate the lateral diffusion coefficient (D). We sequentially treated the cells with d-palmitate, then regular palmitate, and finally d-palmitate again, and observed a bull-eye-like pattern in the C-D SRS channel **(Figure 4.8 C)**. Similar bull-eye pattern was observed for a longer-chain SFA, stearic acid **(Figure 4.8 D)**. By semi-quantitative estimation, if these domains were in the liquid phase, one would predict homogeneous C-D signal distribution within individual domains (2D free diffusion displacement d = 5~10 μm) due to fast lateral diffusion ($D(L_d) \sim 1$ μm^2/s, $D(L_o) \sim 10^{-1}$ μm^2/s) (*1, 33*). Quantitatively, fitting of the line profiles to two-dimentional diffusion (the intensity (I) distribution along radius (r) after diffusion time t: $I(r,t) \propto e^{-\frac{r^2}{4Dt}}$) yielded an estimated D about 10^{-4} μm^2/s, which is close to that in S_o phase ($D(S_o) \sim 10^{-3}$ μm^2/s (*1, 33*)). Moreover, collision between separate domains was also captured **(Figure 4.8 E)**. Interestingly, the collided domains neither completely fuse nor recover the circular morphology in nearly half an hour, again suggesting that they are in solid phase wherein intra-domain interaction overcomes line tension. To the best of our knowledge, this is the first time that large-scale solid-phase membrane is reported in living mammalian cells.

4.3.5   High-T_m palmitate metabolites provide driving force for phase separation

To gain insight into the molecular driving force underlying solid-like domain, we evaluated the phase transition temperature (T_m) of accumulated lipids highlighted in lipidomics **(Figure 4.1 B)**. We noted that those 32:0 and 34:0 lipids all bear significantly higher T_m $(T_m = 41°C\sim67°C,$ **Table 2)** than physiological temperature, which could account for the driving force of L-S_o phase separation under the low cholesterol presented in ER **(Figure 4.7)**.

To further test if high-T_m lipids are indeed enriched in phase-separated membrane domains, we performed detergent wash by Triton X-100 following palmitate treatment. Resistance to nonionic detergent such as Triton X-100 at 4°C is a classical assay used to identify the existence of potentially ordered membrane domain (*4*). SRS imaging revealed that C-D domains but not the majority of endogenous CH_2-bearing lipids showed resistance to detergent wash **(Figure 4.8 F)**. We then did parallel lipidomic analysis on control or palmitate-treated cells before and after detergent wash. We divided the major lipid species (DG, PA, PI and PC) into high-T_m ($T_m >$ 37°C) and low-T_m ($T_m < 37°C$) categories and quantified each category in total lipid extract or detergent-resistant fraction **(Figure 4.8 G and H)**. Firstly, the result shows that new lipid synthesis is dedicated to high-T_m lipids but not low-T_m lipids, thus increase in high-T_m lipids is well correlated with appearance of C-D SRS signal. Secondly, the increased portion of high-T_m lipids is mostly retained after detergent wash while low-T_m lipids are not. This further pinpointed the direct involvement of high-T_m lipids in the formation of detergent-resistant C-D SRS

domains. Similar detergent-resistant membrane pattern was also observed following treatment of

regular palmitate, which rules out the possible isotope effect **(Figure 4.9 A and B)**.
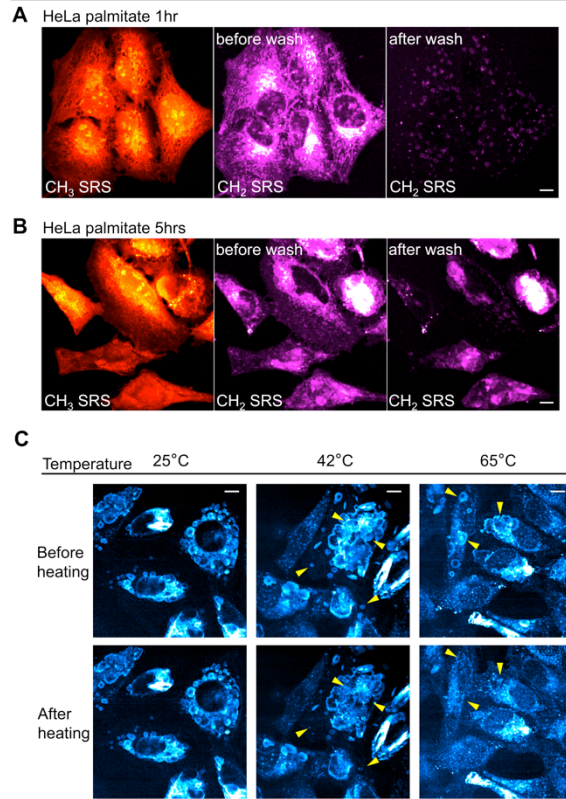
Figure 4.9 Palmitate-derived solid-like membranes are characterized by Triton resistance and high-T_m

components. (A and **B)** HeLa cells were treated with 400μM palmitate for 1 hr (A) or 5 hrs (B). Protein CH_3 and

lipid CH_2 SRS signal were taken before and after extraction by 0.5% Triton X-100 for 10 min at 4°C. Significant

amount of lipid showed detergent-resistance. **(C)** HeLa cells were sequentially treated with 400μM palmitate for 5

hrs and then d-palmitate for 1 hr to delineate individual membrane domains. They were then fixed in

paraformaldehyde at room temperature, and incubated in water bath at indicated temperature (25°C, 42°C, and 65°C)

for 10 min. C-D SRS images were taken before and after the 10 min incubation. Arrows indicate membrane domains

that disappeared (melted) after heating. Scale Bars: 10μm.

As an independent validation, the T_m of membrane domains could also be estimated by *in situ*

heating of fixed cells **(Figure 4.9 C)**. After 10-min temperature-controlled incubation, domains

remained intact in C-D SRS image under 25°C, but partially deformed under 42°C and were mostly melted (deformed) under 65°C, which matches with the T_m's of major palmitate metabolites $(T_m = 41°C \sim 67°C)$. Therefore, the lipidomic and imaging analysis together demonstrate the preferred localization of high-T_m lipids within solid-like membrane domains, supporting high-T_m metabolites were indeed the molecular driving force for such phase separation.

4.3.6 ER membrane phase separation can be tuned by fatty acid unsaturation and chain length

Based on the hypothesized connection between high-T_m lipids and membrane domain formation, ER phase separation should be dependent on the molecular identity of the fatty acid and can be predicted by the T_m of the its main lipid metabolites. Thus we similarly applied a common UFA, oleate, whose metabolites (e.g. DOPC) possess very low T_m due to the unsaturation in the acyl chain (Table 2). The colocalization of C-D SRS to Nile Red fluorescence reveals that oleate is incorporated almost exclusively into LDs, and did not form membrane domains (Figure 4.10 A).

We went on to test a set of deuterated SFAs including lauric acid (C12:0), myristic acid (C14:0), palmitic acid (C16:0), stearic acid (C18:0). Their metabolites show elevating T_m's due to increasing fatty acyl chain lengths (Table 2). In agreement with our hypothesis, they exhibited increasing capability to drive large-scale phase separation at the same concentration (Figure 4.10 B): C12:0 does not form visible membrane domains but numerous LDs even after prolonged

treatment; C14:0 only forms domains with limited size (~1 micron); C18:0 forms large-scale membrane structures even faster than C16:0 does.
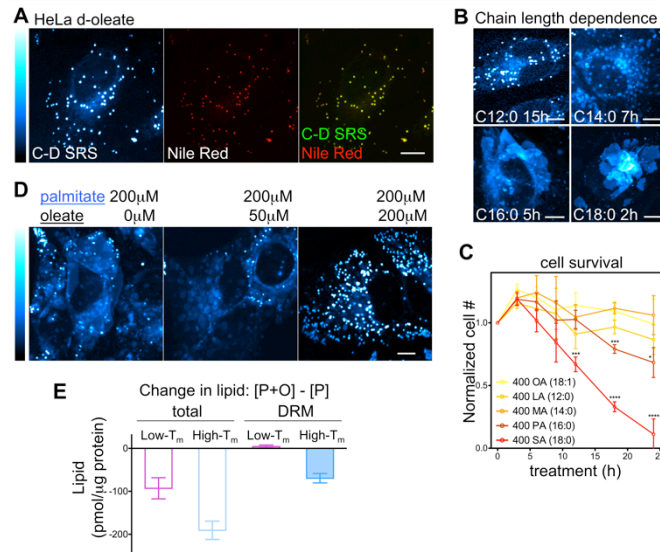
Figure 4.10 The tendency to form solid-like membrane can be tuned by fatty acid identity and combination.

(A) C-D SRS, Nile Red fluorescence and overlay images of HeLa cell treated with d-oleate for 1 hr and stained by Nile Red. **(B)** C-D SRS images of HeLa cells treated with C12:0 (15 hrs), C14:0 (7 hrs), C16:0 (5 hrs) and C18:0 (2 hrs). **(C)** Normalized cell number after treatment of designated fatty acid and duration. Data are presented as mean ± SEM. n=4. *, $p < 0.05$; ***, $p < 0.005$; ***, $p < 0.001$. **(D)** C-D SRS images of HeLa cells treated with combination of d-palmitate and increasing concentrations of oleate. **(E)** Changes in low-T_m and high-T_m lipid concentration in cells co-treated by 400μM palmitate and 200μM oleate (P+O) compared to 400μM palmitate alone (P). Data are presented as the amount difference between 'P+O' and 'P' ([P+O]-[P]) in total lipid extract (total) and detergent-resistant fraction (DRM). Scale bars: 10μm.

Notably, in the functional sense, we found similar dependence for fatty-acid-induced cell death **(Figure 4.10 C)**. Cell death was observed only after prolonged incubation with the long-chain

SFA C16:0 and C18:0, but not with UFA or shorter-chain SFA. This dependence is also correlated with stress markers reported elsewhere that are mutually independent, including Akt/protein kinase B (Akt/PKB) signaling, activation of Jun N-terminal kinase (JNK) and the unfolded protein response (UPR) (*25*, *34*, *35*). Thus, the metabolic effect of a fatty acid might be predicted by simple physicochemical principle regarding the T_m of its metabolites.

4.3.7   Interplay between fatty acids in modulating ER membrane phase separation

Since the plasma consists of a complex and fluctuating mixture of SFA and UFA (*15*), this further raises an interesting question whether fatty acids could influence each other in the metabolic modulation of ER phase. Noticing the relatively low T_m of POPC, we hypothesized that oleate might prevent the system from being driven by palmitate to phase separation.

Thus we added oleate together with d-palmitate to study its influence on the phase separation potential of the latter **(Figure 4.10 D)**. Biochemical studies have found that oleate can channel palmitate into LDs (*23*), which is also manifested in C-D SRS images from our experiment. Yet more importantly, oleate also diminished the solid-like domains in a concentration-dependent manner. Note that in this context, oleate itself stays excluded from the remaining solid-phase membrane **(Figure 4.11 A and B)**. Similar to oleate, docosahexaenoic acid (DHA, 22:6), a polyunsaturated fatty acid (PUFA), was also able to reduce the area of palmitate-derived solid membrane domains **(Figure 4.11 C)**.
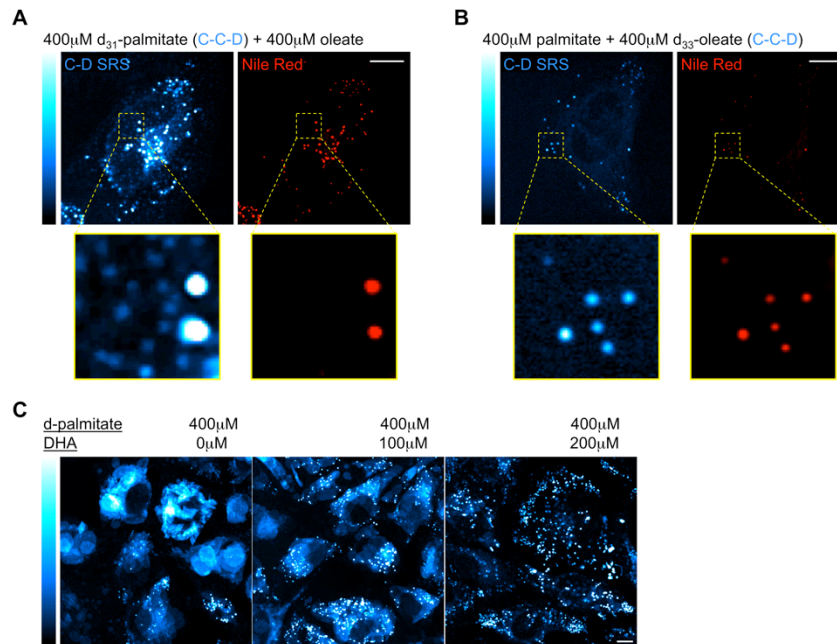
Figure 4.11 Unsaturated fatty acids are able to tune the formation of solid-like domains. (A and **B)** HeLa cells were treated with 400μM palmitate and 400μM oleate for 2 hrs, with isotope labeling on palmitate (A) or oleate (B), and then stained by Nile Red for LDs. (A) and (B) were adjusted to same contrast for visualizing non-LD compartment, thus LDs appear saturated in intensity in (B). **(C)** C-D SRS images of HeLa cells treated with combination of d-palmitate and increasing concentrations of DHA. Scale bars: 10μm.

In parallel, we compared the lipid profile after co-treatment of oleate to that only treated by palmitate. Both total lipid extract and detergent-resistant fraction show significant alteration by oleate. The effect of oleate is clearly reflected in the level of low-T_m and high-T_m lipids **(Figure 4.10 E)**. In total lipid extract, oleate reduced more high-T_m lipids than low-T_m lipids. In detergent-resistant fraction, which is more specific to the solid-like membrane, oleate also significantly reduced high-T_m lipids but did not affect low-T_m lipids. Therefore, in supplementation to the current understanding that accumulation of neutral lipids is cytoprotective,

a previously unknown mechanism for UFA to rescue the cytotoxicity of SFA might lie in its ability to destruct the solid-like membrane.

4.4 Discussion

By taking advantage of live-cell SRS microscopy coupled with minimally perturbative isotope labeling, we discovered that the influx of high-T_m lipids caused by SFA metabolism could drive the formation of large-scale membrane domains in ER. Remarkably, the newly formed domains exhibited solid-like characteristics as detergent resistance, high conformational order, ultraslow lateral diffusion, strong intra-domain interaction and large-scale structural stability. Our observation thus reveals the susceptibility of ER membrane phase to the metabolic activity, and, to some extent, corroborates the theoretical prediction under non-equilibrium condition (*10*). Here we want to emphasize that the earlier work by Fan *et al.* focused on L_o - L_d phase separation to account for lipid raft on plasma membrane, and the non-equilibrium condition there largely refers to vesicle delivery. Although the biological manifestations are different here for ER with all the unique characteristics such as low cholesterol level and high *de novo* lipid synthesis activity, the conclusion drawn from our study converges to a similar physical principle.

In retrospect, ER membrane phase separation has escaped previous observations possibly due to three reasons. Firstly, decades of membrane biophysical studies in live cells have been primarily focused on plasma membrane, largely driven by the controversial lipid raft hypothesis. It is

estimated that cholesterol make up 50% of plasma membrane lipid (*1*). As shown by the phase diagram, high cholesterol concentration tends to result in L_o and L_d phases instead of solid phase. The cholesterol-poor ER membrane would exhibit very different biophysics from the plasma membrane. Secondly, it has to be observed under non-equilibrium condition, where metabolic activity in the ER perturbs the membrane far enough from equilibrium. Lastly, the solid-phase membrane is difficult to capture by other experimental means. Common fluorescent lipid probes suffer from poor ER delivery and/or low partitioning into potentially ordered phase (*20*). For example, we showed that bulky-labeled BODIPY-C_{12} could not partition in solid domain **(Figure 4.5)**. For the same reason, such phase separation could elude the examination of membrane fluidity using fluorescent FA analogs (*24*), which only report on the liquid phase in ER membrane.

4.6 Estimation of d-palmitoyl (d_{31}-labeled) number from C-D SRS intensity

To estimate number of d_{31}-palmitoyl group, we first obtained a calibration curve of d_{31}-palmitic acid **(Figure 4.12)**.
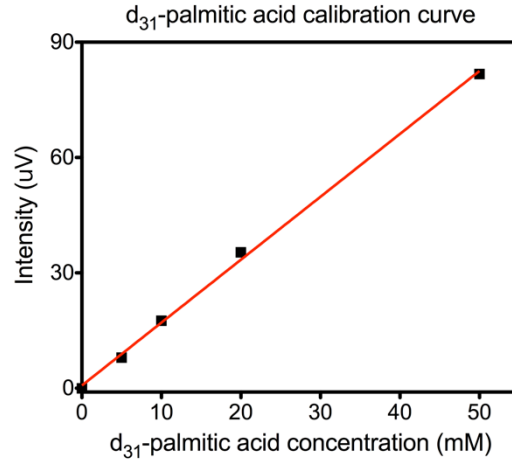
Figure 4.12 Calibration curve of d$_{31}$-palmitic acid. C-D SRS intensity was measured for d$_{31}$-palmitic acid solution

in DMSO of varying concentration. Linear fitting of the concentration curve yielded a slope of 1.64uV/mM.

The average intensity spacing calculated for HeLa cell is 15uV. This corresponds to number of

d$_{31}$-palmitoyl groups ($N_{d\text{-}palmitoyl}$) as calculated below:

$$N_{d-palmitoyl} = \frac{\text{stepsize}}{\text{slope}} \cdot \text{focal volume} \cdot N_A$$

$$= \frac{15uV}{1.64uV/mM} \cdot \pi \cdot (300nm)^2 \cdot 2\mu m \cdot 6.02 \times 10^{23} = 3.1 \times 10^6$$

where N_A is the Avogadro constant, and focal volume is approximated by a cylinder whose

radius and height are 300nm and 2μm, respectively.

The number of palmitoyl groups in a DPPC bilayer within focal area ($N_{palmitoyl,\ DPPC}$) can also be

estimated. The area per DPPC molecule occupies is estimated to be 50Å^2 (*36*). Thus

$$N_{palmitoyl,\ DPPC} = \frac{\text{focal area}}{\text{area per molecule}} \cdot 2 \text{ layers} \cdot 2 \text{ palmitoyl per molecule}$$

$$= \frac{\pi \cdot (300nm)^2}{50\text{Å}^2} \cdot 2 \cdot 2 = 2.3 \times 10^6$$

Thus, $N_{d\text{-}palmitoyl}$ calculated from image intensity is very close to $N_{palmitoyl, DPPC}$, which suggests that the structures in SRS C-D channel are composed of layered membrane.

4.7 Materials and Methods

Fatty acid solution

Palmitic acid (16:0), stearic acid (18:0), oleic acid (18:1), palmitic acid-d_{31} (98% D), stearic acid-d_{35} (98%D) and oleic acid-d_{34} (98% D) were from Sigma. Lauric acid-d_{23} (98% D) (12:0) and myristic acid-d_{27} (98% D) (14:0) were from Cambridge Isotope Laboratory. Fatty acids were reacted with sodium hydroxide (Sigma) above melting point to form 20mM solution, and then coupled to fatty-acid-free bovine serum albumin (BSA) (Sigma) in about 2:1 molar ratio to make 2mM stock solution in culture medium. They were then added to cell culture to achieve designated concentration. For extremely low concentration (10μM and 20μM), serum was reduced from 10% to 1% to minimize interference from serum fatty acid. Control cells were treated with only BSA of same concentration.

Cell culture

The following cell lines and their culture media were used in this study: HeLa (ATCC) and COS-7 (ATCC), Dulbecco's Modified Eagle Medium (DMEM, Invitrogen 11965-092); HepG2 (ATCC), Eagle's Minimum Essential Medium (EMEM, ATCC 30-2003). All media were supplemented with 10% fetal bovine serum (Invitrogen, 16000-044) and 100 U/mL

penicillin-streptomycin (Invitrogen, 15140-122). Primary neonatal heart fibroblasts were isolated from Day 3 newborn mice using Pierce™ Primary Cardiomyocyte Isolation Kit (Thermo Fisher Scientific) with slight modification as following: after cell mixture was plated, fibroblasts attached to glass and other cells were removed. Triacsin C (Sigma), as an inhibitor of acyl-CoA synthetase, was made into 25mM stock solution in DMSO. Scrambled siRNA (4390843, ThermoFisher) or GPAT4 siRNA (s44067, ThermoFisher) was transfected by Lipofectamine RNAiMax (ThermoFisher) according to the manufacturer's procedure.

Cells that reached 80% confluence were dissociated and plated onto coverslips (No.1, FisherBrand) for most experiments and glass-bottom petri-dish (MATTEK, P35G-1.5-14-C) for experiments with single cell tracking. The coverslip was stuck to a microscope slide (1mm thick, VWR) using 0.1mm imaging spacer (SecureSeal) to make an imaging chamber filled with phosphate buffered saline.

Stimulated Raman Scattering Microscopy

The setup for SRS microscopy was similar to what was described earlier (*37*). Briefly, two spatially and temporally overlapped picosecond pulsed laser beams (Pump and Stokes) were produced by picoEmerald laser system (Applied Physics and Electronics) and directed into a laser-scanning microscope (FV1200MPE; Olympus) through a 60× objective (water immersion, N.A. = 1.2, UPlanAPO/IR; Olympus). The Stokes beam was modulated by electro-optic

modulator at 8MHz to enable detection of stimulated Raman loss in pump photon after light interaction with chemical bond vibration. Transmitted Pump and Stokes beams were collected by a high N.A. condenser (oil immersion, 1.4 N.A.; Olympus), filtered by a bandpass filter (890/220 CARS; Chroma Technology) and projected onto a 10×10 mm^2 Si photodiode (FDS1010; Thorlabs) biased at 64V to measure only the Pump beam intensity. The output current is terminated by a 50Ω terminator, pre-filtered at 8-MHz ($\pm$1MHz, KR 2724; KR electronics), and then demodulated by a lock-in amplifier (SR844; Stanford Research Systems). The in-phase X output was used to generate SRS image at the speed of 100ms/pixel. Laser powers on sample were measured to be up to 120mW (Stokes) and 100mW (Pump). The wavelength of Stokes laser was 1064 nm and wavelengths for Pump laser used in this study were: 810.5 nm (2940 cm^{-1}, mainly protein CH$_3$), 816.7 nm (2845 cm^{-1}, mainly lipid CH$_2$), 869.0 nm (2101 cm^{-1}, C-D on resonance), 885.0 nm (off-resonance background). Images were acquired by Fluoview Software and were later assigned pseudo colors in ImageJ.

Fluorescence imaging

BODIPY$^{®}$ 500/510 C$_1$, C$_{12}$ (BODIPY-C$_{12}$) (Molecular Probes) (diluted from 10mM stock solution in DMSO) was used as a fluorescent fatty acid tracer at 2μM in the culture medium. Neutral lipid was stained with 1mM Nile Red solution (diluted from 1mM stock in DMSO) (Molecular Probes) before cells were fixed by 4% PFA. ER is visualized in live COS-7 cells using CellLight® ER-GFP (Thermo Fisher Scientific) according to the manufacturer's manual.

mCherry-Sec61β was a gift from Gia Voeltz (Addgene plasmid # 49155). Transient transfection was done in confluent HeLa cells with Lipofectamine® 3000 Reagent (Thermo Fisher Scientific) at 200ng DNA per well in a 24-well plate. 5 to 10 hours after transfection, cells were split and re-plated to adjust cell density and images were taken 48 hours after transfection.

Confocal fluorescence imaging was performed on the same microscope used for SRS imaging (FV1200MPE; Olympus) and the same objective (60×, water immersion, N.A. = 1.2, UPlanAPO/IR; Olympus). For BODIPY-C$_{12}$, Nile Red, and ER-GFP, the excitation wavelength and filter selection were 488nm and 505-605nm. For mCherry, the excitation wavelength and filter selection were 543nm and 560-660nm.As SRS and fluorescence measurements used different lasers and dichroic mirrors, image was slightly shifted from one to the other channel. In order to perform multi-channel co-localization, we used a standard grid to determine the offset between the field of views of SRS and fluorescence and corrected it in all the multi-channel images later. Images were acquired by Fluoview Software and pseudo-colored by ImageJ.

Spontaneous Raman Spectroscopy

Spontaneous Raman spectra were acquired using an upright confocal Raman spectrometer (Xplora; HORIBA Jobin Yvon), with temperature controlled by water bath (±1°C). Samples were illuminated by 532 nm (25 mW) laser through a 100× objective (air, N.A.=0.9, MPlan N; Olympus). Reference lipids including DPPC-d$_{62}$ and POPC-d$_{31}$ (deuteration on palmitoyl chain,

Avanti Polar Lipids) were first dissolved in 1:2 chloroform:methanol to make 50mM solution. The solvent was then evaporated in Argon gas flow, and lipids were reconstituted in PBS to 50mM after repeated sonication until a dispersion of multilamellar vesicles was formed. Cell spectra were obtained from cells fixed with 4% PFA, lipid droplets were avoided judging by bright field view. Glass and solution background was subtracted by measuring non-cell signal near the targeted cell. For each condition, three different regions on the sample were randomly selected and their spectra were averaged. The acquisition time was 20s for reference lipids and 400s for cells.

CH$_2$ CH$_3$ unmixing algorithm

In order to separate total lipid and protein signal from their overlapping spectrum, we adapted a previously reported spectral unmixing algorithm (*38*). Briefly, we acquired the SRS signals from two wavelengths bearing features of lipid and protein, respectively, and the amount of the two species can be determined by a linear combination of the signal at those two wavelengths (See below), with coefficients R$_1$ and R$_2$ pre-determined by pure substances. Here, signals at 2845 cm^{-1} and 2940 cm^{-1} were measured to perform the spectral unmixing:

lipid [CH$_2$] = R$_1$ • [2845] – R$_2$ • [2940]

protein [CH$_3$] = [2940] – [2845]

where R$_1$ = 5; R$_2$ = 0.4.

Note that this spectral unmixing is rather an estimation of total lipid content than a precise

separation of chemical species.

Image segmentation for LD and membrane signal

Image segmentation in correlative Nile Red fluorescence and C-D SRS image sets **(Figure 4.4 B and C)** was performed in ImageJ. Cells with isolated C-D SRS domains were selected. LDs were first segmented using an intensity threshold in Nile Red fluorescence image. The LD pixels were then left out in C-D SRS image. Resulting C-D SRS image were segmented using intensity threshold and reasonable circularity range.

Cell viability assay

Cells were plated in 96-well plate, after designated treatment concentration and time, cell number is quantified using CellTiter-Glo® Luminescent Cell Viability Assay (Promega) following the manufacturer's instruction.

Free fatty acid quantification

Cells were plated in 6-well plate, after treatment with palmitate, intracellular free fatty acid is quantified by fluorometry using Free Fatty Acid Quantification Kit (Sigma) following the manufacturer's instruction. Protein concentrations were also quantified from each sample as normalization (see below).

Determination of protein concentration using BCA assay

Protein concentration was determined in order to quantify lipid composition in cell. Cells cultured in 6-well plate were washed with ice-cold PBS for three times. They were then lysed in 100μL RIPA buffer on ice for 2 min before being scraped to collection tube. Cell lysates were centrifuged at 1000g for 5min to remove cell debris. Protein concentration in the obtained supernatant was measured using Pierce protein BCA assay kit (Thermo Fisher) following the manufacturer's instruction.

Analysis of lipids using high performance liquid chromatography - mass spectrometry

Lipid extracts were prepared using a modified Bligh and Dyer procedure as described previously (*39*, *40*), spiked with appropriate internal standards, and analyzed using a 6490 Triple Quadrupole LC/MS system (Agilent Technologies, Santa Clara, CA). Glycerophospholipids and sphingolipids were separated with normal-phase HPLC as described before (*40*), with a few modifications. An Agilent Zorbax Rx-Sil column (inner diameter 2.1×100 mm) was used under the following conditions: mobile phase A (chloroform:methanol:1 M ammonium hydroxide, 89.9:10:0.1, v/v) and mobile phase B (chloroform:methanol:water:ammonium hydroxide, 55:39.9:5:0.1, v/v); 95% A for 2 min, linear gradient to 30% A over 18 min and held for 3 min, and linear gradient to 95% A over 2 min and held for 6 min. Sterols and glycerolipids were separated with reverse-phase HPLC using an isocratic mobile phase as before (*40*) except with an Agilent Zorbax Eclipse XDB-C18 column (4.6 × 100 mm). Quantification of lipid species

was accomplished using multiple reaction monitoring (MRM) transitions that were developed in earlier studies (*40*) in conjunction with referencing of appropriate internal standards: PA 14:0/14:0, PC 14:0/14:0, PE 14:0/14:0, PI 12:0/13:0, PS 14:0/14:0, SM d18:1/12:0, D_7-cholesterol, CE 17:0, MG 17:0, 4ME 16:0 diether DG, D_5-TG 16:0/18:0/16:0 (Avanti Polar Lipids, Alabaster, AL).

4.8 References

1. G. van Meer, D. R. Voelker, G. W. Feigenson, Membrane lipids: where they are and how they behave. *Nat. Rev. Mol. Cell Biol.* **9**, 112–24 (2008).

2. R. F. M. de Almeida, A. Fedorov, M. Prieto, Sphingomyelin/ phosphatidylcholine/ cholesterol phase diagram: boundaries and composition of lipid rafts. *Biophys. J.* **85**, 2406–16 (2003).

3. K. Simons, J. L. Sampaio, Membrane organization and lipid rafts. *Cold Spring Harb Perspect Biol.* **3**, a004697 (2011).

4. K. Jacobson, O. G. Mouritsen, R. G. W. Anderson, Lipid rafts: at a crossroad between cell biology and physics. *Nat. Cell Biol.* **9**, 7–14 (2007).

5. T. Omura, P. Siekevitz, G. E. Palade, Turnover of constituents of the endoplasmic reticulum membranes of rat hepatocytes. *J. Biol. Chem.*, 2389–2396 (1967).

6. E. Dawidowicz, Dynamics of membrane lipid metabolism and turnover. *Annu. Rev. Biochem.* **56**, 43–61 (1987).

7. N. M. Borradaile *et al.*, Disruption of endoplasmic reticulum structure and integrity in lipotoxic cell death. *J. Lipid Res.* **47**, 2726–37 (2006).

8. A. K. Leamy *et al.*, Enhanced synthesis of saturated phospholipids is associated with ER stress and lipotoxicity in palmitate treated hepatic cells. *J. Lipid Res.* **55**, 1478–1488 (2014).

9. M. M. Robblee *et al.*, Saturated fatty acids engage an IRE1α-dependent pathway to activate the NLRP3 inflammasome in myeloid cells. *Cell Rep.* **14**, 2611–2623 (2016).

10. J. Fan, M. Sammalkorpi, M. Haataja, Influence of nonequilibrium lipid transport, membrane compartmentalization, and membrane proteins on the lateral organization of the plasma membrane. *Phys. Rev. E - Stat. Nonlinear, Soft Matter Phys.* **81**, 1–15 (2010).

11. D. Lingwood, K. Simons, Lipid rafts as a membrane-organizing principle. *Science.* **327**, 46–50 (2010).

12. J. C. M. Holthuis, A. K. Menon, Lipid landscapes and pipelines in membrane homeostasis. *Nature.* **510**, 48–57 (2014).

13. C. Eggeling *et al.*, Direct observation of the nanoscale dynamics of membrane lipids in a living cell. *Nature.* **457**, 1159–62 (2009).

14. F. R. Maxfield, I. Tabas, Role of cholesterol and lipid organization in disease. *Nature.* **438**, 612–621 (2005).

15. O. Quehenberger *et al.*, Lipidomics reveals a remarkable diversity of lipids in human plasma. *J. Lipid Res.* **51**, 3299–305 (2010).

16. L. Wei *et al.*, Live-cell bioorthogonal chemical imaging: stimulated Raman scattering microscopy of vibrational probes. *Acc. Chem. Res.* **49**, 1494–1502 (2016).

17. L. Li, H. Wang, J.-X. Cheng, Quantitative coherent anti-Stokes Raman scattering imaging of lipid distribution in coexisting domains. *Biophys. J.* **89**, 3480–3490 (2005).

18. D. Fu *et al.*, In vivo metabolic fingerprinting of neutral lipids with hyperspectral stimulated Raman scattering microscopy. *J. Am. Chem. Soc.* **136**, 8820–8 (2014).

19. A. Alfonso-García, S. G. Pfisterer, H. Riezman, E. Ikonen, E. O. Potma, D38-cholesterol as a Raman active probe for imaging intracellular cholesterol storage. *J. Biomed. Opt.* **21**, 61003 (2016).

20. A. S. Klymchenko, R. Kreder, Fluorescent probes for lipid rafts: from model membranes to living cells. *Chem. Biol.* **21**, 97–113 (2014).

21. L. Kuerschner *et al.*, Polyene-lipids: a new tool to image lipids. *Nat. Methods*. **2**, 39–45 (2005).

22. F. Karpe, J. R. Dickmann, K. N. Frayn, Fatty acids, obesity, and insulin resistance: time for a reevaluation. *Diabetes*. **60**, 2441–9 (2011).

23. L. L. Listenberger *et al.*, Triglyceride accumulation protects against fatty acid-induced lipotoxicity. *Proc. Natl. Acad. Sci. U. S. A.* **100**, 3077–82 (2003).

24. M. B. Hoppa *et al.*, Chronic palmitate exposure inhibits insulin secretion by dissociation of Ca2+ channels from secretory granules. *Cell Metab.* **10**, 455–465 (2009).

25. R. G. Holzer *et al.*, Saturated fatty acids induce c-Src clustering within membrane subdomains, leading to JNK activation. *Cell*. **147**, 173–184 (2011).

26. R. Volmer, K. van der Ploeg, D. Ron, Membrane lipid saturation activates endoplasmic reticulum unfolded protein response transducers through their transmembrane domains. *Proc. Natl. Acad. Sci. U. S. A.* **110**, 4628–33 (2013).

27. R. A. Igal, P. Wang, R. A. Coleman, Triacsin C blocks de novo synthesis of glycerolipids and cholesterol esters but not recycling of fatty acid into phospholipid: evidence for functionally separate pools of acyl-CoA. *Biochem. J.* **324 (Pt 2**, 529–34 (1997).

28. H. Shindou, T. Shimizu, Acyl-CoA:lysophospholipid acyltransferases. *J. Biol. Chem.* **284**, 1–5 (2009).

29. A. Radhakrishnan, J. L. Goldstein, J. G. McDonald, M. S. Brown, Switch-like control of SREBP-2 transport triggered by small changes in ER cholesterol: a delicate balance. *Cell Metab.* **8**, 512–21 (2008).

30. F. A. Heberle, G. W. Feigenson, Phase Separation in Lipid Membranes. *Cold Spring Harb Perspect Biol*, 1–13 (2011).

31. R. Volmer, D. Ron, Lipid-dependent regulation of the unfolded protein response. *Curr. Opin. Cell Biol.* **33**, 67–73 (2015).

32. B. P. Gaber, P. Yager, W. L. Peticolas, Deuterated phospholipids as nonperturbing

components for Raman studies of biomembranes. *Biophys. J.* **22**, 191–207 (1978).

33. J. Korlach, P. Schwille, W. W. Webb, G. W. Feigenson, Characterization of lipid bilayer phases by confocal microscopy and fluorescence correlation spectroscopy. *Proc. Natl. Acad. Sci.* **96**, 8461–8466 (1999).

34. P. P. H. Hommelberg, J. Plat, R. C. J. Langen, A. M. W. J. Schols, R. P. Mensink, Fatty acid-induced NF-κB activation and insulin resistance in skeletal muscle are chain length dependent. *Am. J. Physiol. Endocrinol. Metab.* **296**, E114-20 (2009).

35. J. A. Chavez, S. A. Summers, Characterizing the effects of saturated fatty acids on insulin signaling and ceramide and diacylglycerol accumulation in 3T3-L1 adipocytes and C2C12 myotubes. *Arch. Biochem. Biophys.* **419**, 101–9 (2003).

36. N. Kučerka, M.-P. Nieh, J. Katsaras, Fluid phase lipid areas and bilayer thicknesses of commonly used phosphatidylcholines as a function of temperature. *Biochim. Biophys. Acta - Biomembr.* **1808**, 2761–2771 (2011).

37. L. Wei *et al.*, Live-cell imaging of alkyne-tagged small biomolecules by stimulated Raman scattering. *Nat. Methods*. **11**, 410–2 (2014).

38. Z. Yu *et al.*, Label-free chemical imaging in vivo: three-dimensional non-invasive microscopic observation of amphioxus notochord through stimulated Raman scattering (SRS). *Chem. Sci.* **3**, 2646 (2012).

39. E. G. Bligh, W. J. Dyer, A rapid method of total lipid extraction and purification. *Can. J. Biochem. Physiol.* **37**, 911–917 (1959).

40. R. B. Chan *et al.*, Comparative lipidomic analysis of mouse and human brain with Alzheimer disease. *J. Biol. Chem.* **287**, 2678–88 (2012).

Chapter 5

Lipotoxicity and current understanding of its molecular mechanism

5.1 Lipotoxicity in metabolic disorder and *in vitro* model

Elevated free fatty acid (FFA) in circulation is frequently associated with metabolic disorders such as diet-induced obesity and type 2 diabetes (T2D) (*1–3*). The concentration of plasma nonesterified fatty acid (NEFA) dynamically fluctuates in a wide range from 0.1 ~ 2mM in nondiabetic individuals, depending on fasting/feeding state and insulin level (*4*). In diabetic and obese individuals, this value is even higher (several millimolar) due to insulin resistance and retarded plasma NEFA removal (*3*).

It was first discovered by Dr. Roger Unger that elevated FFA correlated with lipid accumulation and function impairment in the pancreas, which he later termed 'lipotoxicity' (*5*). Since then, the adverse effects of excess FFA have been widely observed, linking aberrant lipid metabolism to the pathogenesis of metabolic stress (*5–11*). Consequently, FFA treatment of cultured cells has become a popular *in vitro* model for lipotoxicity, which isolates lipid from a myriad of concomitant metabolic stressors encountered *in vivo*. For example in tissue-specific context, FFA has been reported to cause β cell apoptosis and impair insulin secretion in pancreatic islet (*12–16*), to metabolically activate inflammation in adipose tissue (*17–21*), to diminish insulin sensitivity in skeletal muscle (*22–24*), and to contribute to non-alcoholic liver steatosis (*25–30*). Furthermore, the lipotoxic effect of FFA is not limited to cells and organs that are frequently challenged by metabolic stress, but has also been reported in a much wider spectrum of cell types, suggesting its general inducement of cell dysfunction and death (*21, 31–36*).

Among all the FAs, it is widely acknowledged that saturated fatty acids (SFAs) exhibit much more prominent lipotoxic effect than unsaturated fatty acids (UFAs) (*12, 24, 29, 37–41*). Indeed, most studies above use palmitate (C16:0), an SFA and also one of the most abundant plasma fatty acids (~30% FFAs) (*42*), at submillimolar concentration to study the action of excess FFAs both *in vitro* and *in vivo*. UFAs such as oleate (C18:1), however, do not elicit the lipotoxicity as palmitate, and often reverse the adverse effects of palmitate for reasons that are not fully understood yet (*23, 29, 38, 43, 44*).

5.2 Proposed mechanisms of lipotoxicity

Here I review several proposed molecular mechanisms for lipotoxicity, with an emphasis on the primary subcellular locations where stress response is initiated or executed **(Figure 5.1)**. More comprehensive reviews can be found for specialized topics (*8, 9, 26, 45–47*). It should be recognized that fatty acid invokes an intricate metabolic network concerning organelles such as endoplasmic reticulum (ER) and mitochondria, thus the eventual cell death is an integrated outcome. As will be shown below, for example, disturbance in Ca^{2+} homeostasis impairs the functions of multiple organelles; on the other hand several pathways eventually converge on Jun N-terminal Kinase (JNK) pro-apoptotic pathway.
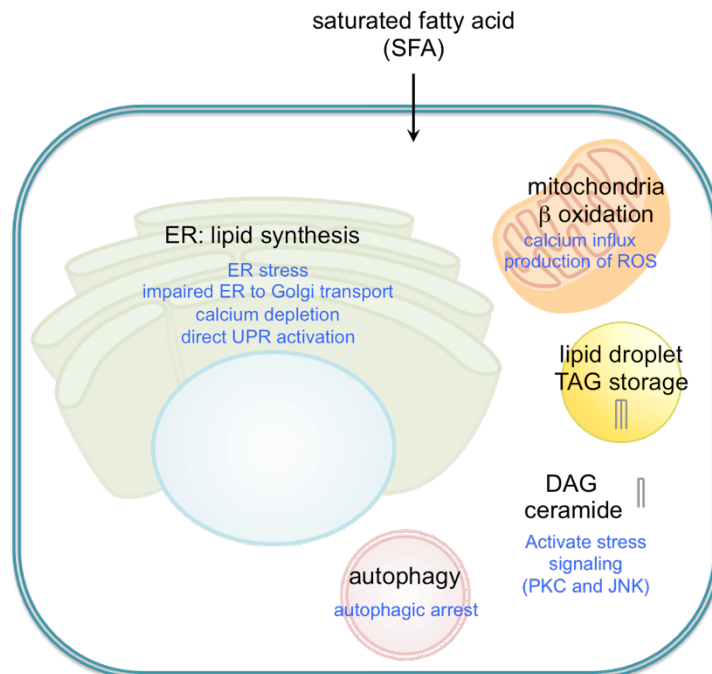
Figure 5.1 Fatty acid metabolism and mechanisms of lipotoxicity. The intracellular metabolism integrates many organelles (in black color). It can be imported into mitochondria for β oxidation, synthesized into lipid molecules in the endoplasmic reticulum (ER), and stored in lipid droplet (LD) as triacylglycerol (TAG). Mechanisms of lipotoxicity are categorized by the subcellular location where the adverse effects are exerted (in blue color).

5.2.1   Endoplasmic reticulum

The endoplasmic reticulum is the center for *de novo* lipid synthesis as well as a nutrient-sensing hub in cell. Thus it remains the most-studied mediators of lipotoxicity so far. The active lipid metabolic activity renders ER membrane composition subjective to alteration by incoming nutrients. For example, it was reported that SFA (e.g. palmitate) could elevate the saturation in ER membrane, which is correlated with dilation of ER and compromised ER integrity (*31*). Since ER is also responsible for the synthesis and folding of proteins, functional perturbation of ER is usually reflected in accumulation of unfolded proteins, i.e. ER stress. The unfolded protein

response (UPR) signaling will be activated to resolve such stress and ensure adequate protein quality control. UPR activation is also found correlated with alteration in membrane composition (*18*, *23*, *29*).

The triggers for ER stress during lipotoxicity remain a debate. Canonically, ER stress is caused by accumulation of unfolded proteins. Yet assessment of a protein folding reporter argues that protein folding is not affected under lipotoxic scenario (*48*). Moreover, misfolded proteins are dispensable for UPR activation (*49*). In cells specialized for secretion, alteration in ER membrane (exit site) may affect ER-to-Golgi transport, the resulting protein overload might cause ER stress (*48*, *50*). However, this is not supported by observation in different cell type (*51*). Besides protein and lipid synthesis, ER also maintains the largest cellular Ca^{2+} store to support the function of calcium-binding proteins in its lumen and to absorb excess Ca^{2+} from the cytosol. Maintenance of the store is energy consuming since Ca^{2+} is pumped into the ER against its chemical gradient (*52*). Given its critical role in ER function, ER calcium depletion is considered a classical UPR inducer. Interestingly, it is also widely observed in lipotoxic scenario and is proposed as potential mediator (*30*, *34*, *53*, *54*). Earlier mechanistic insights point to the sensitivity of an ER calcium pump, SERCA, to its lipid environment, e.g. cholesterol content (*55*) and phospholipid head group (*56*), which demonstrated its capability to transduce membrane stress to a more global level. Besides the canonical ER stress inducers, accumulating evidence argues for a direct role of lipid stress in UPR activation (*18*, *49*, *51*, *57*).

5.2.2 Mitochondria

Fatty acid is 'burned down' in mitochondria for energy supply, a process called beta oxidation.

Reactive oxygen species (ROS) and oxidative stress were shown to contribute to lipotoxicity

(*58*). It is tempting to believe that uncontrolled beta oxidation occurs with lipid overloading,

leading to ROS generation and release from mitochondria. However, surprisingly, experimental

evidence has uncoupled fatty acid beta oxidation from oxidative stress during lipotoxicity. For

example, inhibiting beta oxidation by blocking fatty acid transport into mitochondria did not

change but instead augmented ROS production and palmitate-induced cell death (*30, 59–61*).

Increasing beta oxidation might be beneficial through reducing lipid accumulation elsewhere.

Hence ROS might be generated in other means. One possibility is calcium influx and overload,

which leads to mitochondria membrane permeabilization (*60, 62*). This is related to ER calcium

homeostasis, either directly through ER-mitochondria contacts (*62*), or indirectly through uptake

of ER-released calcium (*60*).

5.2.3 Autophagy

Autophagy, or 'self eating', is the cell's strategy for waste disposal and recycle. The complete

cycle of autophagy starts from formation of autophagosome engulfing the cargo, and then fusion

between autophagosome and lysosome to break up the cargo (*63*). Autophagic arrest has been

documented in both *in vitro* lipotoxicity models or high-fat-diet models (*16, 30, 43*). Although

some studies reported lysosomal membrane permeabilization and subsequent release of cathepsin

to be responsible for lipotoxicity (*64*, *65*), most other reports demonstrated proper function of lysosome, and that suppression of autophagic turnover was in fact a result of failed autophagosome-lysosome fusion (*30*, *43*). Yet it remains a debate whether autophagic arrest is an independent response to lipid or secondary to other stress response. For example, as measured by the accumulation of ubiquitin and p62, autophagic arrest is shown to be dependent on ER stress in one study (*43*), but in another study independent of several canonical stress signaling pathways including ER stress (*30*). Impaired autophagic turnover can also be caused by elevated cytosolic calcium, since it can be partially alleviated by chelating cytosolic calcium or overexpressing ER calcium pump (*30*, *33*).

5.3 Concluding Remarks

Accumulating evidence points to the central role of ER in the initiation and execution of lipotoxicity. This is reasonable given that ER is most actively involved in lipid metabolism. Yet most of these aforementioned studies inevitably value the role of proteins over lipids, even in this case where lipids should rather be in the stage light. The underlying reasons might lie in the technical limitations in lipid research. Lipids are not biopolymers defined by the genetic codes, thus it is usually hard to manipulate and study the exact role of a specific lipid out of thousands of diverse species. Also, unlike proteins that can be GFP-tagged or immuno-labeled, there is not a good fluorescence imaging method to obtain spatial information for the lipid molecules, let alone reveal any possible local effects. Therefore, in the next chapter, with the aid of advanced

metabolic imaging by stimulated Raman scattering, we revisited the lipotoxic scenario from the perspective of lipids, and obtained novel insight into the immediate effect of excess lipid metabolism.

5.4 References

1. R. H. Eckel, S. M. Grundy, P. Z. Zimmet, in *Lancet* (2005), vol. 365, pp. 1415–1428.

2. G. Boden, Obesity and free fatty acids. *Endocrinol. Metab. Clin. North Am.* **37**, 635–46, viii–ix (2008).

3. J. D. McGarry, What if Minkowski had been ageusic? An alternative angle on diabetes. *Science.* **258**, 766–70 (1992).

4. F. Karpe, J. R. Dickmann, K. N. Frayn, Fatty acids, obesity, and insulin resistance: time for a reevaluation. *Diabetes*. **60**, 2441–9 (2011).

5. R. H. Unger, Lipotoxic Diseases. *Annu. Rev. Med.* **53**, 319–336 (2002).

6. R. T. Brookheart, C. I. Michel, J. E. Schaffer, As a matter of fat. *Cell Metab.* **10**, 9–12 (2009).

7. J. E. Schaffer, Lipotoxicity: when tissues overeat. *Curr. Opin. Lipidol.* **14**, 281–7 (2003).

8. T. J. Biden, E. Boslem, K. Y. Chu, N. Sue, Lipotoxic endoplasmic reticulum stress, β cell failure, and type 2 diabetes mellitus. *Trends Endocrinol. Metab.* **25**, 389–398 (2014).

9. A. K. Leamy, R. A. Egnatchik, J. D. Young, Molecular mechanisms and the role of saturated fatty acids in the progression of non-alcoholic fatty liver disease. *Prog. Lipid Res.* **52**, 165–74 (2013).

10. M. Prentki, C. J. Nolan, Islet beta cell failure in type 2 diabetes. *J. Clin. Invest.* **116**, 1802–12 (2006).

11. G. I. Shulman, Cellular mechanisms of insulin resistance. *J. Clin. Invest.* **106**, 171–6 (2000).

12. E. Karaskov *et al.*, Chronic palmitate but not oleate exposure induces endoplasmic reticulum

stress, which may contribute to INS-1 pancreatic β-cell apoptosis. *Endocrinology*. **147**, 3398–3407 (2006).

13. M. B. Hoppa *et al.*, Chronic palmitate exposure inhibits insulin secretion by dissociation of Ca2+ channels from secretory granules. *Cell Metab.* **10**, 455–465 (2009).

14. K. Eguchi *et al.*, Saturated fatty acid and TLR signaling link β cell dysfunction and islet inflammation. *Cell Metab.* **15**, 518–533 (2012).

15. D. A. Cunha *et al.*, Initiation and execution of lipotoxic ER stress in pancreatic beta-cells. *J. Cell Sci.* **121**, 2308–18 (2008).

16. G. Las, S. B. Serada, J. D. Wikstrom, G. Twig, O. S. Shirihai, Fatty acids suppress autophagic turnover in β-cells. *J. Biol. Chem.* **286**, 42534–42544 (2011).

17. H. Wen *et al.*, Fatty acid-induced NLRP3-ASC inflammasome activation interferes with insulin signaling. *Nat. Immunol.* **12**, 408–415 (2011).

18. M. M. Robblee *et al.*, Saturated fatty acids engage an IRE1α-dependent pathway to activate the NLRP3 inflammasome in myeloid cells. *Cell Rep.* **14**, 2611–2623 (2016).

19. M. Kratz *et al.*, Metabolic dysfunction drives a mechanistically distinct proinflammatory phenotype in adipose tissue macrophages. *Cell Metab.* **20**, 614–625 (2014).

20. X. Xu *et al.*, Obesity activates a program of lysosomal-dependent lipid metabolism in adipose tissue macrophages independently of classic activation. *Cell Metab.* **18**, 816–830 (2013).

21. R. G. Holzer *et al.*, Saturated fatty acids induce c-Src clustering within membrane subdomains, leading to JNK activation. *Cell*. **147**, 173–184 (2011).

22. P. P. H. Hommelberg, J. Plat, R. C. J. Langen, A. M. W. J. Schols, R. P. Mensink, Fatty acid-induced NF-κB activation and insulin resistance in skeletal muscle are chain length dependent. *Am. J. Physiol. Endocrinol. Metab.* **296**, E114-20 (2009).

23. G. Peng *et al.*, Oleate blocks palmitate-induced abnormal lipid distribution, endoplasmic reticulum expansion and stress, and insulin resistance in skeletal muscle. *Endocrinology*.

152, 2206–18 (2011).

24. C. Weigert *et al.*, Palmitate, but not unsaturated fatty acids, induces the expression of interleukin-6 in human myotubes through proteasome-dependent activation of nuclear factor-κB. *J. Biol. Chem.* **279**, 23942–23952 (2004).

25. D. Wang, Y. Wei, M. J. Pagliassotti, Saturated fatty acids promote endoplasmic reticulum stress and liver injury in rats with hepatic steatosis. *Endocrinology*. **147**, 943–51 (2006).

26. S. Fu, S. M. Watkins, G. S. Hotamisligil, The role of endoplasmic reticulum in hepatic lipid homeostasis and stress signaling. *Cell Metab.* **15**, 623–34 (2012).

27. H. Malhi, G. J. Gores, Molecular mechanisms of lipotoxicity in nonalcoholic fatty liver disease. *Semin. Liver Dis.* **28**, 360–9 (2008).

28. S. Mei *et al.*, Differential roles of unsaturated and saturated fatty acids on autophagy and apoptosis in hepatocytes. *J. Pharmacol. Exp. Ther.* **339**, 487–98 (2011).

29. A. K. Leamy *et al.*, Enhanced synthesis of saturated phospholipids is associated with ER stress and lipotoxicity in palmitate treated hepatic cells. *J. Lipid Res.* **55**, 1478–1488 (2014).

30. H.-W. Park *et al.*, Pharmacological correction of obesity-induced autophagy arrest using calcium channel blockers. *Nat. Commun.* **5**, 4834 (2014).

31. N. M. Borradaile *et al.*, Disruption of endoplasmic reticulum structure and integrity in lipotoxic cell death. *J. Lipid Res.* **47**, 2726–37 (2006).

32. C. I. Michel *et al.*, Small nucleolar RNAs U32a, U33, and U35a are critical mediators of metabolic stress. *Cell Metab.* **14**, 33–44 (2011).

33. M. J. Khan *et al.*, Inhibition of autophagy rescues palmitic acid-induced necroptosis of endothelial cells. *J. Biol. Chem.* **287**, 21110–21120 (2012).

34. S. Xu *et al.*, Palmitate induces ER calcium depletion and apoptosis in mouse podocytes subsequent to mitochondrial oxidative stress. *Cell Death Dis.* **6**, e1976 (2015).

35. T. Haffar, F.-A. Bérubé-Simard, J.-C. Tardif, N. Bousette, Saturated fatty acids induce endoplasmic reticulum stress in primary cardiomyocytes. *Endoplasmic Reticulum Stress Dis.*

2, 53–66 (2015).

36. H. Ariyama, N. Kono, S. Matsuda, T. Inoue, H. Arai, Decrease in membrane phospholipid unsaturation induces unfolded protein response. *J. Biol. Chem.* **285**, 22027–35 (2010).

37. E. Diakogiannaki, H. J. Welters, N. G. Morgan, Differential regulation of the endoplasmic reticulum stress response in pancreatic beta-cells exposed to long-chain saturated and monounsaturated fatty acids. *J. Endocrinol.* **197**, 553–63 (2008).

38. L. L. Listenberger *et al.*, Triglyceride accumulation protects against fatty acid-induced lipotoxicity. *Proc. Natl. Acad. Sci. U. S. A*. **100**, 3077–82 (2003).

39. K. Maedler *et al.*, Distinct effects of saturated and monounsaturated fatty acids on beta-cell turnover and function. *Diabetes*. **50**, 69–76 (2001).

40. C. Xiao, A. Giacca, A. Carpentier, G. F. Lewis, Differential effects of monounsaturated, polyunsaturated and saturated fat ingestion on glucose-stimulated insulin secretion, sensitivity and clearance in overweight and obese, non-diabetic humans. *Diabetologia*. **49**, 1371–9 (2006).

41. J. A. Chavez, S. A. Summers, Characterizing the effects of saturated fatty acids on insulin signaling and ceramide and diacylglycerol accumulation in 3T3-L1 adipocytes and C2C12 myotubes. *Arch. Biochem. Biophys*. **419**, 101–9 (2003).

42. O. Quehenberger *et al.*, Lipidomics reveals a remarkable diversity of lipids in human plasma. *J. Lipid Res*. **51**, 3299–305 (2010).

43. K. Miyagawa *et al.*, Lipid-Induced Endoplasmic Reticulum Stress Impairs Selective Autophagy at the Step of Autophagosome-Lysosome Fusion in Hepatocytes. *Am. J. Pathol.* **186**, 1–14 (2016).

44. T. Coll *et al.*, Oleate reverses palmitate-induced insulin resistance and inflammation in skeletal muscle cells. *J. Biol. Chem.* **283**, 11107–11116 (2008).

45. R. Volmer, D. Ron, Lipid-dependent regulation of the unfolded protein response. *Curr. Opin. Cell Biol.* **33**, 67–73 (2015).

46. J. Han, R. J. Kaufman, The role of ER stress in lipid metabolism and lipotoxicity. *J. Lipid Res.* **57**, 1329–38 (2016).

47. M. Erikci Ertunc, G. S. Hotamisligil, Lipid signaling and lipotoxicity in metabolic inflammation: indications for metabolic disease pathogenesis and treatment. *J. Lipid Res.*, 1–56 (2016).

48. A. M. Preston, E. Gurisik, C. Bartley, D. R. Laybutt, T. J. Biden, Reduced endoplasmic reticulum (ER)-to-Golgi protein trafficking contributes to ER stress in lipotoxic mouse beta cells by promoting protein overload. *Diabetologia.* **52**, 2369–2373 (2009).

49. R. Volmer, K. van der Ploeg, D. Ron, Membrane lipid saturation activates endoplasmic reticulum unfolded protein response transducers through their transmembrane domains. *Proc. Natl. Acad. Sci. U. S. A.* **110**, 4628–33 (2013).

50. E. Boslem *et al.*, Alteration of endoplasmic reticulum lipid rafts contributes to lipotoxicity in pancreatic β-cells. *J. Biol. Chem.* **288**, 26569–82 (2013).

51. Y. Kitai *et al.*, Membrane lipid saturation activates IRE1α without inducing clustering. *Genes to Cells.* **18**, 798–809 (2013).

52. A. P. Arruda, G. S. Hotamisligil, Calcium homeostasis and organelle function in the pathogenesis of obesity and diabetes. *Cell Metab.* **22**, 381–397 (2015).

53. T. Hara *et al.*, Calcium efflux from the endoplasmic reticulum leads to β-cell death. *Endocrinology.* **155**, 758–768 (2014).

54. Y. Wei, D. Wang, C. L. Gentile, M. J. Pagliassotti, Reduced endoplasmic reticulum luminal calcium links saturated fatty acid-mediated endoplasmic reticulum stress and cell death in liver cells. *Mol. Cell. Biochem.* **331**, 31–40 (2009).

55. Y. Li *et al.*, Enrichment of endoplasmic reticulum with cholesterol inhibits sarcoplasmic-endoplasmic reticulum calcium ATPase-2b activity in parallel with increased order of membrane lipids: Implications for depletion of endoplasmic reticulum calcium stores and apoptos. *J. Biol. Chem.* **279**, 37030–37039 (2004).

56. S. Fu *et al.*, Aberrant lipid metabolism disrupts calcium homeostasis causing liver endoplasmic reticulum stress in obesity. *Nature*. **473**, 528–31 (2011).

57. K. Halbleib *et al.*, Activation of the Unfolded Protein Response by Lipid Bilayer Stress. *Mol. Cell*. **35**, 1997–2004 (2017).

58. J. Liu *et al.*, Palmitate promotes autophagy and apoptosis through ROS-dependent JNK and p38 MAPK. *Biochem. Biophys. Res. Commun.* **463**, 1–6 (2015).

59. M. B. Paumen, Y. Ishida, M. Muramatsu, M. Yamamoto, T. Honjo, Inhibition of carnitine palmitoyltransferase I augments sphingolipid synthesis and palmitate-induced apoptosis. *J. Biol. Chem.* **272**, 3324–3329 (1997).

60. R. A. Egnatchik, A. K. Leamy, D. A. Jacobson, M. Shiota, J. D. Young, ER calcium release promotes mitochondrial dysfunction and hepatic cell lipotoxicity in response to palmitate overload. *Mol. Metab.* **3**, 544–53 (2014).

61. M. Masuda *et al.*, Saturated phosphatidic acids mediate saturated fatty acid-induced vascular calcification and lipotoxicity. *J. Clin. Invest.* **125**, 4544–4558 (2015).

62. A. P. Arruda *et al.*, Chronic enrichment of hepatic endoplasmic reticulum-mitochondria contact leads to mitochondrial dysfunction in obesity. *Nat. Med.* **20++**, 1427–35 (2014).

63. N. Mizushima, T. Yoshimori, B. Levine, Methods in Mammalian Autophagy Research. *Cell*. **140**, 313–326 (2010).

64. A. E. Feldstein *et al.*, Free fatty acids promote hepatic lipotoxicity by stimulating TNF-alpha expression via a lysosomal pathway. *Hepatology*. **40**, 185–94 (2004).

65. F. G. Almaguel *et al.*, Lipotoxicity-mediated cell dysfunction and death involve lysosomal membrane permeabilization and cathepsin L activity. *Brain Res.* **1318**, 133–143 (2010).

Chapter 6

Metabolic imaging reveals endoplasmic reticulum structural remodeling and perturbation

by saturated fatty acid

6.1 Abstract

Being the central organelle for lipid metabolism, the endoplasmic reticulum (ER) has received increasing attention for its role in sensing, initiation and execution of lipotoxicity caused by saturated fatty acids (SFAs). In most of the earlier studies, it is almost taken for granted that SFA increases the overall saturation of ER membrane, without careful evaluation of ER's architecture. Even though some studies have noticed ER structural remodeling and realized its relation to the adverse effects of SFA (*1–3*), the alterations occurred to ER has not been described in detail, neither is known how it is related to fatty acid metabolism or increased saturation in ER membrane. Hence in this chapter, I will describe our attempts towards the above question. By fluorescence imaging, ER is found to undergo expansion in sheet-like structures yet substantial loss of tubules, which is correlated with reduction of ER luminal connection. More importantly, metabolic imaging by stimulated Raman scattering (SRS) reveals that expanded ER membrane is a result of SFA-derived lipid metabolites accumulating locally. We also provide previously unknown link between ER remodeling and autophagic arrest.

6.2 Palmitate remodels ER structure

SFA-induced ER structural alteration has been mainly described as ER expansion, which seems to be a natural result of membrane lipid synthesis promoted by SFA (*1*, *3*). Yet paradox arises when attempting to attribute the adverse effects to ER expansion, since ER expansion is one of the rescuing mechanisms documented in pro-survival unfolded protein response (UPR) signaling

(*4*). Usually, the expanded volume and membrane area provides more space for protein folding thus alleviating the protein load in ER. The seemingly different mode by SFA motivated us to systematically examine how ER is remodeled.

We first visualized ER by simultaneously expressing two fluorescent ER markers, luminal marker ER-GFP and membrane marker mCherry-Sec61β. We treated the cells with 400μM palmitate and acquired time-lapse images every 30min thereafter for 5 hrs **(Figure 6.1)**. Within this time window ER stress has not been detectable according to others' reports (*2*, *5*). We observed that palmitate treatment gradually expanded ER membrane area according to mCherry fluorescence, which may correspond to 'ER expansion' mentioned earlier. However, unexpectedly, it is not always accompanied by simultaneous expansion in the ER lumen, according to GFP fluorescence. We noted that the peripheral ER network has two morphologically distinct domains known as sheet and tubules, which refers to flat and cylindrical part of ER, respectively. The time-lapse imaging also suggests distinct evolution of sheets and tubules, reflected in the growth of ER sheet and meanwhile loss of ER tubules **(Figure 6.1 A)**.

Next we further characterized how palmitate remodels luminal space. The degeneracy of the intricate network architecture motivated us to examine ER luminal connectivity by measuring fluorescence loss in photobleaching (FLIP) with the luminal marker, ER-GFP **(Figure 6.1 B to G)**. The magnified images consistently show disappearance of tubules after palmitate treatment

(Figures 6.1 C and F). After 80-s photo bleaching, we quantified the residual fluorescence with respect to distance from the bleaching center, and compared between palmitate treatment and control. The normal ER appeared as an interconnected network, according to homogeneous photobleaching across the cytoplasm **(Figure 6.1 D)**. However, compartmentalized bleaching of ER-GFP fluorescence was observed after palmitate treatment. Specifically, fluorescence is severely lost in proximal area surrounding the laser spot but remain nearly unchanged in area further away from the laser spot **(Figure 6.1 G)**.

Together, fluorescence imaging has revealed in detail how palmitate remodels ER. Namely, palmitate expands the sheet-like ER membrane but not ER lumen, which is correlated with loss of ER tubules and luminal connectivity.
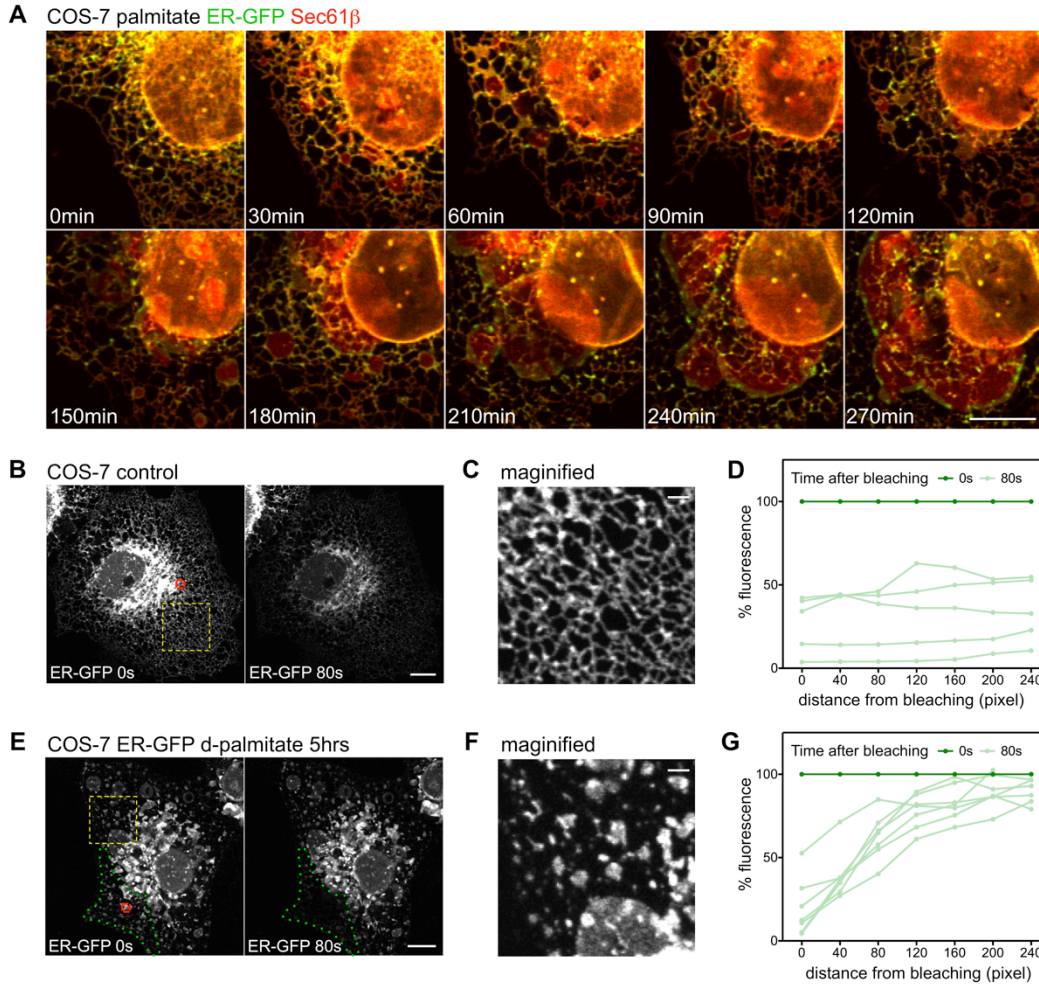
Figure 6.1 Fluorescence ER markers reveals ER remodeling by palmitate. (A) Fluorescence time-lapse images of a COS-7 cell expressing ER-GFP and mCherry-Sec61β. Images were taken every 30min after treatment with 400μM palmitate, and overlay between GFP (green) and mCherry (red) are shown. **(B** and **E)** Fluorescence loss in photobleaching (FLIP) in ER-GFP transfected COS-7 cells, control (B) and after 5-hr palmitate treatment (E). Repetitive photobleaching was performed in red-boxed areas for indicated time. Green dotted line in (E) delineates compartment of local photo-bleaching. **(C** and **F)** Magnified views showing ER tubular network in yellow boxed area of (B) and (E), respectively. **(D** and **G)** Normalized residual fluorescence after bleaching for 80s. Mean fluorescence intensity is calculated in a ring area that has indicated distance from bleaching center. Normalization is performed with the fluorescence intensity at 0s. Scale bars, 10μm in (A) (B) and (E), 2μm in (C) and (F). Pseudo colors used: GFP (green), mCherry (red).

6.3 Palmitate metabolites form membrane domains on ER

We then asked if ER structural alteration is directly associated with *de novo* lipid synthesis from palmitate. To get the spatial information of lipid metabolites, we harnessed metabolic imaging by stimulated Raman scattering (SRS). Basically, we used deuterated palmitate (d-palmitate) in which hydrogen in palmitate is substituted with deuterium. The carbon-deuterium (C-D) bond therein will be carried over to its lipid metabolites. The unique vibrational frequency of C-D bond (around 2100 cm^{-1}) in the cell-silent region distinguishes these nascent lipid molecules from a myriad of cellular lipids, allowing quantitative concentration mapping by chemically selective SRS microscopy. We then correlate the chemical map by SRS with fluorescent markers in cell, such as ER markers, to evaluate the effects of lipid metabolites on ER.

We first imaged d-palmitate metabolites in HeLa cells expressing the luminal ER marker, ER-GFP **(Figure 6.2 A and B)**. Earlier we have shown that palmitate promote synthesis of fully saturated lipids, which gradually accumulate and form domains in ER membrane **(Chapter 4)**. Consistently, C-D SRS channel reveals scattering membrane domains enriched with the newly synthesized lipids. These membrane domains colocalizes well with ER-GFP in the early stage of palmitate metabolism when their sizes are relatively small **(Figure 6.2 A)**. Even the spatial correlation between C-D SRS and GFP fluorescence is partially lost at later stage when the domains expand, ER-GFP can still be found on the rim of these domains **(Figure 6.2 B)**. Similar spatial correlation exists in ER-GFP-expressing COS-7 cell exposed to d-palmitate **(Figure 6.3**

A and B), as well as another long chain SFA, stearate **(Figure 6.3 C)**. As demonstrated aforehand **(Chapter 4)**, these domains form spontaneously as a result of accumulating saturated lipids, thus the correlative metabolic and fluorescence imaging suggests ER remodeling to be a direct result of lipid metabolism.
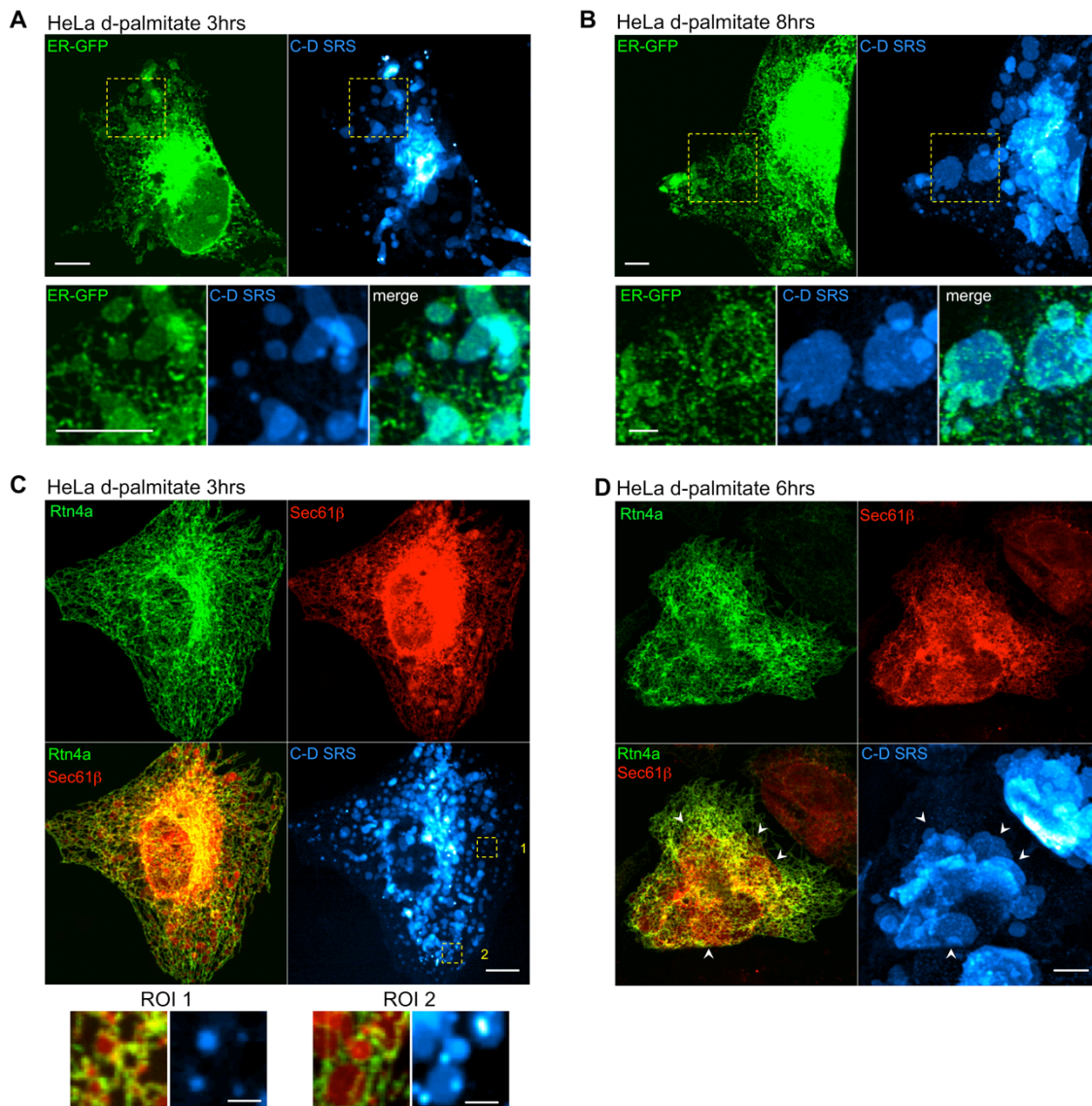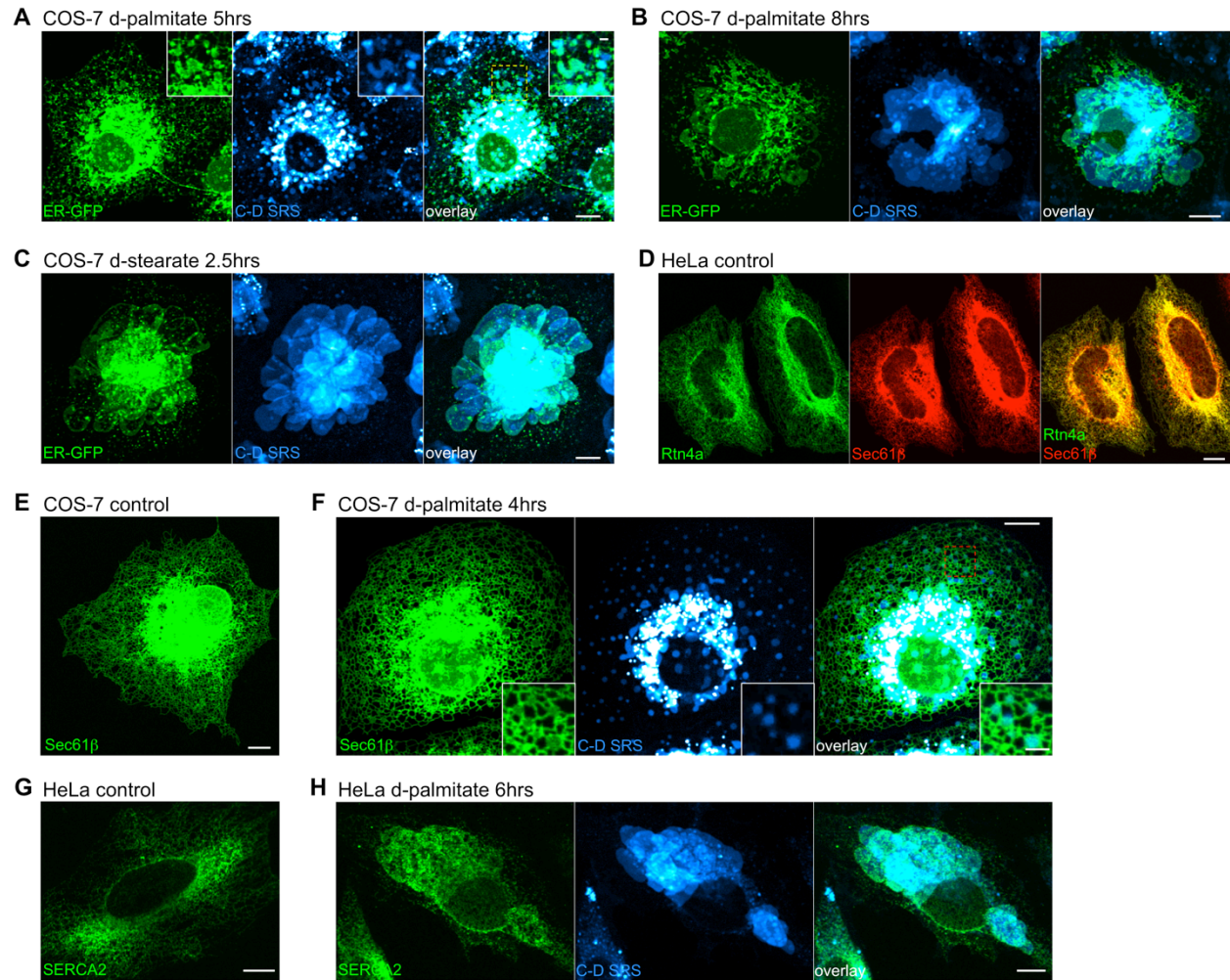

Figure 6.2 Correlative metabolic imaging of d-palmitate and fluorescence imaging of ER markers. (A and **B)** HeLa cells expressing ER-GFP were treated with d-palmitate for 3 hrs (A) and 8 hrs (B). Magnified images were

shown for the boxed areas. Scale bars, 10μm in upper row, 5μm in bottom row. **(C** and **D)** HeLa cells co-expressing Rtn4a-GFP and mCherry-Sec61β were treated with d-palmitate for 3 hrs (C) and 6 hrs (D). Scale bars, 10μm. Magnified images were shown for two ROIs (boxed areas) in (C). Scale bars, 2μm. Arrows point to large ER sheets in (D). Pseudo colors used: GFP (green), mCherry (red), C-D SRS (cyan hot).

We futhur evaluated the localization of ER membrane markers with respect to the d-palmitate-derived domains, including ER tubular marker Rtn4a, membrane protein Sec61β, and membrane protein SERCA2. Rtn4a localize to tubular ER to form high curvature (*6*). Thus in cells co-expressing Rtn4a-GFP and mCherry-Sec61β, both markers can be found on ER tubules **(Figure 6.3 D)**, while ER sheet will be contrasted out as high mCherry fluorescence but low GFP fluorescence. Thus we applied this stratedgy to HeLa cells treated by d-palmitate. Interestingly, domains in C-D SRS channels colocalize well with the putative ER-sheet domains at both early stage **(Figure 6.2 C)** and late stage **(Figure 6.2 D)**. More spatial correlation can be obtained in COS-7 cell expressing mCherry-Sec61β **(Figure 6.2 E and F)** and HeLa cells stained with anti-SERCA2. The consistency of spatial patterns among various ER proteins thus rules out the protein-specific interaction with palmitate metabolites, and supports that expansion of ER sheet is a direct result of palmitate-derived lipid metabolism.

Figure 6.3 More correlative metabolic and fluorescence images in supplementation to Figure 6.2. (A and **B)** COS-7 cells expressing ER-GFP were treated with d-palmitate for 5 hrs (A) and 8 hrs (B). Magnified images were shown for the boxed areas in (A). Scale bars, 10μm in main image, 2μm in inset. **(C)** COS-7 cells expressing ER-GFP were treated with d-stearate for 2.5 hrs. Scale bar, 10μm. **(D)** HeLa cells co-expressing Rtn4a-GFP and mCherry-Sec61β. **(E** and **F)** COS-7 cells expressing mCherry-Sec61β were treated with control (E) or d-palmitate for 4 hrs (F). Magnified images were shown for the boxed areas in (F). Scale bars, 10μm in main image, 2μm in inset.Scale bar, 10μm. **(G** and **H)** HeLa cells, control (G) or d-palmitate treated for 4 hrs (H), were stained with anti-SERCA2. Scale bars, 10μm. Pseudo colors used: GFP and anti-SERCA2 (green), mCherry (red), C-D SRS (cyan hot).

6.4 Ultra-structural study of ER remodeling by palmitate

Based on the observations that palmitate-derived membrane domains expand ER sheet while gradually squeezing out luminal ER-GFP, we propose the following model to describe the local effect of lipid metabolism on ER architecture **(Figure 6.4)**. The high rigidity in the saturated lipid domains drives the expansion of low-curvature sheet-like ER. Yet the expanded ER cannot support the luminal spacing, and is consequently deprived of luminal protein like ER-GFP.
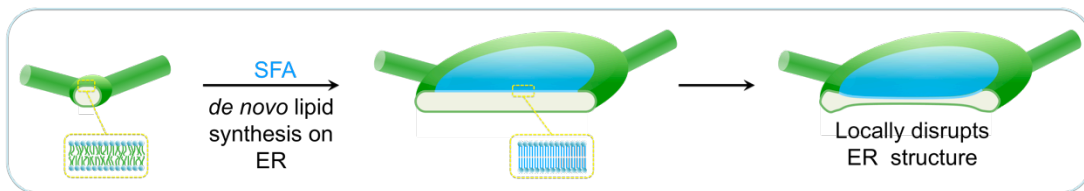
Figure 6.4 Proposed model for ER structural remodeling by saturated fatty acid. The SFA-derived domain (shown in blue) distends ER membrane yet fails to support ER luminal space.

To validate this model, we studied the palmitate-induced structural changes by transmission electron microscopy (TEM). We reasoned that the high saturation in palmitate-derived membrane would provide weaker contrast in osmium (Os) based positive staining, since usually membrane fixation and staining relies on reaction between OsO_4 and carbon-carbon double bonds in unsaturated fatty acyl group (*7*). Indeed, lost of membrane staining was evident in previous studies that employed TEM (*1, 2, 8*) as well as our own attempt using OsO_4 stain (Data not shown).

To improve visualization of membrane, we then explored the more reactive staining with $K_4Fe(CN)_6$ and OsO_4 (known as 'reduced osmium', later referred to as FeOs). The results were indeed improved **(Figure 6.5)**. In control cells, ER appears as two parallel lines spaced by 30-60nm, which is typical of ER luminal width **(Figure 6.5 A)**. When cells were treated with 400μM palmitate for 4 hrs, observable changes occurred on ER, characterized by narrower luminal spacing and uneven staining on the two parallel lines of membrane **(Figure 6.5 B)**. Since FeOs method still relies on unsaturation for contrast, the uneven staining implies the highly saturated domains in ER. Meanwhile the narrowed spacing lends support to the proposed model. Note that they are part of ER since they are continuous with ER membrane (with normal symmetric staining and luminal width). The lumen becomes too narrow at some place that two parallel membranes are barely resolvable by TEM.
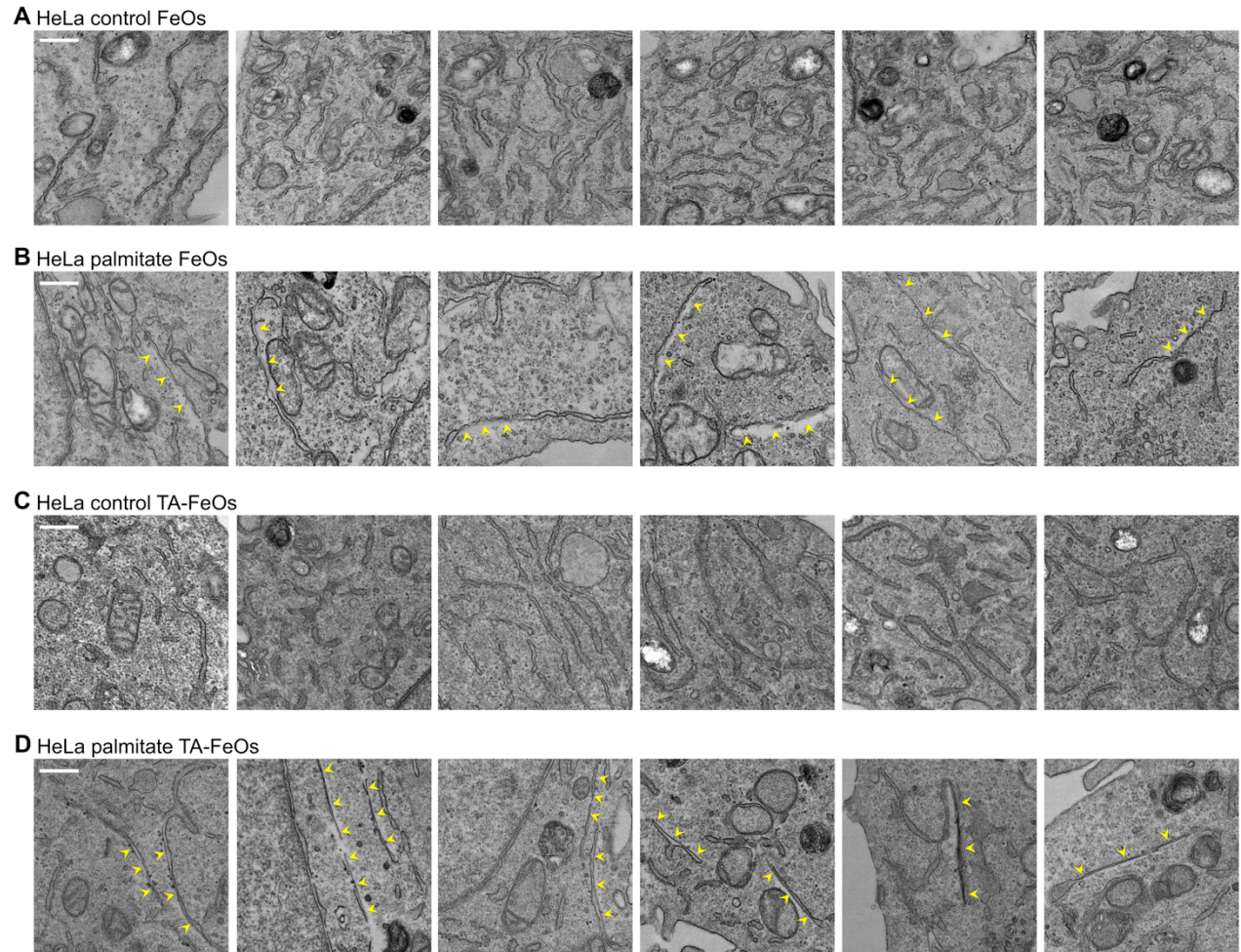
Figure 6.5 Improved TEM staining method reveals narrowed luminal spacing associated with putative palmitate-derived membrane. (A to **D)** Figures show TEM images acquired for control (A) or cells treated with 400μM palmitate for 4 hrs (B). Cells were treated accordingly, fixed and stained by FeOs method. Arrows indicate weaker-stained side and putatively the palmitate-derived membrane. **(C** and **D)** Figures show TEM images acquired for control (C) or cells treated with 400μM palmitate for 4 hrs (D). Cells were treated accordingly, fixed and then stained by TA-FeOs method. Arrows indicate flat and putatively palmitate-derived membrane. Scale bars, 500nm.

To better preserve membrane structure, especially the palmitate-derived membrane domains, we tried tannic acid together with reduced osmium (TA-FeOs) as commonly used in block face EM imaging. TA has been reported to preserve membranes rich in saturated phosphatidylcholine,

possibly through stabilizing the choline head group (*9*). Since lipidomics reveals phosphatidylcholine to be a major component of solid membrane **(Chapter 4)**, TA might also work well in solid domains. Indeed, both membrane preservation and staining contrast were improved with TA addition, as evidenced by less membrane rupture and blurring **(Figure 6.5 C and D)**. The uneven staining between opposing membranes was reduced, possibly as a result of TA. With this method, palmitate treatment consistently induced narrower ER lumen. Interestingly, these parts of ER exhibit fewer irregular ruffles in membrane on one side than the other side of the lumen **(Figure 6.5 D)**. In comparison, such ruffles are common in control cells and account for the fluctuation of ER luminal width **(Figure 6.5 C)**. Again, this supports our model in which a narrower lumen is bounded by a rigid membrane.

In summary, by rational selection of staining protocol, we were able to identify the putative palmitate-derived membranes under TEM. These membranes are characterized by high saturation and/or low curvature, and more importantly, association with narrower ER lumen. Therefore the above TEM analysis is consistent with observations form optical imaging, and supports the proposed model with unparalleled resolution **(Figure 6.4)**.

6.5 Palmitate-derived membrane domains are in close proximity to mitochondria

We then asked if the palmitate metabolites appeared at special locations on the ER. Recent findings suggest that lipid synthesis enzymes are enriched in mitochondria-associated membrane

(MAM) and that ER-mitochondria contact provides the membrane source for autophagosome (*10*, *11*). Therefore, in addition to the ER markers, we also included mitochondria as an imaging target. We applied a short-pulse treatment of d-palmitate to cells and imaged the newly formed domains together with mitochondria and ER, marked respectively by MitoTracker and ER-GFP **(Figure 6.6 A to E)**. In this way, the domains are small enough to be separated from each other, which also makes it more reliable for colocalization analysis regarding sub-micron ER and mitochondria structure. Consistently, these domains localize to ER. We overlay the mitochondria (red) and ER (green) image to obtain the overlapped pixels (yellow), which to some extent represent ER-mitochondria contact (ER-mito) (*10*). In this way, we observed that some membrane domains localized in the close vicinity of ER-mito contact **(Figure 6.6 B to E)**. In agreement with optical microscopic analysis, electron microscopy also implicated ER-mito proximity at places of putative palmitate-derived membrane **(Figure 6.6 F to I)**. Altogether, our observation suggested the mitochondria-associated ER to be a possible site for palmitate metabolites accumulation.
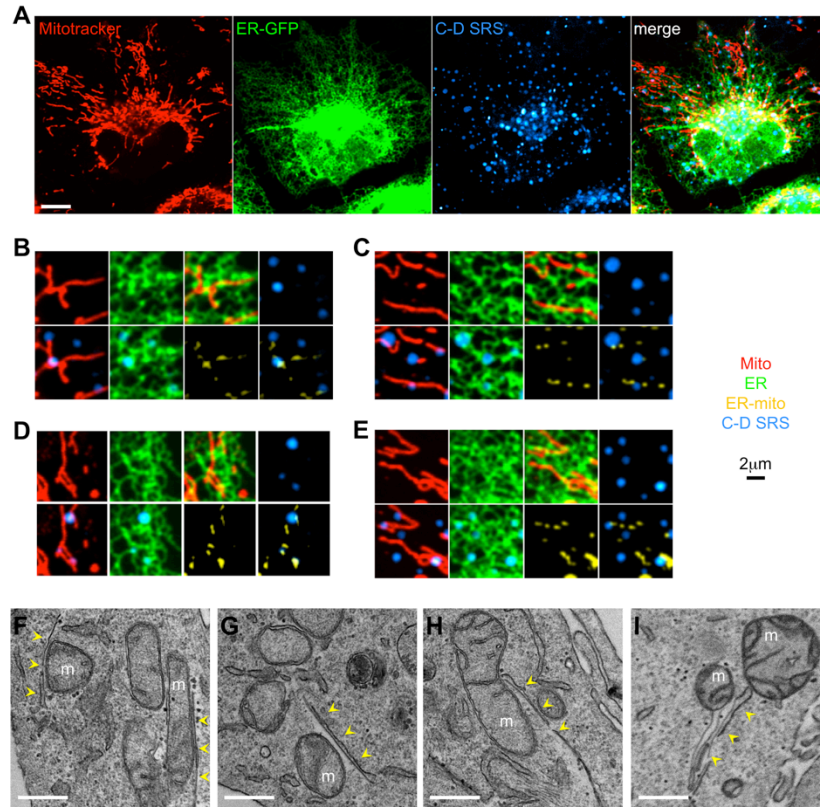
Figure 6.6 ER-mitochondria contact might be a hot spot for generation of membrane domains. (A to **E)** ER-GFP expressing HeLa cells were treated with 400μM palmitate for 20min and stained by MitoTracker Deep Red. Individual channels and their overlay are shown in (A). Scale bar, 10μm. Pseudo colors used: GFP (green), MitoTracker (red), C-D SRS (cyan hot). Magnified images are shown in (B) to (E). Colocalized pixels between Mito (red) and ER (green) channels were picked up and shown as 'ER-mito' (yellow). Overlay images were shown for following combinations: [Mito, ER], [Mito, C-D], [ER, C-D], and [ER-mito, C-D]. Scale bars, 2μm. **(F** to **I)** TEM images acquired for cells treated with 400μM palmitate for 4 hrs and then stained by TA-FeOs method. Arrows indicate putative palmitate-derived membrane. 'm', mitochondria. Scale bars, 500nm.

6.6 Local autophagic arrest is found on palmitate-derived membrane domain

The appearance of membrane domains raised the question whether they locally exert functional perturbation beyond ER structural remodeling. Activation of selective autophagy is evident in

earlier studies of lipotoxic scenarios (*12*, *13*). Based on the current observation and the proposed model **(Figure 6.4)**, we speculated that although palmitate-derived membrane expands ER, these nascent ER domains might not bear proper function due to lack of luminal spacing, hence these domains would be destined for removal by selective autophagy. We then tested this by visualizing sequestosome 1 (p62), a receptor for selective autophagy (*14*). Once p62 recognizes targets, it will cluster and recruit autophagic machinery. In quiescent control cell, p62 distributes across the cytosol (inactive state) **(Figure 6.7 A)**. Yet when sizable membrane domains emerged in the C-D SRS channel, p62 formed punctate or annular clusters (activated state) **(Figure 6.7 B)**. We found that almost all cells turned to the activated state when the largest domain in the cell exceeded a certain size (area~$30\mu m^2$, d~$6\mu m$) **(Figure 6.7 C)**. Moreover, correlative imaging of p62 and solid membrane reveals that most p62 clusters localized at individual membrane domains (area>$10\mu m^2$, d>$2\mu m$) **(Figure 6.7 D)**. Similar results were obtained in HepG2 and mouse fibroblast, both showing p62 clustering on the expanded membrane of palmitate metabolites **(Figure 6.8)**. p62 recognizes protein ubiquitination, a signal for degradation for its activation (*14*). Indeed, ubiquitin also accumulated near the membrane domains with p62 clustered around **(Figure 6.7 E)**. All together, we confirmed that palmitate activated selective autophagy, and revealed the autophagic target to be associated with palmitate-derived membrane domains, if not themselves. Note that such local action is not achievable by other coincident effects of SFAs and imply the causative role of the membrane domains.
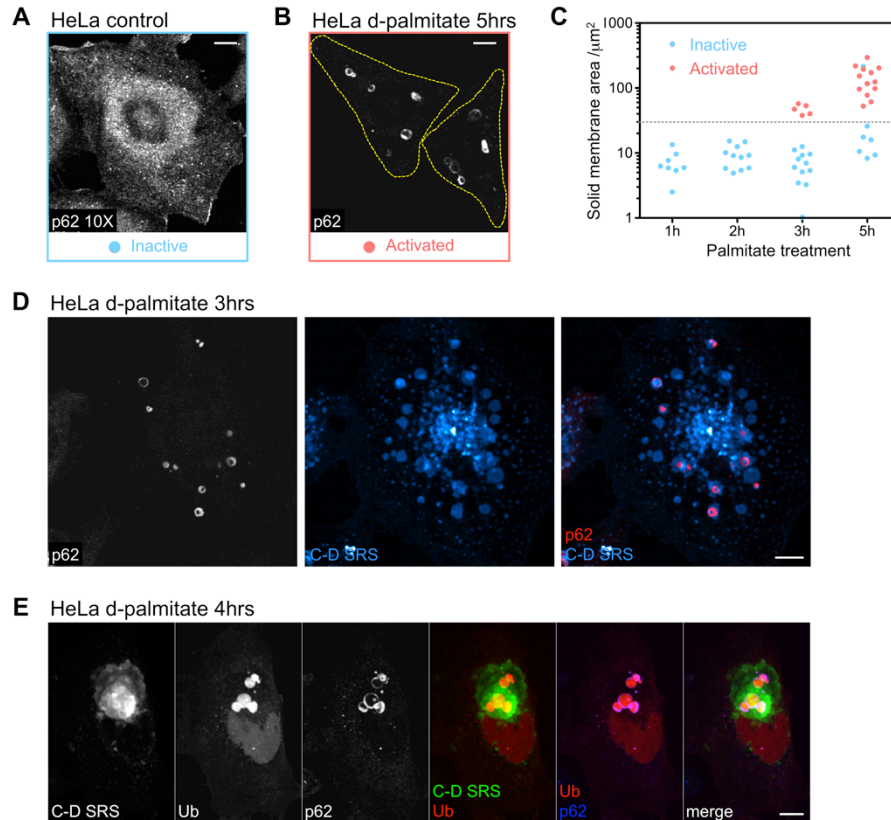
Figure 6.7 Palmitate-derived membrane domains activate selective autophagy. (A) p62 immunofluorescence in control HeLa cell, referred to as 'inactive' state. The intensity has been adjusted to 10-fold brighter to visualize the weak basal p62 signal. **(B)** p62 immunofluorescence in HeLa cell after 5-hr d-palmitate treatment, referred to as 'activated' state. **(C)** Cells are classified as p62-inactive or p62-activated according to p62 staining pattern shown in (A) and (B). The area of the largest membrane domain (from C-D SRS) in the cell are calculated and plotted. **(D)** p62 immunofluorescence, C-D SRS, and their overlay images in HeLa cell after 3-hr d-palmitate treatment. Pseudo colors used: p62 (red), C-D SRS (cyan hot). **(E)** GFP-Ub transfected HeLa cells were treated with d-palmitate for 4 hrs and immunostained with p62. Pseudo colors used: C-D SRS (green), Ub (red), p62 (blue). Scale bars, 10μm.
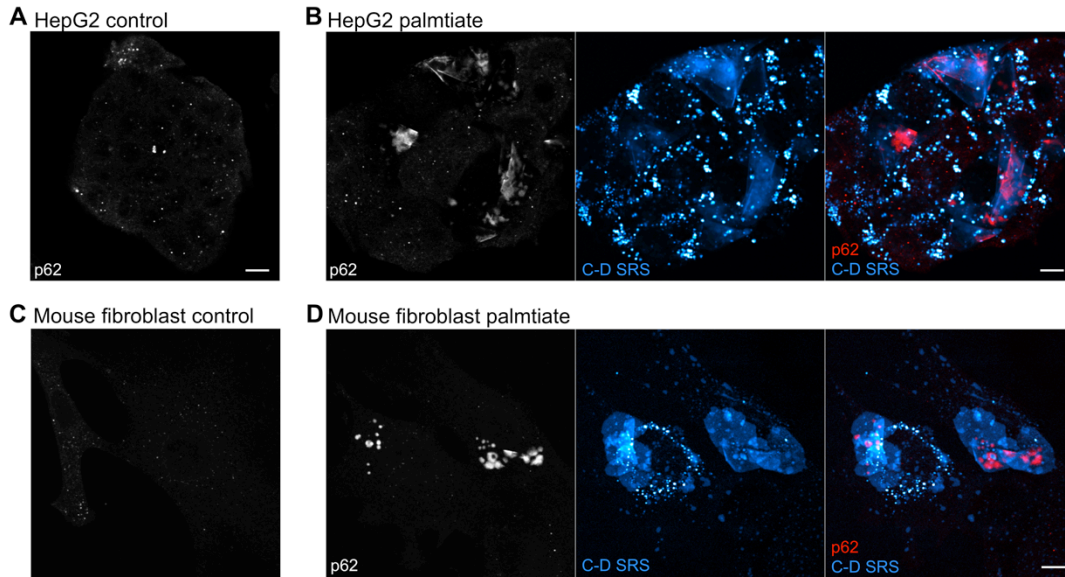
Figure 6.8 p62 clustering on palmitate-derived membrane domains in HepG2 and mouse fibroblast. (A and **B)** p62 immunofluorescence in HepG2 cell for control (A) or treated with d-palmitate for 5h (B). **(C** and **D)** p62 immunofluorescence in mouse fibroblasts for control (C) or treatment with d-palmitate for 2h (D). Pseudo colors used: p62 (red), C-D SRS (cyan hot). Scale Bars: 10μm.

Persistent p62 clustering is also regarded as a sign of impaired autophagic turnover (*15*), which has been documented in *in vitro* studies of lipotoxicity using palmitate (*16–18*) as well as in diet-induced obese mice (*12, 13*). Given the intimate relation between ER homeostasis and autophagy, we thus tested the autophagic function in this context. We first imaged the autophagosome marker LC3, and found abnormally large plaques exceeding the usual submicron size of autophagosomes **(Figure 6.9 A)**. These plaques are localized to p62 clusters, suggesting LC3 is recruited onsite by p62. We then examined autophagic turnover by a tandem RFP-GFP-LC3 sensor (*15*). Upon successful fusion with acidic lysosomes, the original 'yellow' LC3 would turn red due to quenching of GFP (but not RFP) fluorescence. Remarkably, large

LC3 plaques associated with the membrane domains (C-D SRS) were rarely found to fuse with acidic lysosomes **(Figure 6.9 B)**. On the other hand, acidic lysosomes as stained by LysoTracker were not depleted in the meanwhile **(Figure 6.10)**, suggesting that the autophagic arrest was a result of incompetent fusion between autophagosome and lysosome. Conversely, inhibited autophagic turnover could in turn aggravate the membrane stress itself, as evidenced by more solid-like membranes in cells treated with a lysosome inhibitor, chloroquine (CQ) **(Figure 6.9 C and D)**. Together, such a vicious cycle induced by the membrane domains might directly contribute to SFA lipotoxicity by undermining rescuing efforts of autophagy along pro-survival stress signaling (*19*) **(Figure 6.9 E)**.
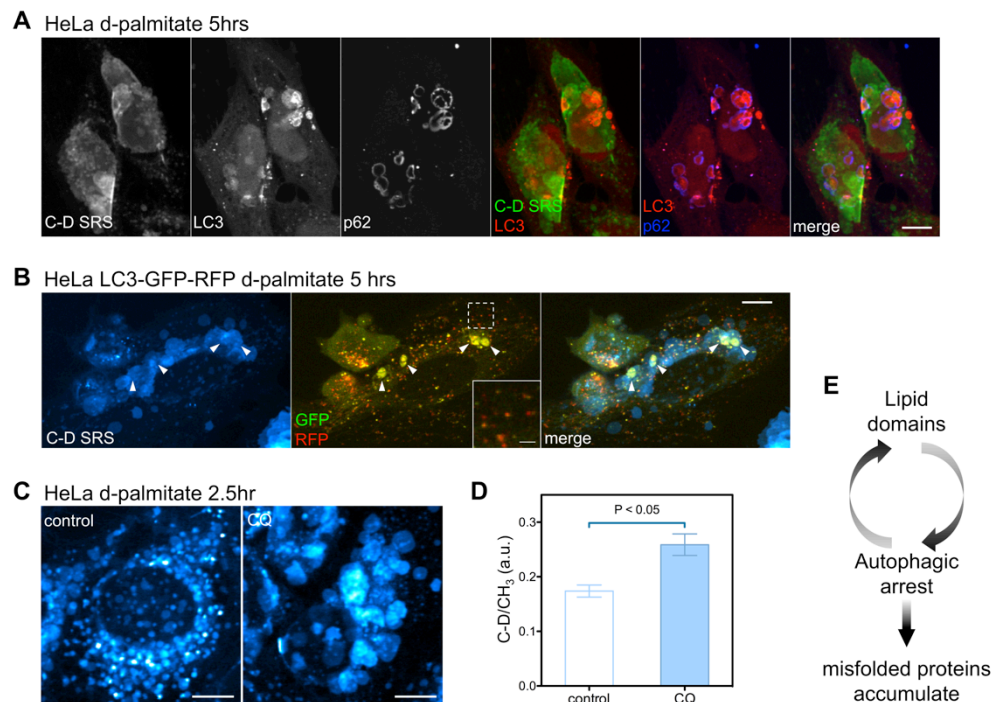
Figure 6.9 Palmitate-derived membrane domains correlate with local autophagic arrest. (A) EGFP-LC3 transfected HeLa cells were treated with d-palmitate for 5hrs and immunostained with p62. Pseudo colors used: C-D

SRS (green), LC3 (red), p62 (blue). **(B)** C-D SRS image and merged fluorescence image of RFP-GFP-LC3 transfected HeLa cells. Inset shows small LC3 clusters with successful fusion to lysosomes (red) in boxed area. Arrowheads mark large LC3 plaques with impaired fusion (yellow). C-D SRS is pseudo-colored cyan hot. **(C** and **D)** HeLa cells were treated by d-palmitate for 2.5hrs without or with chloroquine (CQ). Representative C-D SRS images are shown in (D). Quantification of normalized C-D SRS signal is shown in (D). Data are presented as mean ± SEM. n = 4, p < 0.05 (student's t-test). **(E)** Illustration of vicious cycle caused by domains of lipid metabolites. Scale bars, 10μm except the inset in (B), 2μm.
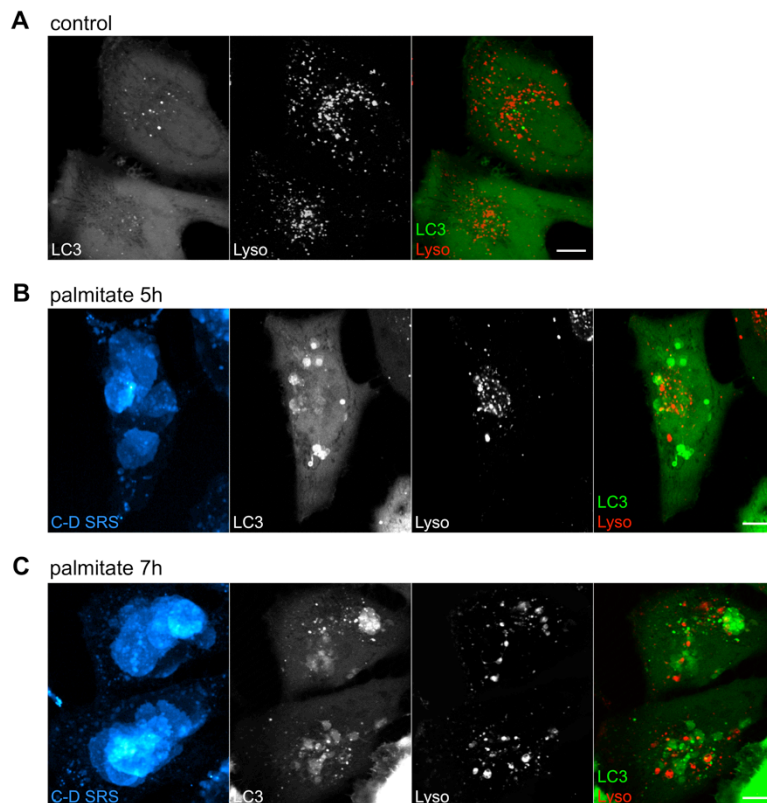
Figure 6.10 Visualization of lysosomes in cells developing large LC3 plaques after palmitate treatment. HeLa cells expressing EGFP-LC3 were stained by Lysotracker Red after palmitate treatment. **(A)** control; **(B** and **C)**, palmitate-treated for 5hrs (B) or 7 hrs (C). Pseudo colors used: C-D SRS (cyan hot), LC3 (green), LysoTracker (red). Scale bars, 10μm.

6.7 Conclusion and Discussion

Here we have described ER structural remodeling in terms of its membrane, lumen, and its morphology. Taking advantage of metabolic imaging that couples SRS microscopy with minimally perturbative isotope labeling, we found that ER structural remodeling is a direct effect of membrane domains formed by accumulating palmitate metabolites. Functionally, the resulting ER membrane domains activate selective autophagy by locally clustering p62. Yet they are correlated with local autophagic arrest. Together with the solid-phase-like characteristic described in **Chapter 4** and the locally disturbed ER homeostasis observed here, our study recalls attention to fundamental membrane biophysical mechanisms that could underlie lipid-mediated stress initiation and signaling. For example, detergent-resistant membrane was implicated in JNK activation in obese mice (Holzer et al., 2011); in another study, phosphatidic acid, which bears high-T_m, was found to mediate lipotoxic vascular calcification in scd-deficient mouse (Masuda et al., 2015). The detrimental effects of solid-like membrane might not be limited to these local effects. ER membrane proteins, e.g. IRE1α and SERCA2b, could be potential molecular linkers that connect solid-phase membrane to stress signaling in a more global context. The ER stress sensor IRE1α can be activated upon increase in membrane saturation even without its luminal domain that is essential in the canonical UPR (Volmer et al., 2013). A recent study reveals that palmitate treatment activates IRE1α without inducing its clustering; instead, IRE1α distribution highly resembles fragmented ER (Kitai et al., 2013). Such noncanonical modes of action of IRE1α might be related to the appearance of solid membrane

domain following palmitate treatment. Similarly, the ER-resident Ca^{2+} pump SERCA2b, which mediates liver ER stress in obesity by depleting ER Ca^{2+} store (Fu et al., 2011), could also respond to membrane ordering through loss of function (Li et al., 2004). Hence, regarding ER membrane biophysics, the low cholesterol and low saturation level renders the organelle extremely sensitive to change in its membrane composition (Radhakrishnan et al., 2008), which might be an evolutionary strategy for nutrient sensing and stress signaling.

Given the generality and dramatic influences of solid membrane, it deserves more cautious discussion on its relation to lipotoxicity and disease pathology (see summary in **Figure 6.11**). Many aspects of our observation in fact suggest that solid-like membrane is in broader sense than lipotoxicity. In particular, (1) solid-phase membrane forms under a wide range of concentration and time, yet only high dose and extended treatment can cause acute lipotoxic death. (2) Palmitate is widely reported to activate UPR signaling, yet palmitate-derived membrane domains (in about 1hr) proceeds the initiation of UPR signaling (3~6hrs (Borradaile et al., 2006; Cunha et al., 2008; Peng et al., 2011)). (3) ER stress progresses through prosurvival phase and then proapoptotic phase (Chen and Brandizzi, 2013). Our observation falls within the prosurvival phase of UPR signaling, where IRE1α-XBP1 signaling remains active (12hr (Kitai et al., 2013; Peng et al., 2011; Volmer et al., 2013)), which is also confirmed by data from our lab (not included here). (4) Solid-like membrane is not terminal but reversible involving active cellular clearance. Thus solid membrane is not an extreme status or artifact when cells are approaching

cell death or undergoing severe stress. To this extent our observation at cell level should be considered physiologically relevant.
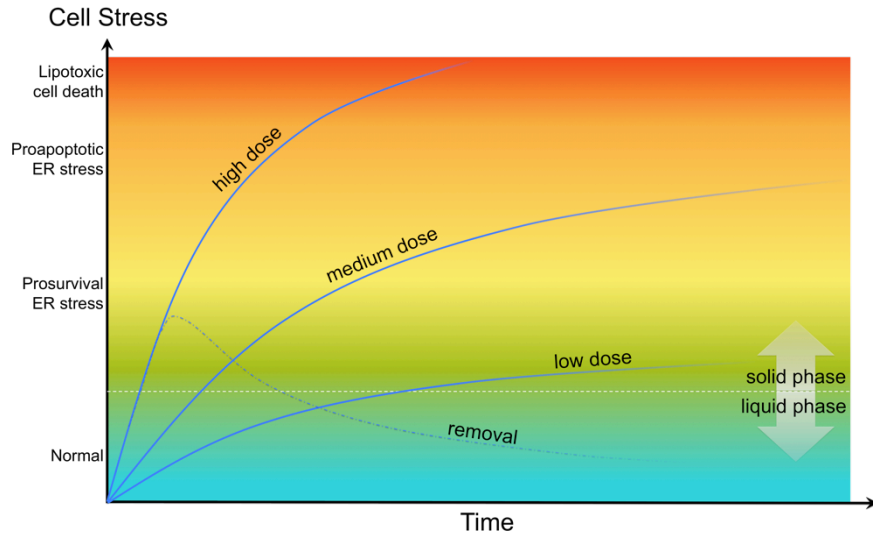
Figure 6.11 Relation of solid-like membrane to physiology. Cell stress progresses through multiple phases from normal to prosurvival ER stress, and to proapoptotic ER stress, and finally to lipotoxic cell death. The formation of solid-like membrane domain is dependent on both time and dose (blue solid lines), but is in general more acute than cell death and even ER stress. Most of our observations fall within prosurvival phase of ER stress. Only prolonged treatment with high-dose palmitate would lead to cell death. Moreover, domain formation is a reversible perturbation to ER membrane, which can be restored when palmitate is removed (blue dashed line).

Finally we discuss the relevance to more complex organismal level. Unlike the cell models, it is hard to define physiological concentration of fatty acid as a single fixed value. Instead, it is a dynamically fluctuating parameter that can reach as high as several millimolar in circulation

(Karpe et al., 2011; McGarry, 1992), of which more than 30% is palmitate. Thus numerous studies have used high concentration (400 μM ~ 1mM) palmitate to model the cytotoxicity of FFA in cell and tissue cultures. Yet what really happens in complex organisms? Fu et al. provided a good illustration in their elaborative review (Fu et al., 2012). Briefly, in healthy state cells can restore homeostasis by adaptive response to nutrition oscillation. In diseased state, chronic stress builds up slowly in time, although non-monotonically, due to incapability to fully restore to baseline level. In this context, acute stress (such as high-dose palmitate) is used to model the buildup of chronic stress within a reasonable experimental timeframe. Although not reaching full consensus, such acute stress initiator is found to reproduce most of phenotypes in the chronic condition. This is manifested by the large body of studies that are based on such acute model and had achieved phenotypes similar to the chronic model. For example, SFA models impaired insulin secretion in β cell (Cunha et al., 2008; Eguchi et al., 2012; Hoppa et al., 2009; Karaskov et al., 2006; Las et al., 2011), metabolic inflammation in adipose tissue (Holzer et al., 2011; Kratz et al., 2014; Robblee et al., 2016; Wen et al., 2011; Xu et al., 2013), diminished insulin sensitivity in skeletal muscle (Hommelberg et al., 2009; Peng et al., 2011; Weigert et al., 2004). Moreover, previous studies have observed similar phenotypes in parallel examination of acute and chronic models (Holzer et al., 2011; Miyagawa et al., 2016; Park et al., 2014). Thus our current study is meaningful in following this notion, and paves the way for further investigation.

6.8 Materials and Methods

Materials

Palmitic acid (16:0), palmitic acid-d31 (98% D) and stearic acid-d35 (98%D) were from Sigma. Fatty acids were reacted with sodium hydroxide (Sigma) above melting point to form 20mM solution, and then coupled to fatty-acid-free bovine serum albumin (BSA) (Sigma) in about 2:1 molar ratio to make 2mM stock solution in culture medium. They were then added to cell culture to achieve designated concentration. Chloroquine (Sigma), an inhibitor of lysosome acidification, was made into 2mM stock solution in PBS.

Cell culture

The following cell lines and their culture media were used in this study: HeLa (ATCC) and COS-7 (ATCC), Dulbecco's Modified Eagle Medium (DMEM, Invitrogen 11965-092); HepG2 (ATCC), Eagle's Minimum Essential Medium (EMEM, ATCC 30-2003). All media were supplemented with 10% fetal bovine serum (Invitrogen, 16000-044) and 100 U/mL penicillin-streptomycin (Invitrogen, 15140-122).

Cells that reached 80% confluence were dissociated and plated onto coverslips (No.1, FisherBrand) for most experiments and glass-bottom petri-dish (MATTEK, P35G-1.5-14-C) for single cell tracking. The coverslip was stuck to a microscope slide (1mm thick, VWR) using 0.1mm imaging spacer (SecureSeal) to make an imaging chamber filled with phosphate buffered

saline.

Fluorescence imaging

ER is visualized in live HeLa and COS-7 cells using CellLight® ER-GFP (Thermo Fisher Scientific) according to the manufacturer's manual. mCherry-Sec61β and Rtn4a-GFP was a gift from Gia Voeltz (Addgene plasmid # 49155 and 61807). GFP-Ub KO was a gift from Nico Dantuma (Addgene plasmid # 11934). pEGFP-LC3 (human) was a gift from Toren Finkel (Addgene plasmid # 24920). Premo™ Autophagy Tandem Sensor RFP-GFP-LC3B (Thermo Fisher Scientific) was used to measure autophagosome/lysosome fusion. For GFP-Ub KO and pEGFP-LC3, transient transfection was done in confluent HeLa cells with Lipofectamine® 3000 Reagent (Thermo Fisher Scientific) at 200ng DNA per well in a 24-well plate. 5 to 10 hours after transfection, cells were split and re-plated to adjust cell density and images were taken 48 hours after transfection. Mitochondria and lysosomes were visualized by staining with 100nM MitoTrackerTM Deep Red FM and 100nM LysoTrackerTM Red (ThermoFisher) diluted from their 1mM DMSO stock, respectively

For p62 and SERCA2 immunofluorescence, cells were fixed in 4% PFA at room temperature for 10min, permeabilized for 30 min in PBS containing 0.1% Tween20, 0.3M glycine (Sigma), 10% goat serum (Invitrogen) and 1% BSA, and then incubated with primary antibody at 1:1000 dilution in 2% BSA overnight at 4°C. They were then blocked in 10% goat serum, washed three

times with PBS, then incubated with secondary antibody at 1:1000 dilution in 10% goat serum overnight at 4°C, and finally blocked by 10% goat serum. Primary antibody used: mouse monoclonal antibody to p62 (Abcam 56416), Mouse monoclonal [2A7-A1] to SERCA2 ATPase (Abcam ab2861). Secondary antibody used: Alexa 647-goat anti-mouse IgG (ThermoFisher A-21236)

Confocal fluorescence imaging was performed on the same microscope used for SRS imaging (FV1200MPE; Olympus) and the same objective (60×, water immersion, N.A. = 1.2, UPlanAPO/IR; Olympus). For GFP, the excitation wavelength and filter selection were 488nm and 505-605nm (without red channels) or 505-525nm (together with red channels). For mCherry, RFP and LysoTracker Red, the excitation wavelength and filter selection were 543nm and 560-660nm. For MitoTracker Deep Red and Alexa647 (p62 and SERCA2 immunofluorescence), the excitation wavelength and filter selection were 635nm and 655-755nm. As SRS and fluorescence measurements used different lasers and dichroic mirrors, image was slightly shifted from one to the other channel. In order to perform multi-channel co-localization, we used a standard grid to determine the offset between the field of views of SRS and fluorescence and corrected it in all the multi-channel images later. Images were acquired by Fluoview Software and pseudo-colored by ImageJ.

Transmission electron microscopy

Transmission electron microscopy (TEM) was performed at the NYU Langone Medical Center Microscopy Core. HeLa cell pellets were fixed in freshly made 2% paraformaldehyde and 2.5% glutaraldehyde (Electron Microscopy Science) in 0.1M sodium cacodylate buffer (Electron Microscopy Science) for 2hrs at room temperature. They were post-fixed with 1% osmium tetroxide for 1hr and then with 2% osmium tetroxide, 1.5% potassium ferrocyanide (reduced osmium, FeOs) for 1hr at 4°C. For TA-FeOs, the post-fixed pellets were further incubated twice with 1% tannic acid in phosphate buffer for 2hr at 4°C. The samples were then processed in a standard manner and were examined under a Philips CM-12 electron microscope and photographed with a Gatan (4 k × 2.7 k) digital camera (Gatan).

6.9 References

1. N. M. Borradaile *et al.*, Disruption of endoplasmic reticulum structure and integrity in lipotoxic cell death. *J. Lipid Res.* **47**, 2726–37 (2006).

2. G. Peng *et al.*, Oleate blocks palmitate-induced abnormal lipid distribution, endoplasmic reticulum expansion and stress, and insulin resistance in skeletal muscle. *Endocrinology*. **152**, 2206–18 (2011).

3. A. K. Leamy *et al.*, Enhanced synthesis of saturated phospholipids is associated with ER stress and lipotoxicity in palmitate treated hepatic cells. *J. Lipid Res.* **55**, 1478–1488 (2014).

4. S. Schuck, W. A. Prinz, K. S. Thorn, C. Voss, P. Walter, Membrane expansion alleviates endoplasmic reticulum stress independently of the unfolded protein response. *J. Cell Biol.* **187**, 525–536 (2009).

5. D. A. Cunha *et al.*, Initiation and execution of lipotoxic ER stress in pancreatic beta-cells. *J. Cell Sci.* **121**, 2308–18 (2008).

6. Y. Shibata *et al.*, Mechanisms determining the morphology of the peripheral ER. *Cell*. **143**, 774–788 (2010).

7. M. J. Dykstra, in *Biological Electron Microscopy* (Springer US, Boston, MA, 1992; http://link.springer.com/10.1007/978-1-4684-0010-6_2), pp. 5–78.

8. E. Diakogiannaki, H. J. Welters, N. G. Morgan, Differential regulation of the endoplasmic reticulum stress response in pancreatic beta-cells exposed to long-chain saturated and monounsaturated fatty acids. *J. Endocrinol.* **197**, 553–63 (2008).

9. M. Kalina, D. C. Pease, Preservation of Ultrastructure By Tannic Acid in Saturated in Model and Type Systems. *J. Cell Biol.* **74**, 726–741 (1977).

10. A. a. Rowland, G. K. Voeltz, Endoplasmic reticulum–mitochondria contacts: function of the junction. *Nat. Rev. Mol. Cell Biol.* **13**, 607–625 (2012).

11. M. Hamasaki *et al.*, Autophagosomes form at ER-mitochondria contact sites. *Nature*. **495**, 389–93 (2013).

12. H.-W. Park *et al.*, Pharmacological correction of obesity-induced autophagy arrest using calcium channel blockers. *Nat. Commun.* **5**, 4834 (2014).

13. K. Miyagawa *et al.*, Lipid-Induced Endoplasmic Reticulum Stress Impairs Selective Autophagy at the Step of Autophagosome-Lysosome Fusion in Hepatocytes. *Am. J. Pathol.* **186**, 1–14 (2016).

14. A. Stolz, A. Ernst, I. Dikic, Cargo recognition and trafficking in selective autophagy. *Nat. Cell Biol.* **16**, 495–501 (2014).

15. N. Mizushima, T. Yoshimori, B. Levine, Methods in Mammalian Autophagy Research. *Cell*. **140**, 313–326 (2010).

16. G. Las, S. B. Serada, J. D. Wikstrom, G. Twig, O. S. Shirihai, Fatty acids suppress autophagic turnover in β-cells. *J. Biol. Chem.* **286**, 42534–42544 (2011).

17. J. Liu *et al.*, Palmitate promotes autophagy and apoptosis through ROS-dependent JNK and p38 MAPK. *Biochem. Biophys. Res. Commun.* **463**, 1–6 (2015).

18. J. Janikiewicz *et al.*, Inhibition of SCD1 impairs palmitate-derived autophagy at the step of autophagosome-lysosome fusion in pancreatic β-cells. *J. Lipid Res.* **56**, 1901–1911 (2015).

19. M. Ogata *et al.*, Autophagy is activated for cell survival after endoplasmic reticulum stress. *Mol. Cell. Biol.* **26**, 9220–31 (2006).